Doctoral Dissertation

Electrochemical Surface-Enhanced Raman Spectroscopy (EC-SERS) for Bio-analysis on Silver-sputtered Screen-printed Electrode

Zicheng Zhu

January 2019

Department of Applied Physics
Graduate School of Engineering,
Osaka University

TABLE OF COTENTS

Abstract

Electrochemical Surface-enhanced Raman spectroscopy (EC-SERS) is a promising analytical tool for monitoring and rapid detection of analytes with high sensitivity. Compared with non-electrochemical SERS, EC-SERS takes the advantages of manipulating analyte on the surface through electrochemical modulation. Benefited from the adjustable potential of the electrode, the orientation and adsorption modes of the molecule on the surface change that can affect SERS intensity. Besides, oxidation or reduction process may occur due to the applied positive or negative potential which also influences the enhancement of SERS signal. Therefore, EC-SERS technology provides an enhanced signal and more selective peaks. Besides, EC-SERS detection is useful for biological analysis which is possible for observing the change of orientation and molecule-surface bonding by applied different potentials. Instrumentation of EC-SERS measurements consists of SERS-active electrode, potential-stat device, and Raman spectroscopy. This dissertation comprises of five chapters. The content of each chapter is described in the following paragraph.

The first chapter covers the general information of electrochemical surface-enhanced Raman spectroscopy including the history and basic theory. Also, then, the nanofabrication methods used for SERS-active substrate will be introduced. Finally, the motivation of bio-analysis and perspective for this dissertation will be mentioned.

In the second chapter, the original method has been proposed for rapid and highly productive fabricating SERS-active screen-printed electrode (SPE) by sputtering

deposition which is introduced. Silver nanoparticles successfully deposited two kinds of working electrodes of SPE which were carbon electrode and the gold electrode. Besides, the sputtering experiments of different substrates (paper, glass epoxy and polyethylene terephthalate) of the SPE were also conducted. The comparison of SERS enhancement of rhodamine 6G (R6G) on different kinds of SERS-active SPEs was introduced. Also, the relationship between the surface roughness (observed through AFM and SEM images) and SERS enhancement has been investigated. Compared with the classical citrate reduction method, the sputtering method guaranteed low SERS background signal and a maximum of surface absorption for target analytes because there was no other material except pure silver directly deposited on the working electrode. These results demonstrated the applicability of this mass producible fabrication method for producing SERS-active SPEs, as well as, highlighting the future potential of commercial bio-applications.

The third and fourth chapter move the focus on the application of EC-SERS technology to biosensors. It is a label-free technique as the Raman signal arises from the vibration peaks of the chemical bonds in the molecules of interest. Furthermore, it has excellent potential for multi-component detection. The benefits brought by this method include simple experimental process, fast detection time and highly sensitive detection. For chapter three, there are two applications which are for the diagnosis of preeclampsia and jaundice. For the first example, the uric acid, as an important biomarker in urine for early diagnosis of preeclampsia, was used for EC-SERS bio-

analysis. It could be observed that the intensity signal was gradually enhanced with more negative applied potential until the applied potential reached -1400 mV.

For the fourth chapter, quantitative detection of aminoglutethimide (AGI) has been investigated based on its adsorption on the SERS-active electrode employing the EC-SERS technology. EC-SERS spectra of AGI molecule exhibited different adsorption mode onto the substrate with different potentials applied. When the applied potential reaches to -400 mV, the intensities of the EC-SERS peaks donated by both aniline moiety and glutarimide moiety are significantly enhanced, this suggests the bidentate interaction of AGI molecule with the substrate. A linear dependence occurs in the range of 1×10^{-5} M to 2×10^{-7} M. The limit of detection (LOD) is 40 ng/mL and the R squared of the linear curve is 0.98. Compared with the SERS technique, these adsorption modes offer the advantages of enhanced signal intensity and more selectivity of the AGI molecule. In the future, the EC-SERS sensor may become a useful tool for rapid and routine analysis in anti-doping detection and patient biomarkers for on-site use.

The fifth chapter provides the EC-SERS experiments of pyridine to comprehensively explain SERS and investigate EC-SERS spectra from the chemical and physical enhancement mechanisms. The essential information is presented for exhibiting the mechanisms of electrochemical adsorption and reaction. The results are discussed for investigating the SERS mechanisms and characterization of adsorption configuration to an elucidation of electrochemical reaction mechanisms.

The sixth chapter summarizes this dissertation. Prospective developments of EC-SERS in substrates, methods, theory and future remarks will be mentioned in this chapter.

List of Tables

List of Figures

Fig 2.2. The photo of SPE used in this work which is composed by working electrode (WE), counter electrode (CE) and reference electrode (RE). SEM image of two different materials of working electrodes which are made by a) carbon and b) gold.

Fig 2.3. a) V0005 in-line sputtering machine. b) Schematic figure of V0005 in-line sputtering machine.

Fig 2.4. Silver-deposition on the screen-printed electrodes with different substrates.

Fig 2.5. SEM raw images of 200 k magnification ratio of silver-deposited carbon working electrodes with different deposition time of (Raw a) 4.8 s, (Raw b) 12 s, (Raw c) 16.8 s and (Raw d) 24 s, which corresponding to the zoom out images (a), (b), (c) and (d), respectively. Silver target power of sputtering deposition: 250 kW. E-beam of SEM image: 12 kV.

Fig 2.6. SEM raw images of 200 k magnification ratio of silver-deposited gold working electrodes with different deposition time of (Raw a) 12 s, (Raw b) 16.8 s and (Raw c) 24 s, which corresponding to the zoom out images (a), (b) and (c), respectively. Silver target power of sputtering deposition: 250 kW. E-beam of SEM image: 5 kV.

Fig 2.7. The cross-sectional image of (a) bare carbon working electrode and (b) silver-deposited carbon working electrode. The diameters of silver nanoparticles range from approximately 20 nm to 30 nm.

Fig 2.8 Two proposed models of different structures of Ag-depostied film on the reference glass substrates. Model a. island formation looked like Ag nanoparticles on the glass substrate; Model b. Ag thin film on the glass substrate.

Fig 4.1 (a) Raman spectral of the AGI powder and (b) SERS signal of 0.1 mM AGI in ethanol solution without applied potential. The acquisition time is 60 s and laser powers are 0.5 mW and 2.8 mW, respectively.

Fig 4.2 Different absorption methods which are a) aniline (AN) b) glutarimide (GI) and c) both aniline and glutarimide moieties interacting with the silver surface

Fig 4.3 Cyclic voltammogram of a bare electrode in buffer solution (blue line), a bare SERS-active electrode in buffer solution (red line), and a SERS-active electrode containing the AGI in buffer solution (black line). Scan rate: 50 mV s^{-1}

Fig 4.4 SERS spectral of 0.1 mM AGI in buffer solution with different potentials at the SERS-active electrode. The assignments marked in the graph: C-N-C / CH_3 bending (948 cm-1), C-H / CH_2 bending (1147 cm-1), CH_2 wagging (1313 cm-1) and NH_3^+ rocking (1566 cm-1). The potentials are ramped at -200 mV increment from 0 mV to -1000 mV vs Ag/AgCl. Acquisition time: 60 s, laser power: 2.8 mW.

Fig 4.5 The structure of the AGI molecule in stick-ball mode with the charge density shown in color calculated by B3LYP/6-311 + G.

Fig 4.6 Proposed orientation of the AGI molecule on the AgNPs electrode surface, based on interpretation of spectral data. The applied potentials: at (a) −200 mV, (b) −400 mV, (c) -600 mV and (d) from -800 to -1000 mV vs. Ag/AgCl.

Fig 4.7 a) E-SERS signals of AGI on the silver-deposited carbon screen-printed electrode (SPE) with -400 mV potential applied. b) background signal on the silver-deposited carbon SPE. c) AGI in buffer solution on the bare carbon SPE

Fig 4.8 (a) EC-SERS spectra at the applied potential of -400 mV vs Ag/AgCl with enhanced peak signal at 1147 cm^{-1}. I, II, III, IV, V and VI corresponding to the different concentration of the AGI solution of $1x10^{-4}$, $1x10^{-5}$, $5x10^{-6}$, $1x10^{-6}$, $5x10^{-7}$ and $2x10^{-7}$ M, respectively (b) Calibration curve of different drug concentrations of AGI with good linear dependence (R^2 = 0.98) ranging from $1x10^{-5}$ to $2x10^{-7}$. Error bar represents standard deviation where n = 4.

Fig 5.1 Selected normal modes of pyridine

Fig 5.2 SERS spectral of 0.01 mM pyridine + 0.05 M KCL in 0.05 M NaF solution with different potentials at the SERS-active electrode. The potentials are ramped at -200 mV increment from 0 mV to -1000 mV vs Ag/AgCl. Acquisition time: 60 s, laser power: 2.8 mW.

List of commonly used abbreviations

YSI - Yellow Spring Instruments

FAD - Flavin adenine dinucleotide

FADH2 - Hydroquinone form of flavin adenine dinucleotide

ISFET - Ion-sensitive field-effect transistor

ENFET Enzyme Field Effect Transistor

HPLC - high performance liquid chromatography

GC - Gas chromatography

GLC - Gas-liquid chromatography

RPLC - Reversed phase liquid chromatography

NPLC - Normal phase liquid chromatography

LC - Liquid chromatography

CE-MS - Capillary electrophoresis–mass spectrometry

GC-MS - Gas chromatography–mass spectrometry

LC-MS - Liquid chromatography–mass spectrometry

LC-DAD - Liquid chromatography–diode array detection

SFC - Supercritical fluid chromatography

LBA - Ligand binding assays

ELISA - Enzyme-linked immunosorbent assay

MIA - Magnetic immunoassay

RIA - Radioimmunoassay

DPI - Dual-polarization interferometry

MRI - Magnetic Resonance Imaging

RAST - Radioallergosorbent test

UTI - Urinary tract infection

UV–Vis or UV/Vis - Ultraviolet–visible spectroscopy or ultraviolet–visible spectrophotometry

ECL- Electrochemiluminescence

UV-NIR - UltraViolet - Near InfraRed

LSPR - Localized Surface Plasmon Resonance

HDAC - Histone deacylase

SERS - Surface-Enhanced Raman Scattering

SLIPSERS -Slippery Liquid-Infused Porous SERS

SHINERS - Shell-isolated nanoparticle-enhanced Raman spectroscopy

FDTD - Finite difference time domain

HOMO - Highest occupied molecular orbital

LUMO - Lowest unoccupied molecular orbital

EC-SERS - Electrochemical surface-enhanced Raman scattering

EM - Electromagnetic field enhancement

CE - Chemical enhancement

Ns - Metallic nanostructures

FIB - Focused ion beam

EF - Enhancement factor

AAO - Anodized aluminum oxide

AgFON - Ag films over nanosphere

AFM -Atomic force microscope

SEM - Scanning electron microscope

DFM - Dynamic force mode

EMA - Effective medium approximation

R6G - Rhodamine 6G

Au - Gold

Ag - Silver

C - Carbon

UA - Uric acid

CA - Chronoamperometry

CV - Cyclic voltammetry

SWV - Square wave voltammetry

DPV - Differential pulse voltammetry

LSV - Linear sweep voltammetry

SPE - Screen-printed electrode

CCD - Charge-Coupled Device

DFT - Density functional theory

AGI - Aminoglutethimide

AN - Aniline

GI - Glutarimide

LOD - Limit of detection

Py - Pyridine

Chapter 1. Introduction

1.1 Biotechnology

1.1.1 Biosensor

Biosensors are principally employed in extensive fields of biotechnology such as medicine, agriculture, environment and so on. Biosensors are used for these purposes when the concentration of target analytes are monitored or evaluated. In the following paragraphs, the history, principle, different types of biosensors will be introduced.

1.1.2.1 History

The history of biosensors is back to as early as 1906. The concentration of an acid in a liquid is proportional to the electric potential was demonstrated by M. Cremer [1]. After three years, the concept of pH (hydrogen ion concentration) was introduced by Soren Peder Lauritz Sorensen. Before 1922, Griffin and Nelson first introduced immobilization of the enzyme invertase on charcoal and aluminum hydroxide [2], [3]. In the year 1922, W.S. Hughes put forward an electrode for pH measurements [4]. The first acknowledged biosensor was developed by Leland C. Clark, Jr in 1956. His invention was used for oxygen detection and named 'Clark electrode' [5]. In 1962, Leland Clark developed an amperometric enzyme electrode for the detection of glucose. Updike and Hicks discovered the first enzyme-based sensor which was reported by in 1967 [6]–[12]. Two years later, the potentiometric biosensor was developed by Guilbault and Montalvo Jr which was used for detecting urea [13]. In 1970, the ion-sensitive field effective transistor was discovered by Bergveld [14]. In 1975, the first

commercial biosensor was eventually produced by Yellow Spring Instruments (YSI) [15]. In the same year, Lubbers and Opitz developed the fiber-optic biosensor for oxygen detection [16], and Suzuki et al. invented first microbe-based immunosensor [17]. In the year 1978, the first tissue based sensor for the determination of amino acid arginine was reported by Rechnitz [18]. Schultz achieved the fiber-optic biosensor for glucose detection in 1982 and surface plasmon resonance immunosensor was invented by Liedberg et al. in the next year [19]. In the following year, first mediated amperometric biosensor was developed for glucose detection [20]. The SPR-based biosensor was developed by Pharmacia Biacore [21] in 1990, and then Handheld blood biosensor was reported by i-STAT in 1992 [21]. Table 1 shows the historical overview of biosensors.

Table 1.1 Important cornerstones in the development of biosensors

1962	An amperometric enzyme electrode for the detection of glucose by Leland Clark [6]-[12]
1967	The first enzyme-based sensor reported by Updike and Hicks [6]-[12]
1969	Potentiometric biosensor to detect urea was reported by Guilbault and Montalvo Jr. [13]
1970	Discovery of ion-sensitive field-effect transistor (ISFET) by Bergveld [14]
1975	First commercial biosensor for glucose detection by YSI [15]
	Fibre-optic biosensor for carbon dioxide and oxygen detection by Lubbers and Opitz [16]
	First microbe-based immunosensor by Suzuki et al. [17]
1978	First tissue based sensor for the determination of amino acid arginine by Rechnitz [18]
1982	Fibre-optic biosensor for glucose detection by Schultz [19]
1983	Surface plasmon resonance (SPR) immunosensor by Liedberg et al. [20]
1984	First mediated amperometric biosensor: ferrocene used with glucose oxidase for glucose detection [20]
1990	SPR-based biosensor by Pharmacia Biacore [21]
1992	Handheld blood biosensor by i-STAT [21]

1.2.2.2 Principle of biosensor

A biosensor is an analytical device incorporating a deliberate and intimate combination of a specific biological element [16], [22]–[24]. Biosensors are employed in applications such as disease monitoring [25]–[33], drug discovery [34]–[41], and detection of pollutants [42]–[50], disease-causing [51]–[59] and so on. A typical biosensor is represented in the graph of Fig. 1, it consists of the following components which are bioreceptor and transducer. The analyte is the detection target which reacts with bioreceptor to generate the signals in the form of light, heat, current, pH change and so on. There are two different kinds of bioreceptor: nanostructure (nanoparticle, nanotube, and nanotip) and biomaterial (enzymes, cells, DNA and antibodies). The transducer is an element such as a photodiode, thermistor, electrode, quartz electrode etc. that converts bio-recognition into a measurable signal. Combination of electronics parts, display and software generates the result of the biosensor.

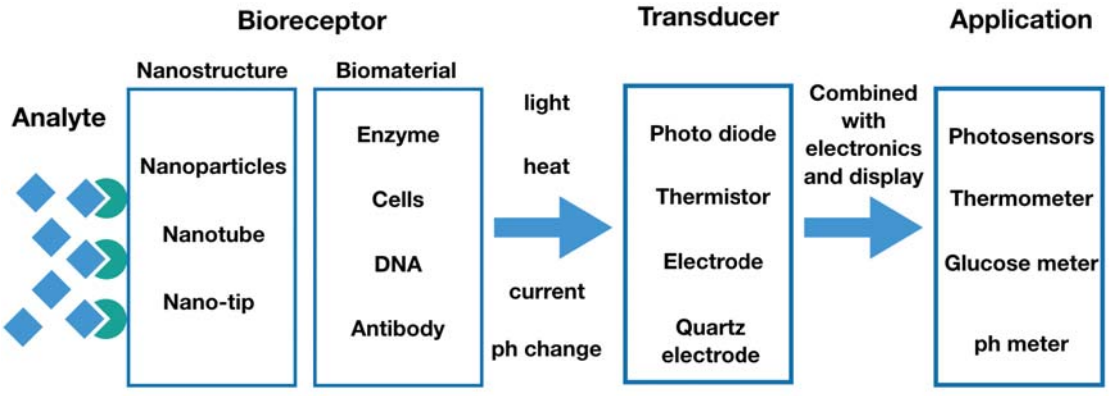

Fig 1.1 Schematic representation of a biosensor.

1.2.2.3 Different types of biosensors

The biosensors can be of many types such as: resonant biosensors [60]–[64], optical-detection biosensors [24], [65]–[68], thermal-detection biosensors [69], [70], ion-sensitive FET (ISFET) biosensors [14], [71]–[73] and electrochemical biosensors [74]–[76].

Resonant biosensors are usually coupled with antibodies as bioreceptor. When the analyte (antigen) gets attached to the antibodies, the changes of the resonant frequency can be measured. For optical biosensor, extensively wide biomaterials can be used such as enzymes, receptors, antibodies, nucleic acids and so on. It is a compact analytical device containing an optical transducer system, which detects the light change of the analyte during the reaction and proportionate to the concentration. Thermal-detection biosensors composed by immobilized enzyme molecules as bioreceptor and temperature sensors as a transducer. During the biological reactions, heat is absorbed or produced which leads to the changes in temperature. Sensors measure the changes in temperature, and the relationship between temperature changes and the concentration of the analyte can be evaluated. These are semiconductor FETs having an ion-sensitive surface. The surface electrical potential changes when the ions and the semiconductor interact. This change in the potential can be subsequently measured. The electrochemical biosensors are mainly used for the detection of hybridized DNA, DNA-binding drugs, glucose concentration, etc. The chemical reactions of electrochemical

biosensors generate the electron or consume ions which affect the electrical properties of the solution. Finally, the change of the electrical properties can be detected.

1.1.2 Bioanalytical techniques

Bioanalysis is comprising the classification and quantification of analytes in biological samples such as blood, plasma, serum, saliva, urine, feces, skin, hair, and organ tissue [77]–[82]. Bioanalysis is not only to detect small molecules such as drugs and metabolites but also to recognize large molecules such as proteins and peptides. There are several bioanalytical techniques commonly used in bioanalysis studies which are listed in table 1.2. It is recognized that bioanalytical methods and techniques are continually undergoing changes and improvements. It is necessary to indicate that each bioanalytical method has its features, which will diversify from analyte to analyte. In these situations, validation standards may need to be generated for each analyte. Furthermore, the suitability of the method may also be affected by the terminal purpose of the investigation.

1.1.2.1 Hyphenated techniques

The hyphenated techniques include liquid chromatography-mass spectrometry (LC-MS), gas chromatography-mass spectrometry (GC-MS), liquid chromatography-diode array detection (LC-DAD) and capillary electrophoresis–mass spectrometry (CE-MS). Liquid chromatography-mass spectrometry (LC-MS) is an analytical chemistry technique that couples the physical division capacities of liquid chromatography (or

HPLC) with the mass analysis capacities of mass spectrometry (MS) [83]–[87]. Gas chromatography-mass spectrometry (GC-MS) is an analytical method that combines the features of gas-chromatography and mass spectrometry to identify different substances within a test sample [84], [88]–[93]. Capillary electrophoresis-mass spectrometry (CE-MS) is an analytical chemistry technique formed by the combination of the liquid separation process of capillary electrophoresis with mass spectrometry [94]–[100].

1.1.2.2 Chromatographic methods

Chromatography is a laboratory technique for the separation of a mixture [101]. The mixture is dissolved in a fluid called the mobile phase, which carries it through a structure holding another material called the stationary phase. The idea of preparative chromatography is to segregate the components of a compound for the following use and is thus a sort of purification [102], [103]. Analytical chromatography is done generally with fewer amounts of substance and is for setting the presence or detecting the appropriate proportions of analytes in a mixture [104]. There are several kinds of chromatography techniques such as Liquid chromatography (LC) [105], [106] [107] [86], Gas chromatography (GC) [108] [109] [110]–[113] and Supercritical fluid chromatography [114] [115], [116].

1.1.2.3 Electrophoresis

Electrophoresis is the motion of dispersed particles relative to a fluid under the

influence of a spatially uniform electric field [117]–[121]. Electrophoresis of positively charged particles (cations) is named as cataphoresis, while electrophoresis of negatively charged particles (anions) is called as anaphoresis. Electrophoresis is implemented in labs to isolate macromolecules based on size. The procedure uses a negative charge, so proteins move towards a positive charge which is applied for both DNA and RNA analysis.

1.1.2.4 Ligand binding assays

Ligand binding assays (LBA) is an analytic procedure, which relies on the binding of ligand molecules to receptors, antibodies or other macromolecules [122]. A detection process is employed to ascertain the presence and amount of the ligand-receptor complexes produced, and this is typically prepared electrochemically or through a fluorescence detection technique [123]. This sort of analytic examination can be managed to examine for the occupation of target molecules in a sample that is identified to bind to the receptor [124]. There are numerous types of ligand binding assays such as dual polarisation interferometry (DPI) [125]–[128]. enzyme-linked immunosorbent assay (ELISA) [129]–[134], magnetic immunoassay (MIA) [135], [136] and Radioimmunoassay (RIA) [137], [138].

1.1.2.5 Optical Spectrometry

Optical spectrometry is the subject of the interaction between object and electromagnetic radiation. Historically, spectroscopy founded through the investigation

of visible light dispersed according to its wavelength by a prism. Next, the idea was significantly extended to involve any interaction with radiative energy as a role of its wavelength or frequency. Spectroscopy is a power bioanalytical tool for bioanalysis such as Electrochemi-luminescence (ECL) [139]–[142], UltraViolet - Near InfraRed (UV-NIR) [143], [144], Fluorescence detection, Raman spectroscopy and Localized Surface Plasmon Resonance (LSPR). Raman spectroscopy and localized surface plasmon resonance are related to the main topic of the dissertation. The details will be introduced from chapter 1.2.

Table 1.2 Some techniques commonly used in bioanalytical studies

Bioanalysis	Techniques and Methods	
1	Hyphenated techniques	Liquid chromatography-mass spectrometry (LC-MS)
		Gas chromatography-mass spectrometry (GC-MS)
		Capillary electrophoresis–mass spectrometry (CE-MS)
2	Chromatographic methods	High performance liquid chromatography (HPLC)
		Gas chromatography (GC)
		Ultra performance liquid chromatography (UPLC)
		Supercritical fluid chromatography
3	Electrophoresis	-
4	Ligand binding assays	Dual polarisation interferometry
		Enzyme-linked immunosorbent assay (ELISA)
		magnetic immunoassay (MIA)
		Radioimmunoassay (RIA)
5	Optical Spectrometry	Electrochemiluminescence (ECL)
		Ultraviolet–visible spectroscopy (UV-VIS)
		Fluorescence detection
		Raman spectroscopy
		Localized Surface Plasmon Resonance (LSPR)

1.1.3 Bio-applications

There are various applications of the biosensor which cover their use for food quality and safety, disease detection, environmental monitoring, plant biology, biodefense biosensing and many more. In the food processing industry, the development of biosensors is required to respond to the demand for quality and safety of food with real-time, selective, simple and inexpensive techniques [145]. Enzymatic biosensors which reported by Ghasemi-Varnamkhasti et al. are used for monitoring of aging of beer based on cobalt phthalocyanine [146]. Presence of Escherichia coli in vegetables is a bioindicator of fecal contamination in food [147]. In the medical field, the demands of biosensors are increasing significantly. Glucose biosensor is widely used by diabetes patients who require precise control over blood-glucose levels [148], [149]. Besides, a promising biosensor used for urinary inspection is under study. For environmental monitoring, the portable, rapid, and smart biosensors are required [150]. The cost-effective, fast, in situ and real-time biosensing device for multiplexed pollutant detection, shows the recent achievement of biosensors with the technique of new materials and nanotechnology. In plant biology, the revolution of new DNA sequencing technology achieves the significant improvement in plant science [151]. Cellular, subcellular localization and metabolite levels can be observed through the methods of mass spectroscopy. For biodefense applications, the biosensor is demanded to sensitively and real-timely detect the bacteria, toxins, and viruses. The nucleic acid-

based sensor can reach high sensitive detection without utilizing amplification steps [152].

1.2 Raman scattering

Raman scattering is the inelastic scattering of a photon by molecules which are excited to different vibrations or rotational energy levels. When the incident light strikes on the molecule, most of the photon are elastically scattered which called Rayleigh scattering [153]. The tiny minority of the scattered photons are scattered inelastically by an excitation. The energy and frequency of scattered photons are different from those of incident photons [154].

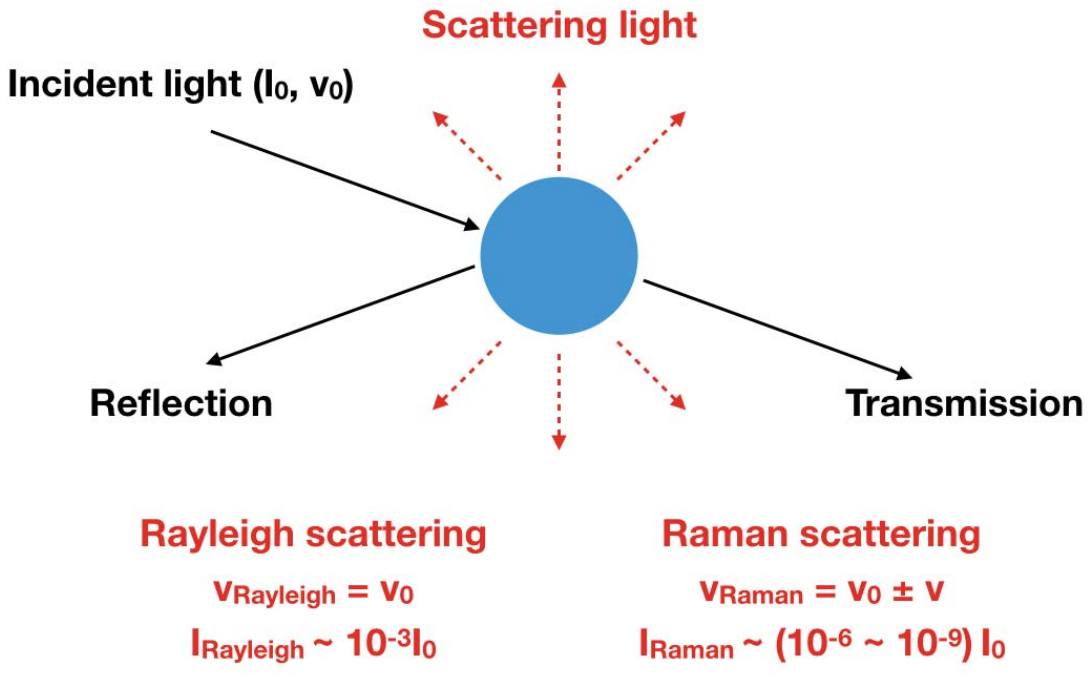

Fig. 1.2 Introduction of scattered radiation and Raman scattering

1.2.1 History

The inelastic scattering of light was predicted by Adolf Smekal in 1923 [155]. In 1922, Indian physicist C. V. Raman published his work on the "Molecular Diffraction of Light," which led to his discovery of the radiation effect. The Raman effect was first reported by C. V. Raman and K. S. Krishnan [156] on 21 February 1928. Raman received the Nobel Prize in 1930 [157]. In 1998 the Raman effect was designated a National Historic Chemical Landmark by the American Chemical Society.

1.2.2 Mechanism of Raman scattering

As shown in Fig 1.3, the photon from the laser beam produces an oscillating polarization in the molecules, exciting them to a virtual energy state. Also, then the photon is re-emitted as scattered light. Several kinds of the possible polarizations can be coupled with the oscillating polarization of the molecule such as vibrational and electronic excitations [158]. The following equations can calculate the dipole moment in a molecule:

$$p = \alpha E \tag{1}$$

where p is induced electric dipole moment of a molecule, α is polarizability and E is electric field.

$$\alpha = \alpha_0 + (\frac{\partial \alpha}{\partial \gamma})\Delta\gamma \tag{2}$$

$$\Delta\gamma = \gamma_{max}\cos(2\pi v t) \tag{3}$$

$$E = E_0\cos(2\pi v_0 t) \tag{4}$$

$$p = \alpha_0 E_0 \cos(2\pi v_0 t) + \frac{E_0 \gamma_{max}}{2}\left(\frac{d\alpha}{d\gamma}\right)\left(\cos\big(2\pi t(v_0 + v)\big) + \cos\big(2\pi t(v_0 - v)\big)\right) \quad (5)$$

where α_0 is molecule equilibrium polarizability, E_0 is a maximum electric field, v_0 is excitation frequency, v is vibrational frequency and γ_{max} maximum vibrational amplitude. The vibrational state will change if the polarization in the molecule couples with these possible polarizations. On the contrary situation, the scattered photon will have the same energy as the incident photon which called Rayleigh scattering.

When the polarization in the molecule couples to the higher or lower vibrational state, the energy of a scattered photon is different from that of the incident photon. The energy difference between the absorbed and emitted photon corresponds to the energy difference between two resonant states of the material and is independent of the absolute energy of the photon. Raman scattering can be classified as two types, Stokes Raman scattering, and anti-Stokes Raman scattering. If the energy of a scattered photon is higher than an incident photon, this type of scattering is known as Stokes Raman scattering. By contrast, anti-Stokes Raman scattering is a process that electron is excited from the vibrational level to the ground level as shown in Fig 1.3.

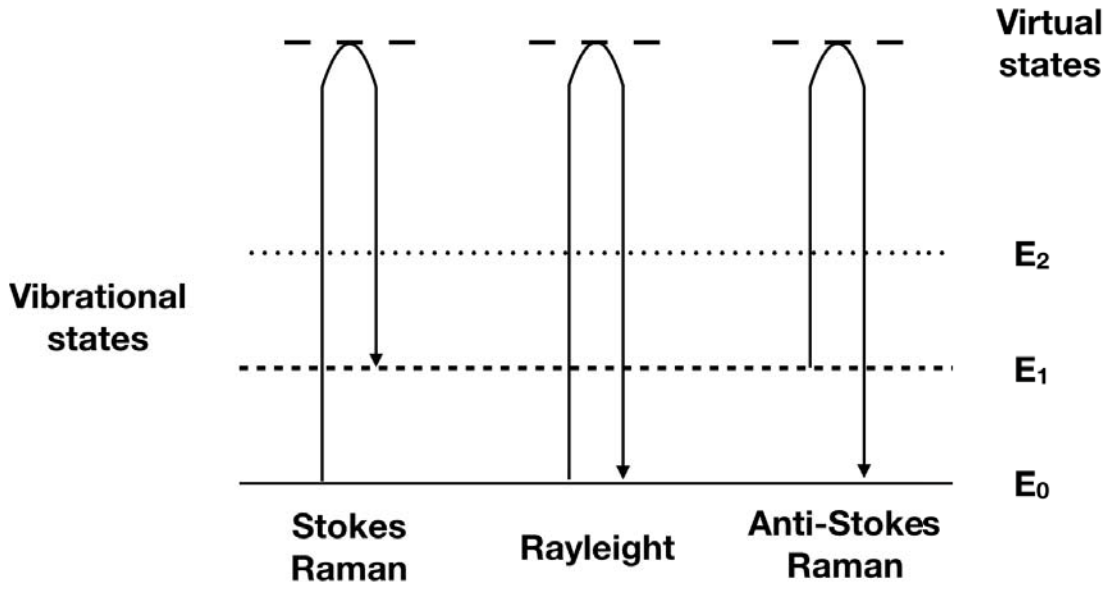

Fig. 1.3 Relationship between energy level and molecule vibrations

1.2.3 Surface-enhanced Raman spectroscopy (SERS)

Surface-enhanced Raman spectroscopy (SERS) is a surface-sensitive technique that enhances Raman scattering on rough (or nanostructures) metal surfaces. The enhancement factor can be as much as 10^{10} to 10^{14} [159]–[165], which means the technique is available for detecting single molecules.

Martin Fleischmann first observed SERS from the pyridine adsorbed on the electrochemically roughened silver electrode in 1973 [166]. In the year 1977, two groups independently proposed a mechanism of explaining the SERS effect. Jeanmaire and Van Duyne introduced an electromagnetic effect [167], while Albrecht and Creighton noted a charge-transfer effect [168]. The electromagnetic theory proposes the excitation of localized surface plasmons, while the chemical theory proposes the formation of charge-transfer complexes.

1.2.3.1 Electromagnetic enhancement

Surface-enhanced Raman scattering is a phenomenon including the light−molecule interaction shown in Fig 1.4 a and the light−metal interaction shown in Fig 1.4 b. When the light strikes on the surface, the dipolar of metal nanoparticle contributes to the plasmon oscillations, the localized surface plasmons resonance (LSPR) is excited when the frequency of the incident light matches with an inherent oscillation frequency of free electrons in the metal [160]. It leads to an electric field on the metal nanoparticle. The metallic nanoparticles such as Ag, Au, and Cu can generate a strong LSPR effect in the visible to near-infrared region. As a result, the energy is enhanced for 2 to 5 orders of magnitude [169]–[171].

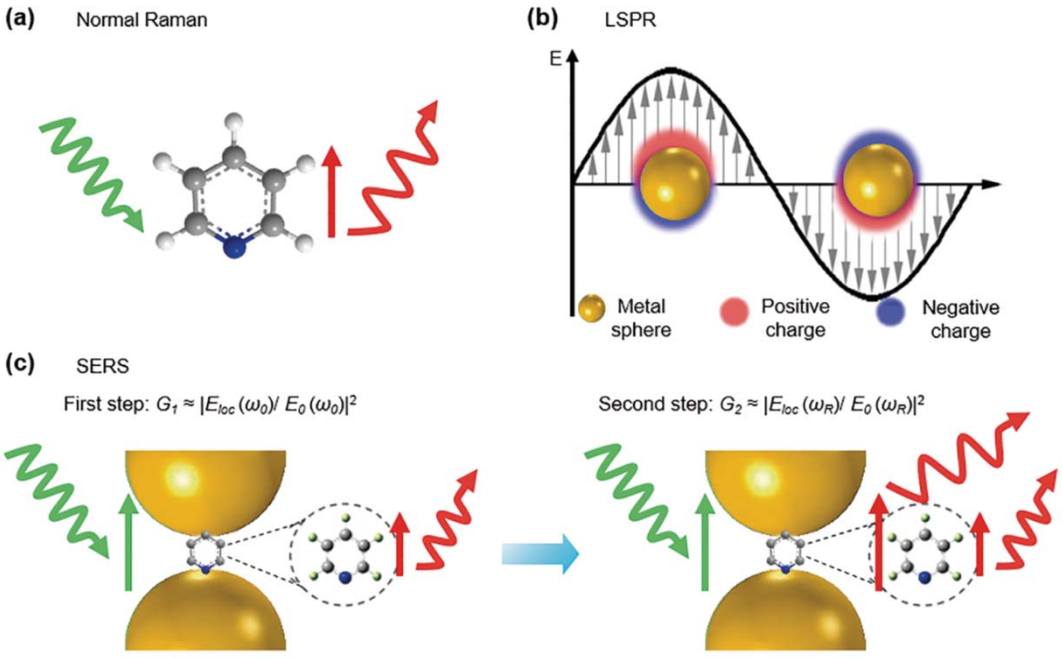

Fig. 1.4 Schematics of (a) normal Raman, (b) localized surface plasmon resonance (LSPR), and (c) electromagnetic enhancement mechanism in SERS, including the two-step enhancements [172].

The SERS process can be considered by a two-step enhancement process, as shown in Fig 1.4c. The first step results from the enhanced local field (near field) surrounding the nanoparticles at the exciting wavelength

(λ_{ex}): $E_{loc}(\lambda_{ex}) = G_1 E_0$ (6)

where G_1 is the enhancement factor of the electromagnetic field in the near field at λ_{ex}, and E_0 the exciting light with λ_{ex}. The nanoparticles serve as transmitting optical antennae to transfer the Raman signal as the second step, which is from the near field to the far field. The Raman signal is proportionate to the enhanced local electric field at the Raman emission wavelength of

λ_{em}: $E_{loc}(\lambda_{em}) = G_2 E_0$. (7)

Therefore, the overall SERS enhancement depends on the "exciting" and "emitting" field:

$G_{SERS} \propto [E_{loc}(\lambda_{ex})/E_0]^2 [E_{loc}(\lambda_{em})/E_0]^2 = G_1^2 G_2^2$ (8)

The optimal SERS enhancement requires a delicate balance between exciting and emitting wavelengths with the plasmon peak of the metal nanostructure. The SERS enhancement factor is approximately proportional to the fourth power of the enhancement of the local electric field when the wavelengths of incident laser and Stokes Raman scattering signal are close to each other.

Because the strength of the local electric field depends on the distance between the molecule and the metal surface (r) by

$E(r) \propto (1 + r/a)^{-3}$ (9)

the SERS enhancement may scale with r roughly by $(1 + r/a)^{-12}$, where a is the radius of NP. SERS intensity will decrease significantly if the distance increases (see Fig 1.5 b) [173], [174]. Therefore, the highest sensitivity in SERS measurements can be achieved when the molecules are anchored at the surface. There are several strategies for anchoring the molecules on the surface which are electrostatic and hydrophobic interactions [175], Host-guest interaction [176]–[178] and Biomolecular recognition [179]–[181].

Through the Fig 1.5b, the SERS signals can still be observed when the analyte does not directly contact with the PNP surface. This phenomenon is called a long-range effect, which is a central idea for the shell-isolated nanoparticle-enhanced Raman spectroscopy (SHINERS) method [182]–[184].

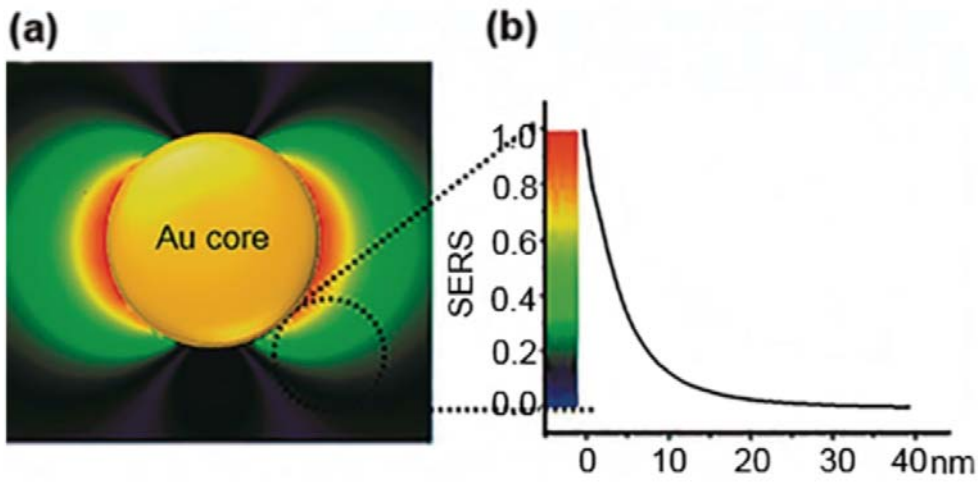

Fig. 1.5 (a) Finite difference time domain (FDTD) simulation of the electric field distribution of an AuNP. (b) Dependence of SERS enhancement on the distance from Au surfaces [185], [186].

1.2.3.2 SERS Hot Spot

The significantly substantial SERS enhancement can be created when two nanoparticles are brought close enough to each other, which is called a hot spot. The hot spots usually exist in the gaps between nanoparticle aggregates. A model to describe the highly enhanced EM field in the hot spot is shown in Fig 1.6a [172]. When two nanoparticles with a diameter of D and a gap distance of d are arranged in a uniform electrostatic field E_0 polarized along the dimer axis, the local field in the gap can be calculated to be

$$E_{loc} = E_0 (D + d)/d \quad (10)$$

The EF, i.e. (D/d + 1), can be 6.7×10^6 for D=50nm and d=1nm, which is much higher than the SERS enhancement from a single particle. Theoretical calculation of the enhancement factor of an Ag dimer with 2 nm gap ($\sim10^9$) is about 10^4 larger than that of the Ag sphere ($\sim10^5$) (see Fig 1.6b). The high enhancement makes the single-molecule detection possible [187]. Therefore, for bioanalytical research, it is essential to make the SERS substrates with high sensitivity [165], [188]–[191].

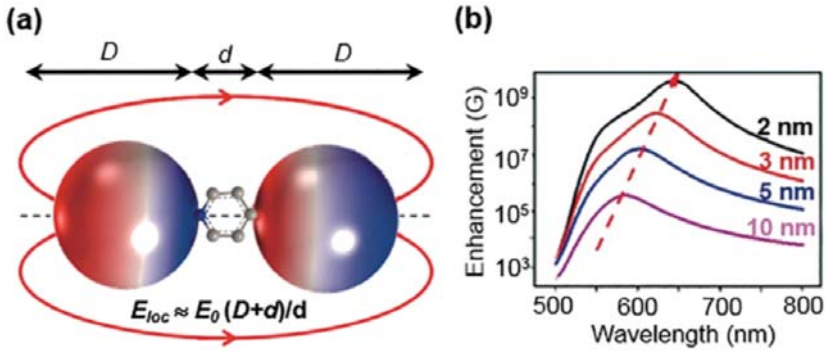

Fig 1.6 (a) Simplified model to understand the high electromagnetic field inside the gap of two nanoparticles. (b) Gap-size dependent SERS enhancement of AuNPs dimer [172].

1.2.3.3 Chemical enhancement

The chemical mechanism comes from the charge transfer between the chemisorbed species and the metal surface [192], [193]. When a molecule is covalently bound to the metal surface, the electron can be exchanged through a photo-excited electronic transition, which generates a resonance Raman process in the molecule. This transition is called a CT transition, and the enhancement of the Raman intensity by the resonance is called CT effect. Fig 1.7 shows the schematic diagram of the CT effect of SERS. Surface plasmon resonance generates the relative energies of excited electron-hole pairs via in the metal nanoparticle relative to the highest occupied molecular orbital (HOMO) to the lowest unoccupied molecular orbital (LUMO) of the chemisorbed molecule [213]. As a result, the SERS signal of a chemisorbed molecule is strongly enhanced compared with the Raman spectrum.

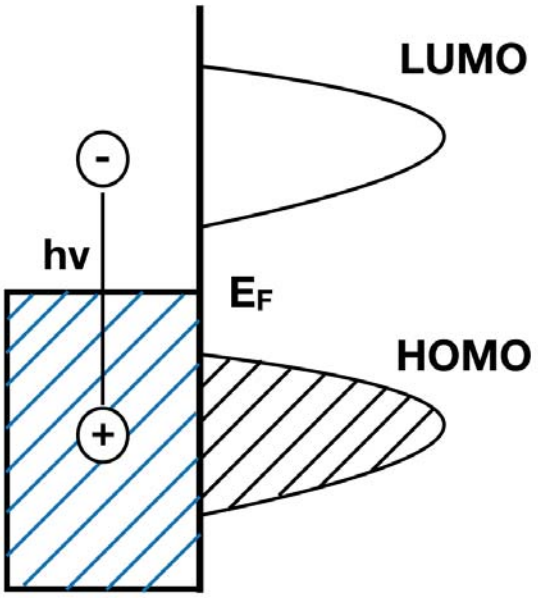

Fig 1.7 Schematic diagram of chemical enhancement of SERS.

A theory of Raman intensities based on the Herzberg-Teller coupling mechanism was presented by Lombardi et al. [194]. Both molecule-to-metal and metal-to-molecule charge transfer are included in this theory. In equation (11), term B shows molecule-to-metal charge transfer from the molecular ground state to one of the unfilled metal levels M.

$$B = \sum_{K\neq I}\sum_{k}\sum_{M\neq K}\left[\frac{M_{IK}^{\sigma}h_{KM}M_{MI}^{\sigma}}{\hbar(\omega_{KI}-\omega)}+\frac{M_{IK}^{\rho}h_{KM}M_{MI}^{\sigma}}{\hbar(\omega_{KI}+\omega)}\right]\frac{<i|k><k|Q|f>}{\hbar\omega_{MK}}+\left[\frac{M_{IM}^{\sigma}h_{KM}M_{KI}^{\sigma}}{\hbar(\omega_{KI}-\omega)}+\frac{M_{IM}^{\rho}h_{KM}M_{KI}^{\sigma}}{\hbar(\omega_{KI}+\omega)}\right]\frac{<i|Q|k><k|f>}{\hbar\omega_{MK}} \quad (11)$$

In equation (12), term c shows the metal-to-molecule charge transfer from one of the filled metal levels M to the excited state K.

$$C = \sum_{K\neq I}\sum_{k}\sum_{M\neq I}\left[\frac{M_{MK}^{\sigma}h_{IM}M_{KI}^{\rho}}{\hbar(\omega_{KI}-\omega)}+\frac{M_{MK}^{\rho}h_{IM}M_{KI}^{\sigma}}{\hbar(\omega_{KI}+\omega)}\right]\frac{<i|k><k|Q|f>}{\hbar\omega_{IM}}+\left[\frac{M_{IK}^{\sigma}h_{MI}M_{KM}^{\sigma}}{\hbar(\omega_{KI}-\omega)}+\frac{M_{IK}^{\rho}h_{MI}M_{KM}^{\sigma}}{\hbar(\omega_{KI}+\omega)}\right]\frac{<i|Q|k><k|f>}{\hbar\omega_{IM}} \quad (12)$$

where ρ and σ each represent the three spatial directions in the tensor. I, K, F to be vibronic in that they are assumed to be products of purely electronic functions with purely nuclear functions. MIM and MMK representing molecule-to-metal and metal-to-molecule charge transfer transitions to be zero.

The transition obtains its intensity via MMI through intensity borrowing from the (assumed) allowed transition I->K as shown in equation (11). Equation (12) shows that transition obtains its intensity via M_{MK} through intensity borrowing from the allowed I->K transition. The borrowing mechanism is vibronic coupling through h_{KM}. It represents the coupling of the metal to excited molecular states through some vibrational mode. From the equation (11) and the equation (12), the enhancements are considered that it comes through the resonance denominator $\omega_{MI}^2 - \omega^2$ and $\omega_{KM}^2 - \omega^2$, respectively.

1.3 Electrochemical Surface-enhanced Raman spectroscopy

The electrochemical surface-enhanced Raman scattering (EC-SERS) is like the branches of SERS study. For the characterization, EC-SERS provides useful information for revealing the adsorption configuration and electrochemical reaction of the analyte. The electromagnetic field enhancement (EM) and chemical enhancement (CE) contributes the SERS enhancement as mentioned above. The EM makes a great effort to SERS signal in most SERS system. For EC-SERS system, the CE plays an important role especially in the characterization of chemical species. There are several features of EC-SERS study which are introduced below.

1.3.1 Feature of EC-SERS

1.3.1.1 Two Fields of EC-SERS systems

When the light strike at the surface of the nanostructured electrode, there are two kinds of electric fields are generated which is an electromagnetic field (EM-field) caused by SERS process, and static electrochemical field (EC-field) lead by the applied potential of the electrode [195]. It leads to the change of orientation of the molecule and the interaction or bonding between adsorbate and surface, which influences the SERS signals.

1.3.1.2 Potential dependent characterization

For EC-SERS analysis, the applied potential on the electrode causes the change of coverage and adsorption orientation of the analyte. As shown in Fig 1.8, the 2-Amino-5-(4-pyridinyl)-1,3,4-thiadiazole is measured on the silver-nanostructure electrode with different potentials. The result shows the orientation of the molecule changes with different applied potentials, which causes the change of the SERS intensity [196].

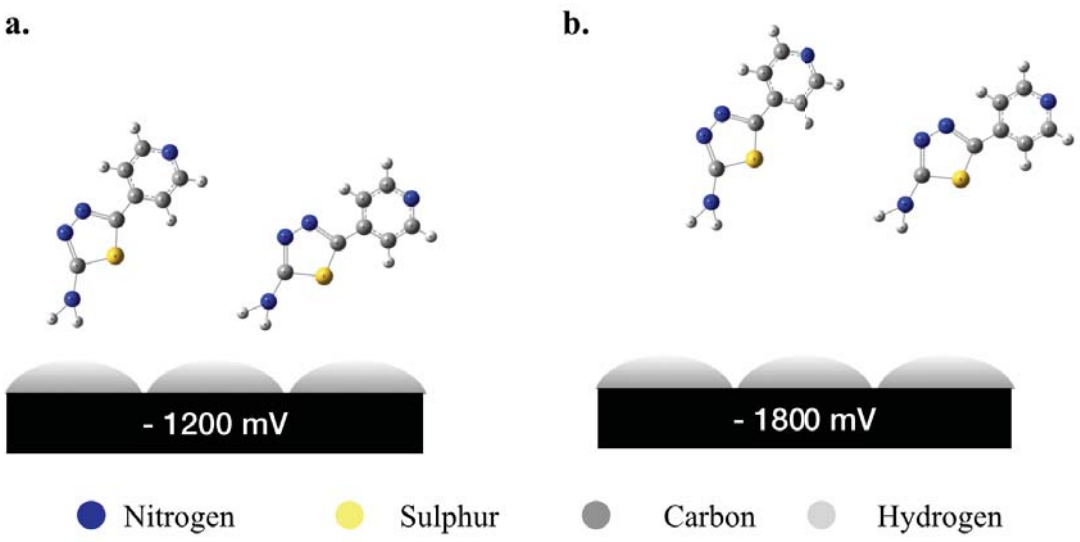

Fig 1.8. Change of the orientation of 2-Amino-5-(4-pyridinyl)-1,3,4-thiadiazole with different applied potentials of (a) -1200 mV and (b) -1800 mV.

Fig 1.9 shows the different adsorption modes of benzotriazole on an iron electrode in sulfuric acid at three kinds of applied potentials which are positive to the potential of zero charges, zero charge and negative to the potential of zero charges. The phenomenon can be observed that the negative charged atom/moiety are close to the surface when the positive potential applied on the electrode. On contrast, positive charged atom/moiety are close to the surface [197]. There are two explanations for the phenomenon which are the photon-driven charge transfer (CT) mechanism and bonding interaction of the molecule-metal surface. For the photon-driven CT mechanism, there are two directions which are metal to molecule and molecule to metal. It depends on the electrode materials, the electronic structure of the adsorbed molecules and excitation wavelength. On the other hand, in the case of bonding interaction, it

influences the geometric and electronic structure of the molecule, which leads to the change of bonding interaction.

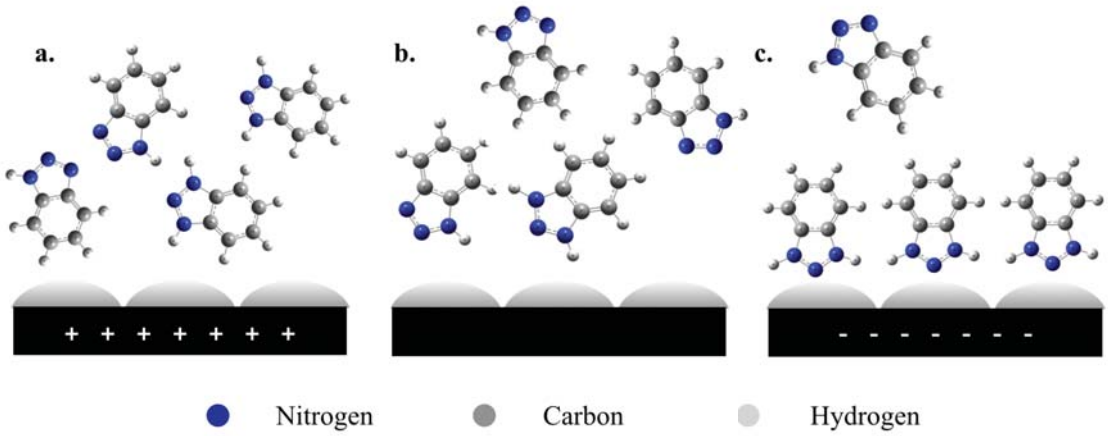

Fig. 1.9. Schematic of adsorption mode of benzotriazole on an iron electrode in sulfuric acid at potentials. (a) Positive to potential of zero charge (PZC); (b) PZC; (c) Negative to PZC.

1.3.1.3 Materials of the electrode

For most of the SERS-active substrates, coinage metals are extremely widely used. These kinds of metals support the effective surface plasmon resonance (SPR) because of the prominent optical property of free electron metals [198]. Compared with coinage metals, transition metals (VIII B element group) have different electronic band structures. It reduces the effectiveness of SPR because of the inter-band electronic transition [199]. While, some transition metals are available for the research of ultraviolet light (UV-SERS) such as Rh, Pd, Co and Ni [200]. The SERS intensities of adsorbate can be enhanced due to the strong chemisorption interaction. If the strong

binding interaction generated between molecule and transition metal surface, it might cause the change of electronic distribution of the adsorbed molecule and shift of the SPR frequency. Moreover, different enhancements for different vibrational modes will happen because of the changes of the optical electric field at the metal surface [201].

1.3.1.4 Electrolyte solutions

The EC-SERS system is also related to the electrolyte solution. The electrochemical window will be significantly expanded if organic solvents or ionic liquids are used, which eliminates the hydrogen evolution of water and also changes the oxidation potential of the electrode [202], [203]. Besides, the SPR frequency of the metal nanostructures will be shifted, which is caused by the change of the refractive index of the host solvent.

1.3.1.5 Electrochemical effects

The surface charge density of electrode is changed by applied different potentials which results in a shift in the SPR frequency. When a negative potential is applied on the electrode, it leads to the blueshift of the plasmon resonance band. By the contrary, a positive potential leads to a redshift of plasmon resonance band [313]. The following equation shows the charge density dependent plasmon frequency which can explain the shift of plasmon resonance band with different applied potentials:

$$\omega_p = 4\pi n e^2 / m\varepsilon_0 \quad (13)$$

where e and m are the charge and mass of an electron, n is the number density of free electrons, and ε_0 is the permittivity of vacuum. The change of n will lead to a shift of plasmon frequency. Besides, it will be easier to be polarized if the excess electrons exist in the conductance band. That is why the negative potential can contribute to a substantial enhancement effect than positive potential [204]–[207].

Fig 1.10 illustrates the change of SERS intensity with different applied potentials. The molecular adsorption ground state and the photon-driven CT excited state are shown in ψ_g(Vi) and ψ_{CT}(Vi), respectively. Vi notes the potential from a filled level of the metal to the LUMO of the adsorbed molecule. At the applied potential of V_1, it is insufficient to produce the photon-driven CT states on the surface. When the potential reaches V_2, the excitation energy matches the required CT energy which leads to significant enhancement of SERS intensity. If the potential negatively moves to V_3, the excitation energy does not match the ideal resonance condition which causes a decrease of the SERS signal.

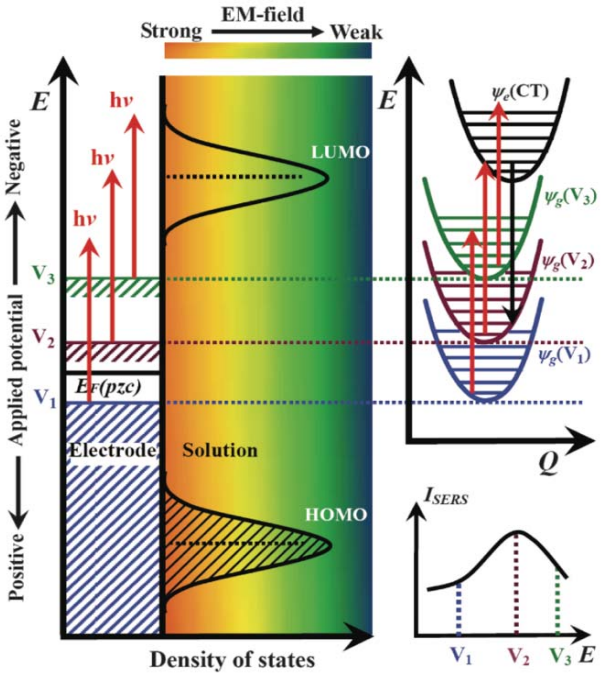

Fig. 1.10 The change of the surface vibrational energy of the adsorbate with the electrode potential [208].

1.3.2 Brief summary of EC-SERS study

Table 1 shows the EC-SERS works in recent years. The analytes are divided into three sections which are inorganic species, organic molecules, and biomolecules. The materials of nanostructure are Ag, Au, Pt, Rh, Ru, Pd, Fe, Ni, and Co. Through the EC-SERS bio-application, the meaningful information can be obtained such as chemical bonding between analyte and surface, the orientation of the analyte on the surface and electrochemical reaction of the molecule [199], [209]–[227].

Table 1.3. Partial list of SERS study related to electrochemistry

Absorption	
Inorganic species	SCN-: Ag, Au, Pt, Rh, Fe; CN-:Ag, Au, Pt; Cl-, Br-, I-:Au, Ag, Pt [199]
Organic molecules	Pyridine: all known SERS substrates [199]
	Benzotriazole, thiourea: Ag, Au, Pt, Pd, Rh, Ru [199]
	Pyrazine: Ag, Au, Pt [199]
	Benzene: Ag, Au, Pt, Pd, Rh, Ru [209]
	Imidazole: Fe, Ni, Co, Ag [210]
	Benzenethiol: Ag, Au, Pt [211]
	Mercaptopyridine: Ag, Au [212]
	Conducting polymers: Au, Ag; polypyrrole, polythiophene, polyaniline, polyacetylene [213]
	Dyes: Au, Ag: R6G [214], Crystal violet [215], nile blue [216], N719 dye [217]
Biomolecules	Ag: Cyt c [218], hemoglobin [219] , enzymes [220], uric acid [221], amino acids [222], DNA bases [222], melamine[223], aminoglutethimide [224]
	Au: hemoglobin [219], ssDNA [225], dsDNA[225], oligonucleotide [210], anti-IgG [226], bilayer lipid membrane [227], NADH [210]

Chapter 2. Fabrication of SERS-active Electrode

2.1 Introduction

2.1.1 Nanofabrications for SERS-active substrates

Researchers have developed many types of metallic nanostructures (NS) by advanced nano-processing technology as SERS-active substrate. Fig 2.1 highlights some milestones in the development of nanostructured SERS-active substrates. Generally, NSs strategies for manufacturing can be classified as top-down, bottom-up, or combinatorial techniques, which are summarized in Table 2.1. Details of these techniques are as follows.

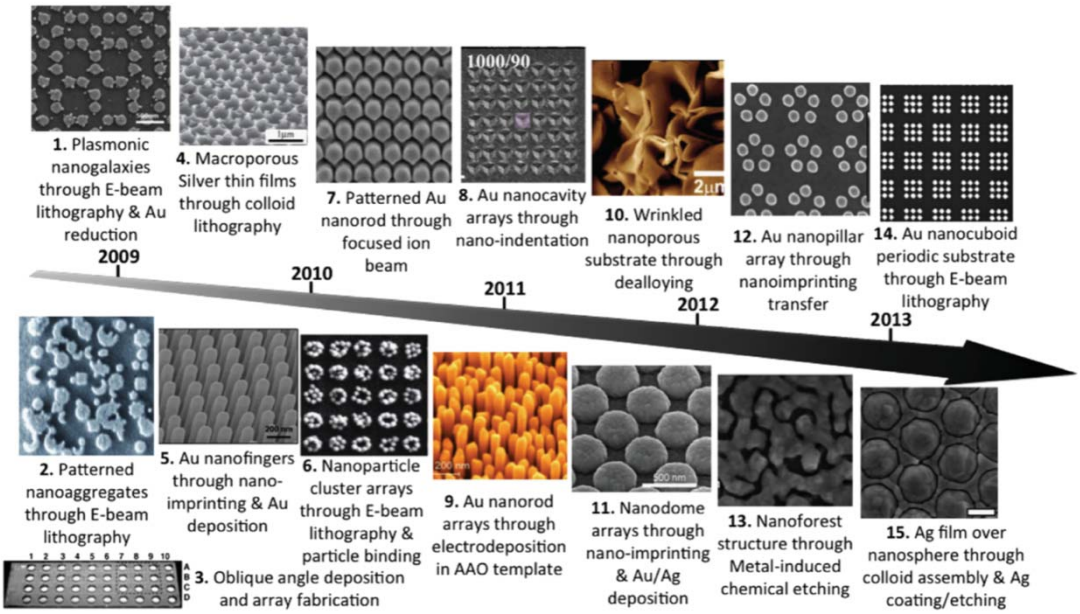

Fig. 2.1. Nanofabrication used for fabricating SERS-active substrates in which [1] from [228], [2] from [229], [3] from [230], [4] from [231], [5] from [232], [6] from

[183], [7] from [233], [8] from [234], [9] from [235], [10] from [236], [11] from [237], [12] from [238], [13] from [239], [14] from [240], [15] from [241].

2.1.1.1 Top-down techniques

Although limited by production cost and speed, electron beam (E-beam) lithography is still one of the most commonly used SERS active substrates, as it provides a well-controlled nanoscale pattern. As shown in Fig 2.1, E-beam lithography with combinatorial spectral was used to generate Au arrays of randomly generated cells with different morphologies by Wells et al. Lin et al. applied focused ion beam (FIB) and nanoindentation to fabricate nanostructured Au substrates, as shown in Fig 2.1 (7 and 8) [234]. The FIB technique was used to precisely fabricate patterned Au nanorods (NRs). As shown in Fig 2.1 (12), Yang et al. developed an Ar-ion sputtering path for manufacturing Ag nanoneedle arrays on a silicon substrate [239]. Dense Ag nanoneedle arrays and sharp tips have made it possible to reproducibly achieve an average SERS potentiator (EF) of more than 10^{10}. As shown in Figure 2.1 (13), the incomplete cover of the Au layer can selectively lead the chemical etchant, resulting in a nano-forest substrate which was demonstrated by Seol et al. The EF of these substrates was not extraordinarily high, but this etching technique enables high throughput nanofabrication compared to other top-down technique [239].

Table 2.1. Fabrication technique, metal surface, and average EF for four approaches to fabricate metal nanostructures.

Nanofabrication	Techniques and Methods	Average enhancement	Metals
Top-down fabrication	E-beam lithography	5 x 10^8	Au
	Focus ion beam	1 x 10^7	Au
	Nano-indentation	5.85 x 10^7	Au
	Metal-induced chemical	1 x 10^7	Au
	Ar ion sputtering	1 x 10^10	Ag
Button-up assembly	Nanoparticle Immobilization	1 x 10^6	Au
	Oblique angle deposition	1 x 10^9	Ag
	Galvanic displacement	1 x 10^8	Au
Combination	E-beam lithography + Au reduction	1 x 10^8	Au
	Dealloying + thermal treatment	3 x 10^8	$Au_{79}Ag_{21}$
	E-beam lithography + particle binding	1 x 10^8	Au
	UV-lithography + OAD	1 x 10^6	Ag
Template-assisted fabrication	ZnO nanowires	2.19 x 10^6	Au
	Nanoimprinted polymer	1 x 10^10	Au
	Anodic aluminum oxide	1 x 10^9	Au
	Carbon nanotube	1 x 10^7	Au
	Colloid assembly	1 x 10^7	Au

2.1.1.2 Bottom-up techniques

Compared with most top-down methods, the bottom-up approach is usually relatively simple and low cost. High throughput can also be easily achieved. However, due to the low reproducibility, it is not easy to predict the location of hot spots and EFs. The most straightforward is to fix the Au NPs to the substrate surface to a height of 10^6 [242]. As shown in Fig 2.1 (3), Abell et al. integrated these assemblies into a multi-well array for virus observation [230]. Researchers have fabricated interesting Au and Ag NSs on various metallic substrates, such as Fe [227], Cu [229], Si [239] and Al foils.

Compared to other manufacturing techniques, the galvanic displacement reaction is simple and cost-effective.

2.1.1.3 Combination techniques

Manufacturing techniques that combine the advantages of top-down and bottom-up technique have been developed. Gopinath et al. produced plasmonic nano galaxies and the first hybrid multiscale aperiodic NS. Nanocylinder was fabricated by E-beam lithography. As shown in Fig.1 (6), Yang et al. combined E-beam lithography and immobilization of Au NPs to fabricate an Au NPs cluster arrays [232]. Through this method, the enhancement factor reaches 10^8. Nanoporous $Au_{79}Ag_{21}$ films with a bicontinuous network structure using non-alloying method were introduced by Liu et al. [240]. As shown in Fig. 1 (10) [236], the nanoporous films were treated with heat shrinkage of the predicted polymer substrates. The EF is larger than 10^9.

2.1.1.4 Template-assisted fabrication

Template-assisted manufacturing has been used to create various NSs which is also widely used in the manufacture of SERS active substrates. Anodized aluminum oxide (AAO) is one of the most commonly made through template-assisted fabrication. There are several ways for making SERS-active substrate through metallic salts [250], evaporation deposition [251], and electrochemical deposition [235]. Ag films over nanosphere (AgFON) substrates are also widely used for SERS-active substrates [252]–

[254]. Self-assembled nanoring cavity arrays based on AgFON is introduced by Im et al. which is shown in Fig. 1(15) [241]. The average EF of cavity arrays is near 10^8 [255].

2.1.2 SERS-active Screen-Printed Electrode (SSPE)

Screen printed electrodes (SPE) is not only taking advantage of cost-effectiveness but also meeting the demands of portability. The versatility of screen-printed electrodes is of essential importance in the field of analysis, the technique to modify electrodes with efficiency through various inks commercially feasible for the reference, counter and working electrode, supports for highly specific and finally calibrated electrodes to be fabricated for particular target analytes [257]–[259]. Many classifications of screen-printed electrode applications exist for environmental monitoring, proteins, enzymes and DNA sequences [260]–[263]. Screen printed electrodes are portable, simple handling, economical analytical methods [264]. Consequently, screen printed electrodes can be efficiently applied for in situ environmental monitoring to accomplish improved achievement, as has been illustrated over the past several years.

SERS-active screen-printed electrode (SSPE) technology, for portable spectroelectrochemical detection, is rapidly developing and has been widely used in a range of applications such as detection of melamine, pyridine, biodegradable ionic liquids, and DNA as well as in a biomimetic membrane [219], [265]–[267]. The most popular way of preparing SERS-active SPEs is based on the classical citrate reduction method proposed by Lee and Meisel [266], [268], [269]. In brief, silver nitrate solution, sodium citrate and citric acid are added into water. After centrifugation, the silver

nanoparticle can be obtained, and then drop coated onto the working electrode. This is indeed an effective and low-cost way of fabricating SERS-active electrodes. However, undesired SERS background noise that comes from the trace citrate molecules limits the adsorption sites and interferes with the detection of analytes. As an alternative, the sputtering method was employed for fabricating the SERS-active SPEs. A low background signal has been observed from the fabricated electrode, and a high signal-to-noise ratio can be expected. Besides, larger surface adsorption area for target molecules is present, and further surface modification can be quickly done if desired.

2.2 Fabrication of SSPE by Sputtering deposition

We proposed a rapid and highly productive way to fabricate SSPE by sputtering deposition. The coating process time for one batch coating was within 15 minutes, and more than ten thousand silver-deposited electrodes were able to be fabricated per hour. Also, sputtering method guaranteed low SERS background signal and a maximum of surface absorption for target analytes because there was no other material but pure silver directly deposited on the working electrode. To our knowledge, this is the first work of fabricating SERS-active SPEs through sputtering coating method among any other EC-SERS studies.

Before sputtering deposition, the plastic specially-made mask was covered on the electrode with a hole on the working electrode which was the only area needed to be deposited. The diameter of the hole on the mask was slightly smaller than the diameter

of working electrodes which prevented from the cases of the silver being deposited onto the reference electrode or counter electrode.

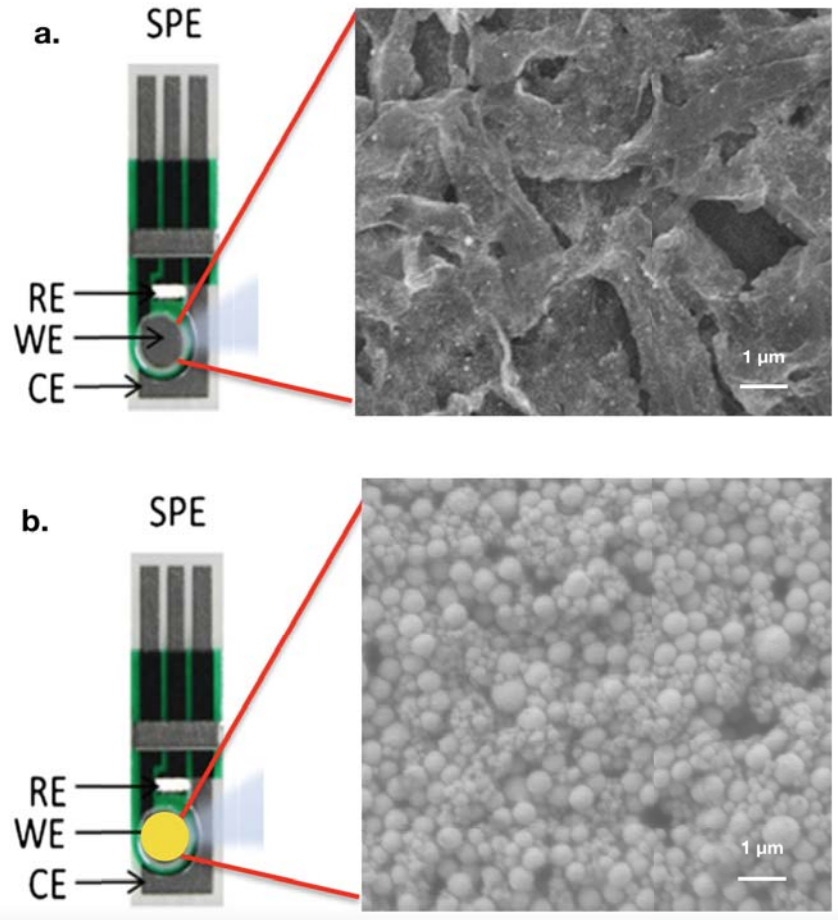

Fig. 2.2. The photo of SPE used in this work which is composed by working electrode (WE), counter electrode (CE) and reference electrode (RE). SEM image of two different materials of working electrodes which are made by a) carbon and b) gold.

The SPEs are supplied by BioDeviceTechnology (Japan). The SPE consists of a reference electrode (Ag / AgCl), a counter electrode (carbon) and a working electrode (carbon/gold). There were two kinds of material of working electrode which were

carbon (Fig 2.2a) and gold (Fig 2.2b). The customized mask mounted the SPEs in order that only the working electrode areas were exposed for sputtering deposition.

Table 2.2. Design of experiments for silver sputtering deposition on carbon SPE

DOE	Vacuum level (Pa)	Target Power (W)	Deposition time (sec)	Ar Gas flow (sccm)	Results
1	8 x 10 ^ -4	500	24	200	Film structure
2	8 x 10 ^ -4	500	16	200	Film structure (rare gaps)
3	8 x 10 ^ -4	500	12	200	Film structure (Less gaps)
4	8 x 10 ^ -4	500	4.8	200	Film structure (many gaps)
5	8 x 10 ^ -4	250	24	200	Film structure (Less gaps)
6	8 x 10 ^ -4	250	16	200	Film structure (many gaps)
7	8 x 10 ^ -4	250	12	200	Island structure
8	8 x 10 ^ -4	250	4.8	200	Island structure (few nanoparticles)
9	8 x 10 ^ -4	50	24	200	Island structure (few nanoparticles)
10	8 x 10 ^ -4	50	16	200	Island structure (few nanoparticles)
11	8 x 10 ^ -4	50	12	200	None
12	8 x 10 ^ -4	50	4.8	200	None

The silver-deposited SPEs were prepared by using the in-line sputtering machine of Optorun.Co.Ltd (Japan) which was shown in Fig 2.3. The target power was set to 100 kW, 250 kW and 400kW for the sputtering process. The deposition time of the sputtering process was 4.8 s, 12 s, 16.8 s and 24 s, which was shown in Table 2.1. Considered avoiding to melting carbon electrode and plastic masks, the whole sputtering process was under the temperature of 50 ℃. Since the surface roughness on working electrode of SPEs was challenging to be directly analyzed by an ellipsometer, as reference, planar and smooth quartz glasses were fitted nearby the SPEs for each coating processes.

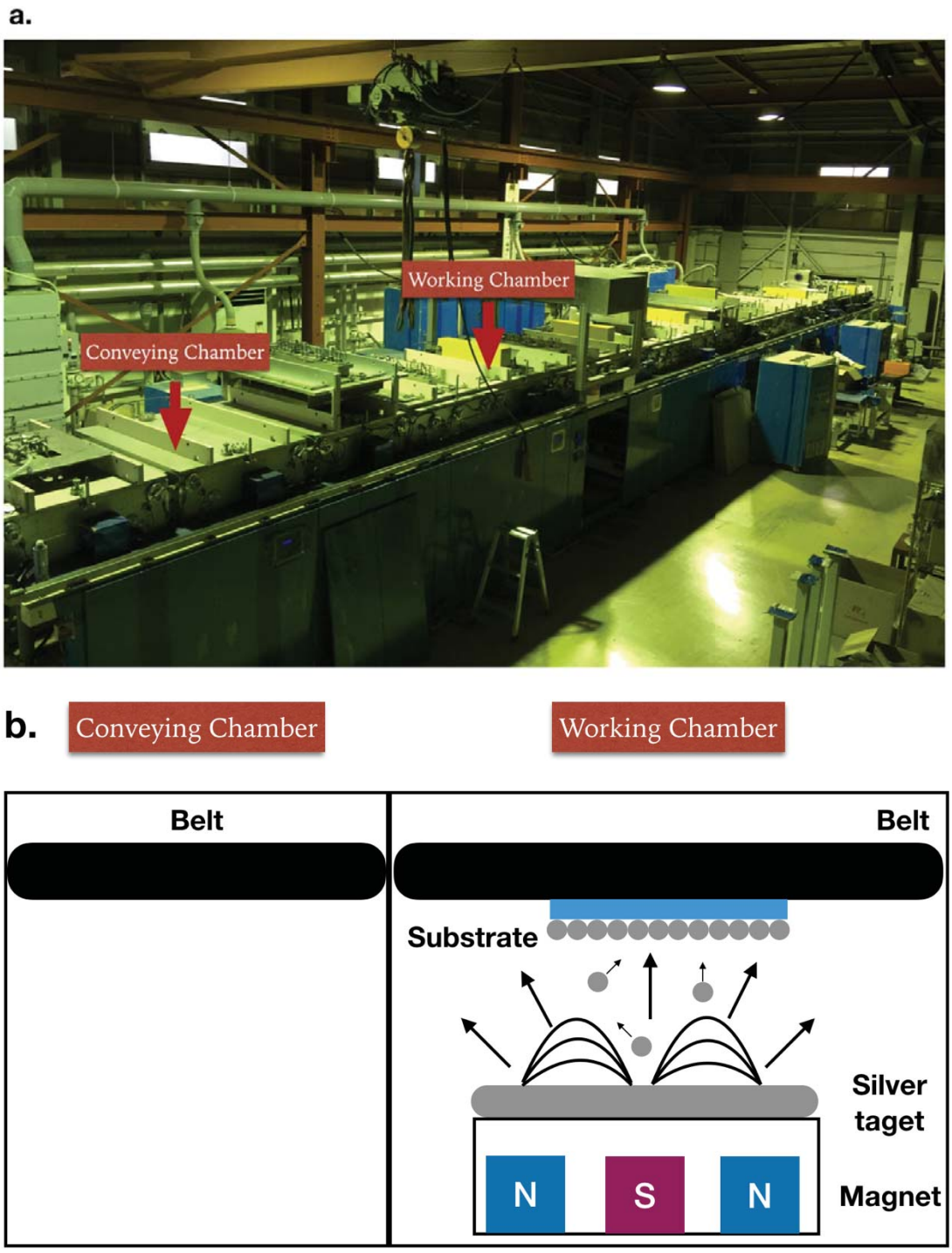

Fig 2.3. a) V0005 in-line sputtering machine. b) Schematic figure of V0005 in-line sputtering machine.

2.3 Fabrication of SSPE on different substrate

In order to investigate the applicability of the sputtering method for producing SERS-active SPEs, three different substrates of SPE were used for the sputtering process which was paper, glass epoxy and polyethylene terephthalate (PET) as shown in Fig 2.4. Besides, the different structure of SPE with micro-chamber was also deposited by silver film and analyzed at the next chapter..

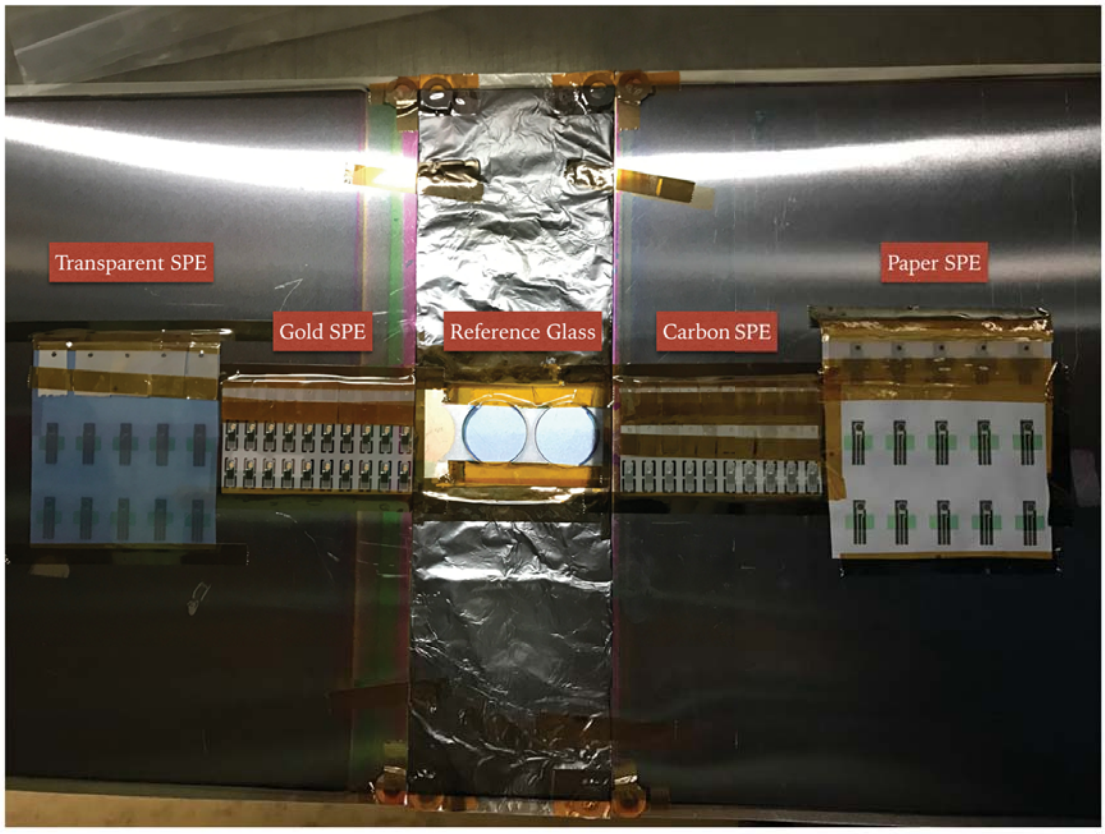

Fig 2.4. Silver-deposition on the screen-printed electrodes with different substrate.

2.4 Results and discussion

2.4.1 SEM and AFM images

In our previous observation, we noticed that when charging the silver target with high power (500 W), island structure became difficult to form due to the high depositing rate of silver atoms. Besides, high kinetic energy atoms led to an increase in temperature on the substrate which might damage the surface of the working electrode. On the other hands, with the low target power (50 kW), it would be difficult to deposit silver onto the substrate due to the low kinetic energy of the silver atoms. Therefore, the power applied for the silver target was adjusted to a well-optimized condition.

Raw a

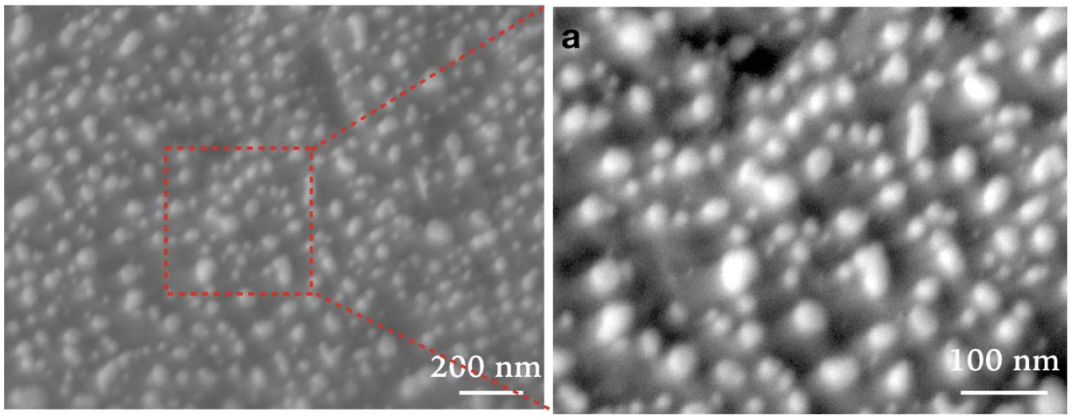

Raw b

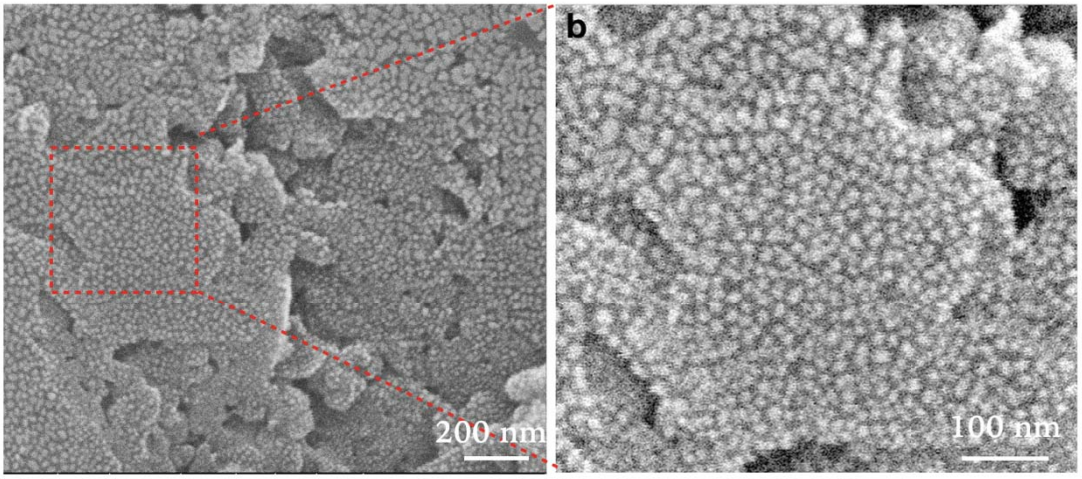

Raw c

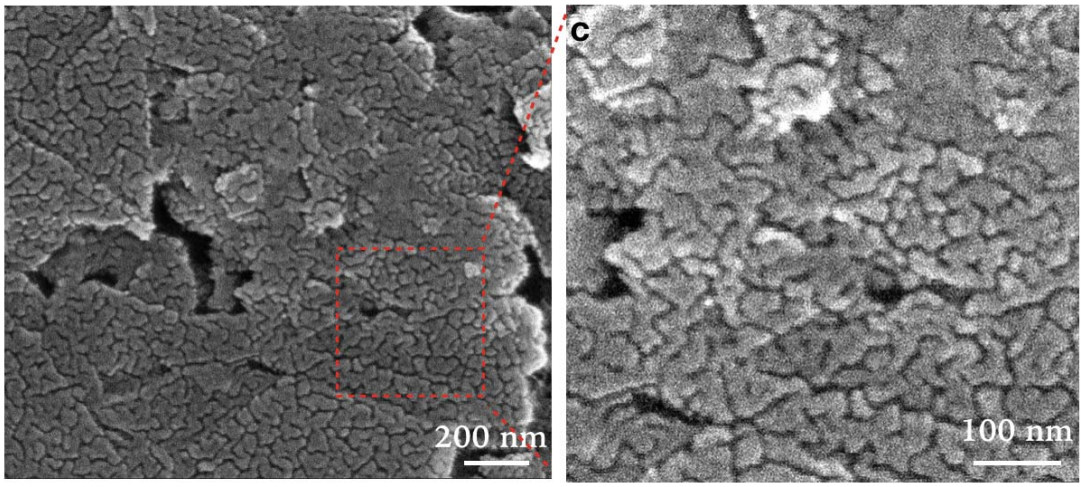

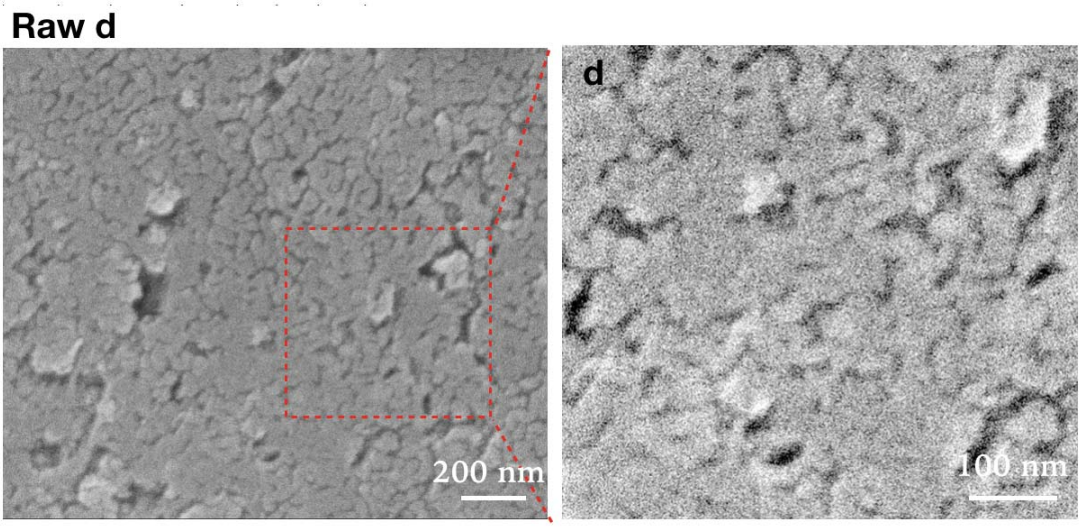

Fig 2.5. SEM raw images of 200 k magnification ratio of silver-deposited carbon working electrodes with different deposition time of (Raw a) 4.8 s, (Raw b) 12 s, (Raw c) 16.8 s and (Raw d) 24 s, which corresponding to the zoom out images (a), (b), (c) and (d), respectively. Silver target power of sputtering deposition: 250 kW. E-beam of SEM image: 12 kV.

JEOL JSM-7500FA was used for SEM analysis of silver-deposited film on the SPEs. The SEM images of a bare carbon electrode and Ag deposited carbon electrode were shown in Fig 2.2a and Fig 2.5. By glancing Fig 2.5 from left to right, the growth of the Ag films thicknesses on the carbon electrode could be observed. The island formation which looked like Ag nanoparticles was observed on the Fig 2.5a and Fig 2.5b, while, for the Fig 2.5c and Fig 2.5d, the gaps among Ag nanoparticles were gradually filled up and formed into the silver film structure. Compared with Fig 2.5a, Ag nanoparticles of Fig 2.5b were more aggregated and extremely close to each other. The quantities and diameter of deposited Ag nanoparticles were estimated as follow:

assuming N stands for surface coverage of Ag nanoparticles, there were approximately 14 nanoparticles / $(100\ nm)^2$ = 14 x 10^{14} N / m^2 of Fig 2.5a and 25 nanoparticles / $(100\ nm)^2$ = 25 x 10^{14} N / m^2 of Fig 2.5b. The sizes of Ag nanoparticles of Fig 2.5a were hugely inconsistent that the diameter of bigger nanoparticles reached 25 nm while the diameters of smaller ones were less than 10 nm.

On the other hand, diameters of Ag nanoparticles of Fig 2.5b were relatively uniform which were observed in a range from 20 nm to 30 nm. The Ag-deposited film structures of the gold working electrode shown in Fig 2.6 were similar to those of carbon working electrode. The island structure could be observed through 12 s sputtering deposition shown in Fig 2.6b. With longer deposition time, silver nanoparticles progressively formed into the film structure shown in Fig 2.6c and Fig 2.6d.

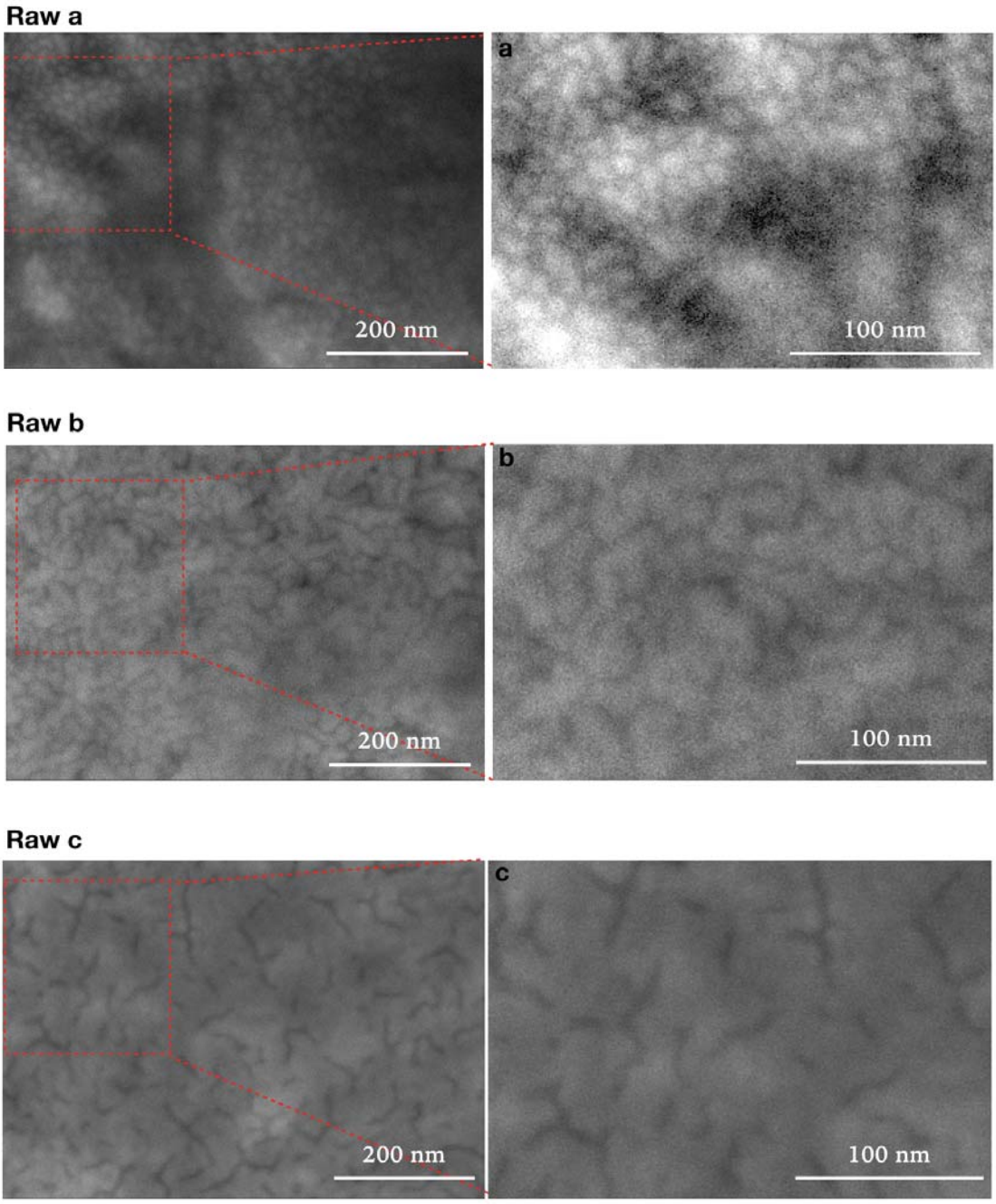

Fig 2.6. SEM raw images of 200 k magnification ratio of silver-deposited gold working electrodes with different deposition time of (Raw a) 12 s, (Raw b) 16.8 s and (Raw c) 24 s, which corresponding to the zoom out images (a), (b) and (c), respectively. Silver target power of sputtering deposition: 250 kW. E-beam of SEM image: 5 kV.

Atomic force microscope (SPA400-AFM, Seiko Instruments Inc., Japan) was used for analyzing the surface of the SERS-active SPE which was equipped with a calibrated 20 μm xy-scan and 10 μm z-scan range PZT-scanner. All AFM images were taken in dynamic force mode (DFM mode, i.e., tapping mode) at optimal force. A silicon cantilever (OMCL- AC160TS, OLYMPUS), which has a spring constant of 42 N/ m and a frequency resonance of 300 kHz, was also used for imaging in the air at room temperature. The cross-sectional image of the bare working electrode and silver-deposited working electrode were obtained by an Atomic Force Microscope (AFM) which was shown in Fig 2.7a and Fig 2.7b, respectively. Compared with the cross-sectional image of the bare electrode, the roughness was considered which mainly came from the screen-printed electrode. Through the AFM and SEM images, it was possible to estimate for the size and the shape of the single silver nanoparticle (particle size: approximately 24 nm for diameter and 4 nm for height averagely). By inspecting the whole area, the shape of the cross-section appeared to be irregular, and the roughness increased to over 13 nm which might be caused by the roughness of SPE. In conclusion, because the roughness of the SPE substrate is larger than that of the silver nanoparticle, it is considered that the roughness of the cross-sectional image mainly comes from the SPE substrate rather than the silver nanoparticles.

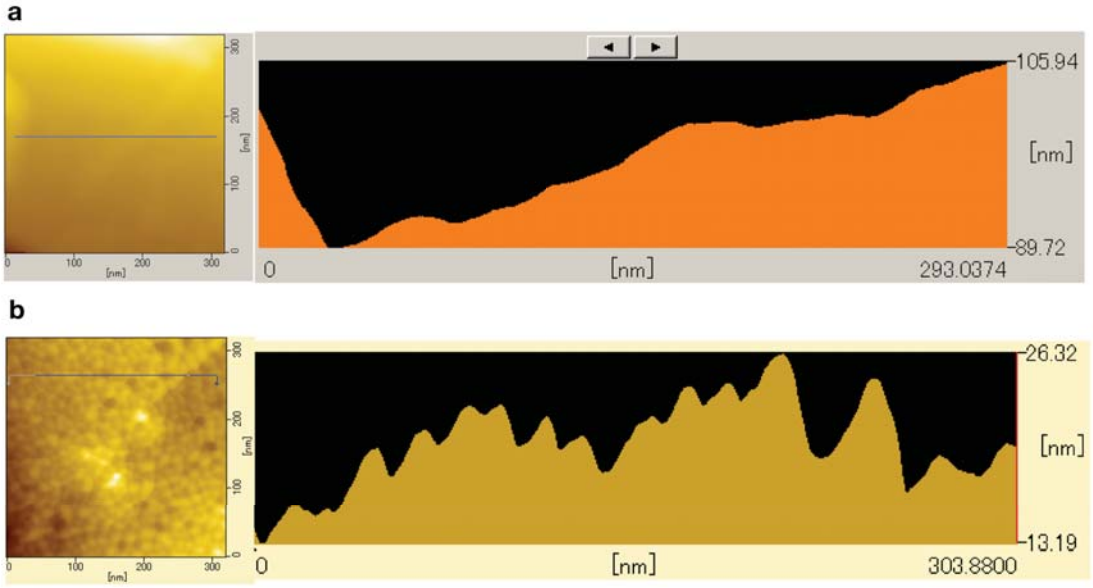

Fig. 2.7. The cross-sectional image of (a) bare carbon working electrode and (b) silver-deposited carbon working electrode. The diameters of silver nanoparticles range from approximately 20 nm to 30 nm.

2.4.2 Evaluation of silver film

Regard to the evaluation of silver film, it is difficult to directly evaluate the deposited silver film on the carbon SPEs through ellipsometry measurements because of the roughness of SPE. However, it is able to correctly estimate the deposited silver film on the flat and smooth glass substrate. Fig 2.8 showed two proposed models of different Ag film thicknesses on the reference glasses which were placed nearby the SPEs during the sputtering processes. We can see that the substrate of Model b. (Fig 2.8) has acquired enough nanoparticles to create a layer of thin film, contrary to the substrate of Model a. which merely has acquired a gathering of nanoparticles. For these two situations, the refractive indices (n) and extinction coefficients (k) were different.

The complex refractive index of surface roughness is like the case of Model b. Effective medium approximation (EMA) method is widely applied which can make calculation relatively easier. EMA pertains to analytical or theoretical modeling that develops from averaging the multiple values of the constituents. At the constituent level, the values of the materials vary and are inhomogeneous. EMA produces acceptable approximations which can describe useful parameters and properties of the composite material overall. Therefore, EMA is descriptions of a medium (composite material) based on the properties and the relative fractions of its components and are derived from calculations. The EMA method can be expressed by the following equation [270]–[272]:

$$f_a \frac{\varepsilon_a - \varepsilon}{\varepsilon_a + 2\varepsilon} + (1 - f_a) \frac{\varepsilon_b - \varepsilon}{\varepsilon_b + 2\varepsilon} = 0 \quad (14)$$

In equation 1, f_a and $(1\text{-}f_a)$ represent the volume fractions of phases a and b which complex dielectric constants are ε_a and ε_b, respectively. There are two solutions in this quadratic equation. One solution can typically be considered as a physically sensible solution; the other solution is generally negative or has other unphysical features [273]. The calculation result of the refractive index and extinction coefficients by the EMA method were shown in Fig 2.8.

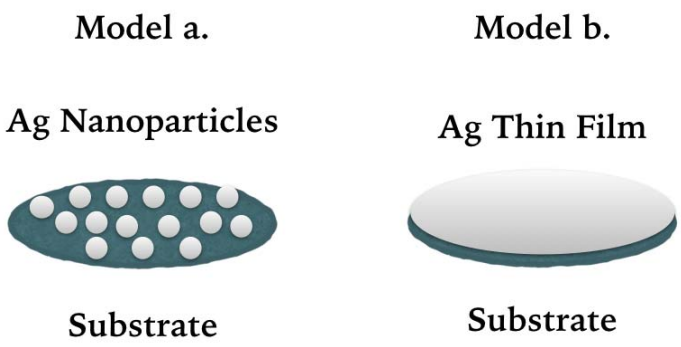

Fig 2.8 Two proposed models of different structures of Ag-depostied film on the reference glass substrates. Model a. island formation looked like Ag nanoparticles on the glass substrate; Model b. Ag thin film on the glass substrate.

The ellipsometer of SEMILAB SE-2000 and fitting software of Spectroscopic Ellipsometer Analyzer were used to analyze the surface roughness on the substrate. The refractive index and extinction coefficient were estimated by the EMA method, and the results were shown in Fig 2.9. The measuring and fitting results were shown in Fig 2.10. The parameters used in the simulation are shown in appendix a and appendix b. The measuring curve of 24 s silver-deposited film and fitting curve of 10 nm film were almost overlapped which mean the thin film model we assumed in Model b. of Fig 2.8 closed to the coating result. Compared with the fitting results of 24 s silver-deposited film, the measuring curve of 12 s silver-deposited film and fitting curve of 5 nm film were not great consistency. The reason for unperfected fitting was considered that the random distributions and inconsistent sizes of Ag nanoparticles on the surface caused, to some extents, the difference between

calculated refractive indices and the actual coating results. While Ψ and Δ fitting results of 5 nm film were consistent with the measuring results. According to the measuring results, the thickness error was only 0.2 nm.

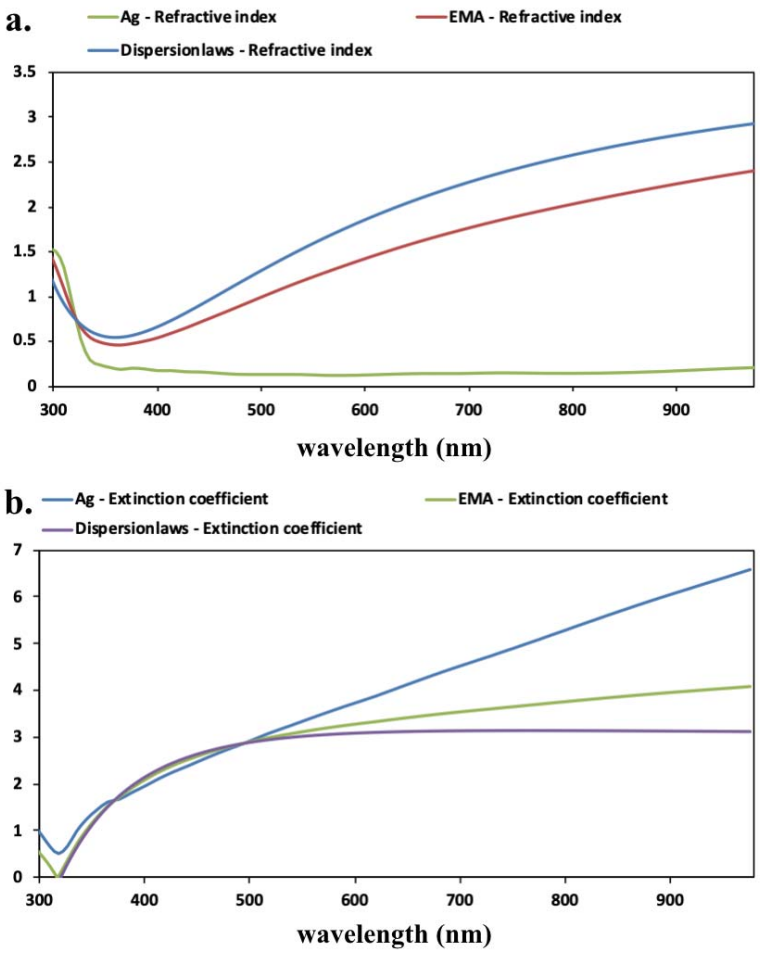

Fig 2.9. Refractive index (a) and extinction coefficients (b) calculated by EMA method.

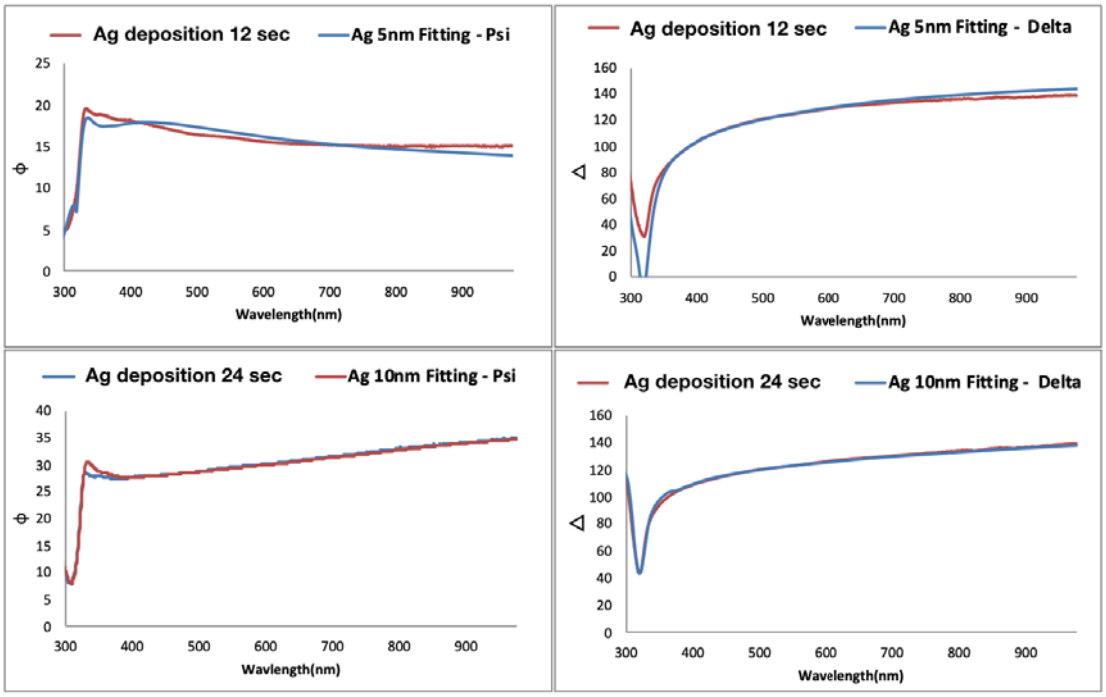

Fig 2.10. Measuring and fitting results of amplitude component Psi(Ψ) and phase difference Delta(Δ) of 5nm and 10nm Ag thin films.

To verify the reproducibility of silver nanostructure deposited by the sputtering method, five continuous batches of 12 s silver deposition experiments were conducted, and the analysis by ellipsometer was shown in Fig 2.11. The thicknesses errors of these five coating experiments were ±0.1 nm, which not only demonstrated satisfying reproducibility by silver deposition but also showed the applicability and feasibility of sputtering depositing method for fabrication of SERS-active electrodes.

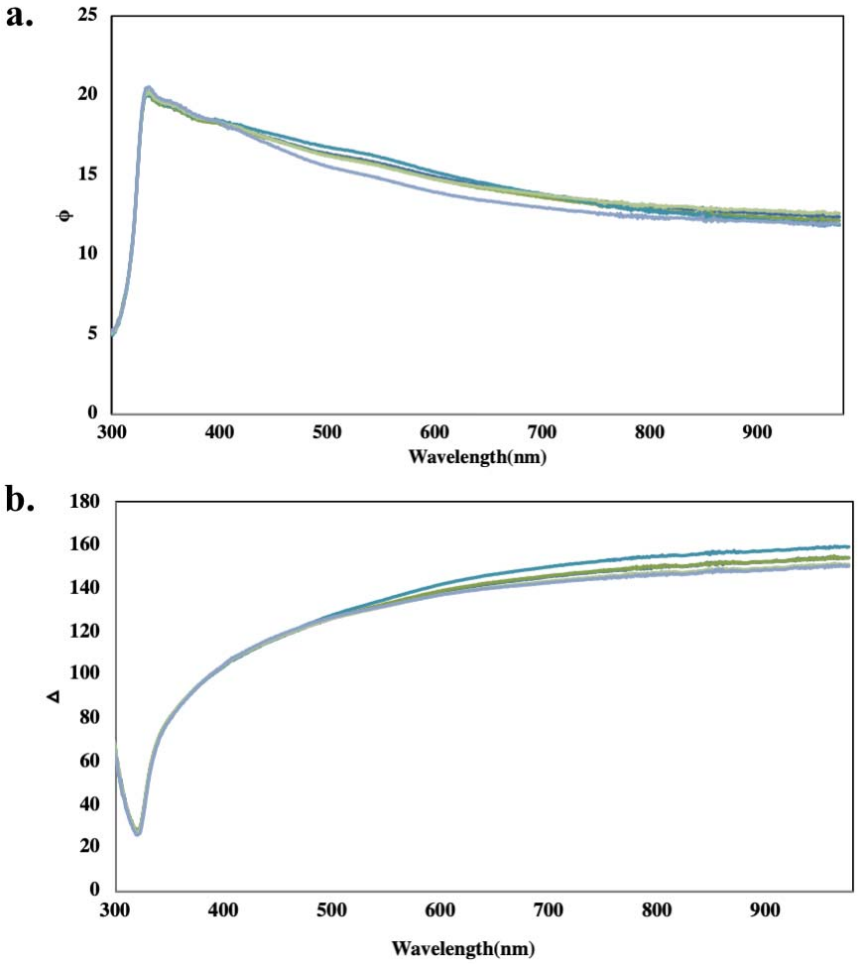

Fig 2.11. Measuring result of a) amplitude component Ψ and b) phase difference Δ of continuous five batches 5nm Ag deposition on reference glasses.

2.4.3 Comparison of SERS signal

The Raman spectra and Raman images were obtained with a laser Raman confocal microscope (RAMAN-11, Nanophoton, Japan) equipped with a Nikon 100X, NA = 0.9 objective lens and an Olympus 20X, NA = 1.0, water-immersion objective lens, which were used for measuring the Raman spectral of AGI power and E-SERS spectral of AGI in solution, respectively. The sample was illuminated with a line-shaped laser (532

nm was about 2.8 mW / line (400 pixels) focused through the objective lens. The same objective lens collected Raman scattering from the samples and guided to a spectrophotometer with a slit width of 15 μm. The Raman signal was diffracted by a 600 grooves/mm grating (spectra resolution, 1.6 cm^{-1}) and detected by an air-cooled CCD camera (-70 ˚C). Raman spectra were obtained from 1.25 μm x 167 μm (3 x 400 pixels) area.

The SERS experiments were conducted to reveal the relationship between surface roughness and enhancements of the SERS signal. The solution of 100 μM R6G was dropped and dried on the carbon working electrodes of different surface roughness as shown above (Fig 2.5a, Fig 2.5b, Fig 2.5c, and Fig 2.5d) which corresponding to the sputtering deposition time of 4.8 s, 12 s, 16.8 s and 24 s. The absorption spectra of the 12 sec and 24 sec Ag-sputtered film were shown in Fig 2.12. Combined with Fig 2.5, the silver island structure of 12 sec sputtering deposition generates the surface plasmon resonance, which leads to stronger absorption than that on the 24 sec Ag-sputtered film.

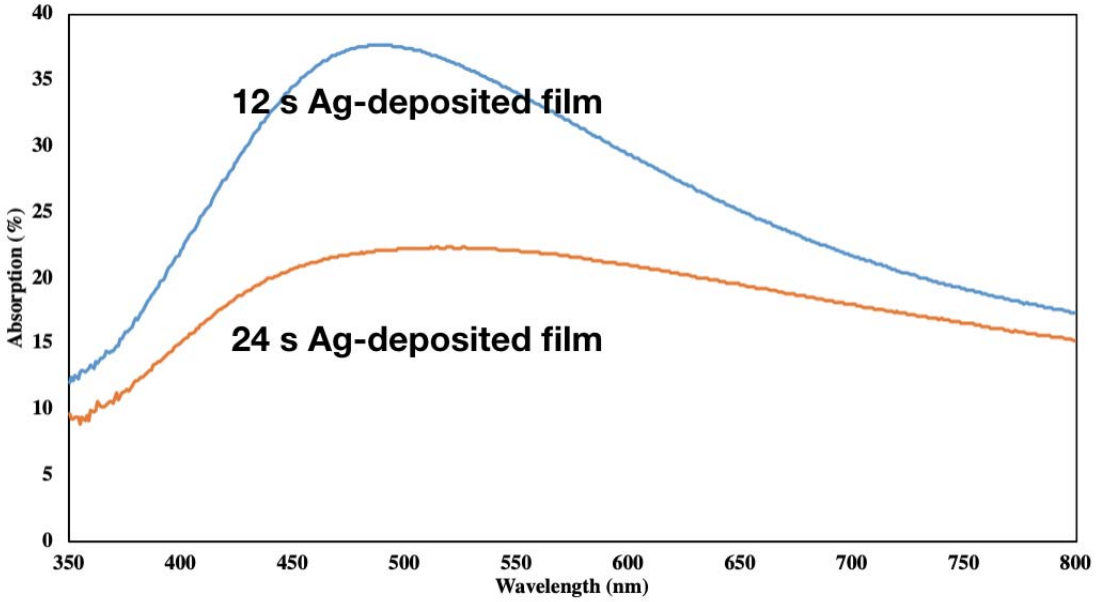

Fig 2.12. Absorption spectra of the 12 second and 24 second Ag-sputtered film.

The fluorescence intensity of R6G adsorbed on the SERS-active carbon electrode was shown in Fig 2.13, and the SERS spectra were shown in Fig 2.14a. According to the Raman spectra, the peaks at 1315 cm^{-1}, 1366 cm^{-1}, 1513 cm^{-1}, 1581 cm^{-1}, and 1654 cm^{-1} were assigned to the C-C stretching vibrational mode of the aromatic ring; the peak at 778 cm^{-1} was assigned to the C-H out-of-plane bending vibrational mode; the peak at 1188 cm^{-1} was assigned to the C-H in-plane bending vibrational mode. The peak at 617 cm^{-1} was assigned to the C-C-C ring in-plane vibrational mode. These band assignments were shown in Table 2.3 which were in good agreement with the previous reports [274].

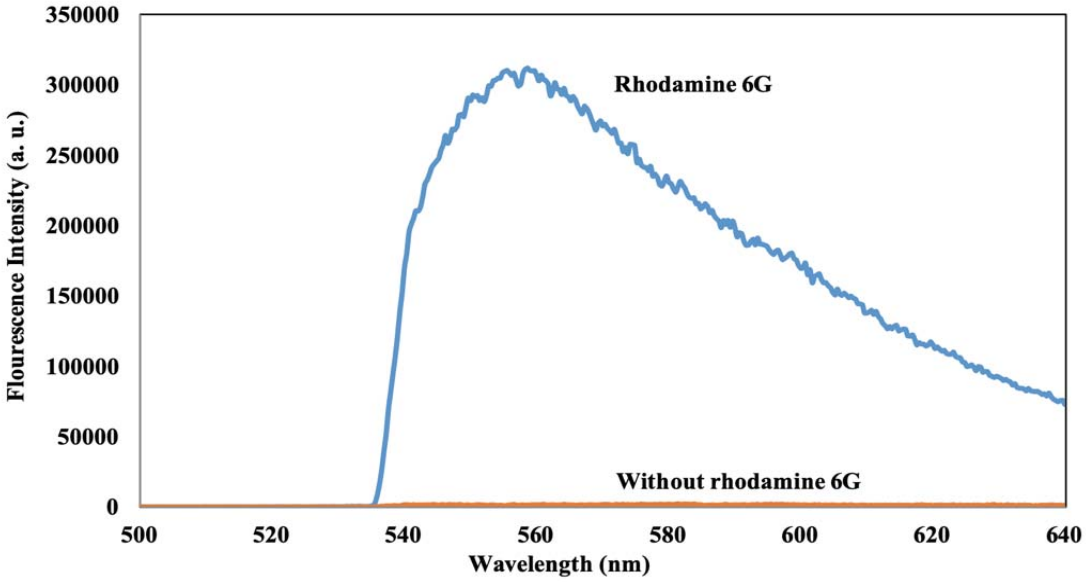

Fig 2.13. Fluorescence intensity of R6G on the SERS-active carbon electrode.

The SERS peaks of R6G were obtained at the 12 s, 16.8s and 24 s Ag-deposited film structure corresponding to the images of Fig 2.5b, Fig 2.5c, and Fig 2.5d. While combined with Fig 2.14a, there were no apparent peaks on the bare carbon electrode and 4.8 s Ag-deposited film structure corresponding to the images of Fig 2.5a. The results implied that the sparse Ag nanoparticles on the electrode like the case of Fig 2.5a were not benefited to the increases of SERS signals. Contrarily, for Ag-deposited films structure of Fig 2.5b, the surface of concentrated Ag nanoparticles benefited the increase of SERS signals. It is considered that more R6G molecules were absorbed to contribution to SERS signals due to more silver nanoparticles of Fig 2.5b than those of Fig 2.5a. When the deposition time increased, the gaps among Ag nanoparticles were gradually filled up, and silver nanoparticle became the silver film structure like Fig 2.5c and Fig 2.5d. As a result, the decrease of surface

roughness led to the weakening of SERS signals of each peak which could be conveniently observed through Fig 2.14b and Fig 2.14c. In conclusion, the concentrated nanoparticle structure was better than sparse nanoparticle structures and film structures for the enhancement of Raman signals, which could explain that the most enhanced Raman signals were observed on the surface roughness of Fig 2.14b. Similarly, on the Ag-deposited gold working electrode, the most enhanced SERS signals could be observed at 12 s Ag-deposited film structure shown in Fig 2.15b and Fig 2.15c, and the SERS signals became weakening with the increase of silver deposition time.

Table 2.3. Raman band assignment of Rhodamine 6G

Wavenumber (cm-1)	Assignment
617	C-C-C ring in-plane
776	C-H op bend
1125	C-H ip bend
1181	C-H ip bend
1316	arom C-C str
1366	arom C-C str
1512	arom C-C str
1578	arom C-C str
1653	arom C-C str

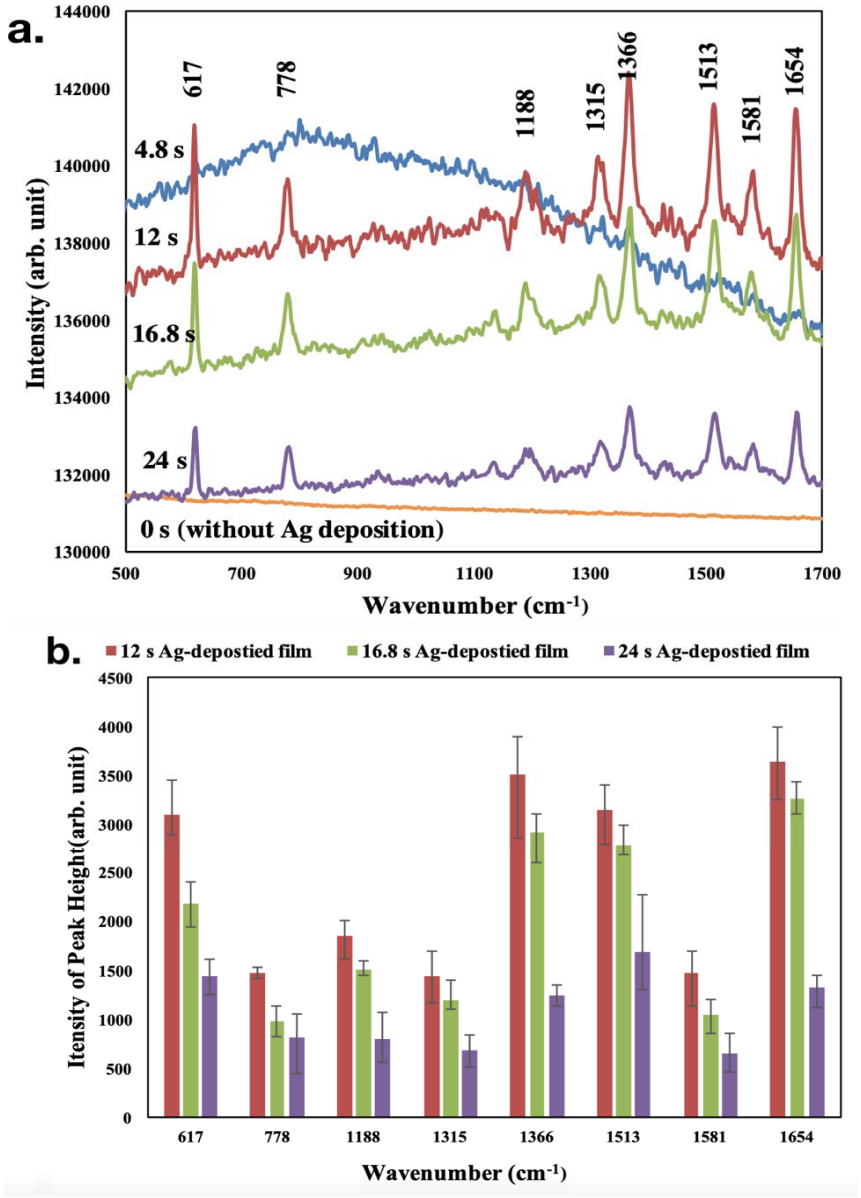
a.
144000
142000
140000
138000
136000
134000
132000
130000
Intensity (arb. unit)
617
778
1188
1315
1366
1513
1581
1654
4.8 s
12 s
16.8 s
24 s
0 s (without Ag deposition)
500
700
900
1100
1300
1500
1700
Wavenumber (cm-1)
b.
12 s Ag-depostied film
16.8 s Ag-depostied film
24 s Ag-depostied film
Itensity of Peak Height(arb. unit)
4500
4000
3500
3000
2500
2000
1500
1000
500
0
617
778
1188
1315
1366
1513
1581
1654
Wavenumber (cm-1)

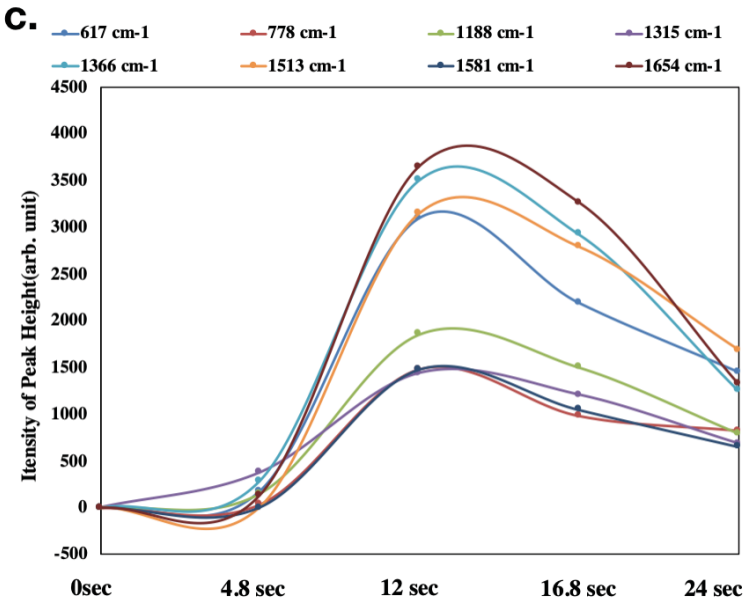

Fig 2.14. (a) SERS signal of 100 μM rhodamine 6G measured at the silver-deposited carbon working electrode on the glass epoxy substrate with different deposition time of 0 s, 4.8 s, 12 s, 16.8 s and 24 s. (b) Signal to noise of SERS spectral of each peak on the silver-deposited carbon working electrode with different deposition time of 12 s, 16.8 s and 24 s. (c) Relationship between deposition time and signal to noise of SERS spectral of each peak. The acquisition time: 60 s and laser power: 0.5 mW.

Fig 2.15a showed the SERS spectra of six types of SERS-active SPEs. Surprisingly, the SERS signals were able to be observed at all kinds of the substrate even at the paper electrode which demonstrated the applicability of the sputtering method for producing SERS-active SPEs. Intensities of peak height were calculated and shown in Fig 2.15b. The result implied that SERS enhancement of R6G on the Ag/Au SPEs was generally stronger than that on the Ag/C SPEs. Besides, the signal

intensity of the SERS-active SPE on the PET substrate was the greatest among all types of the substrate.

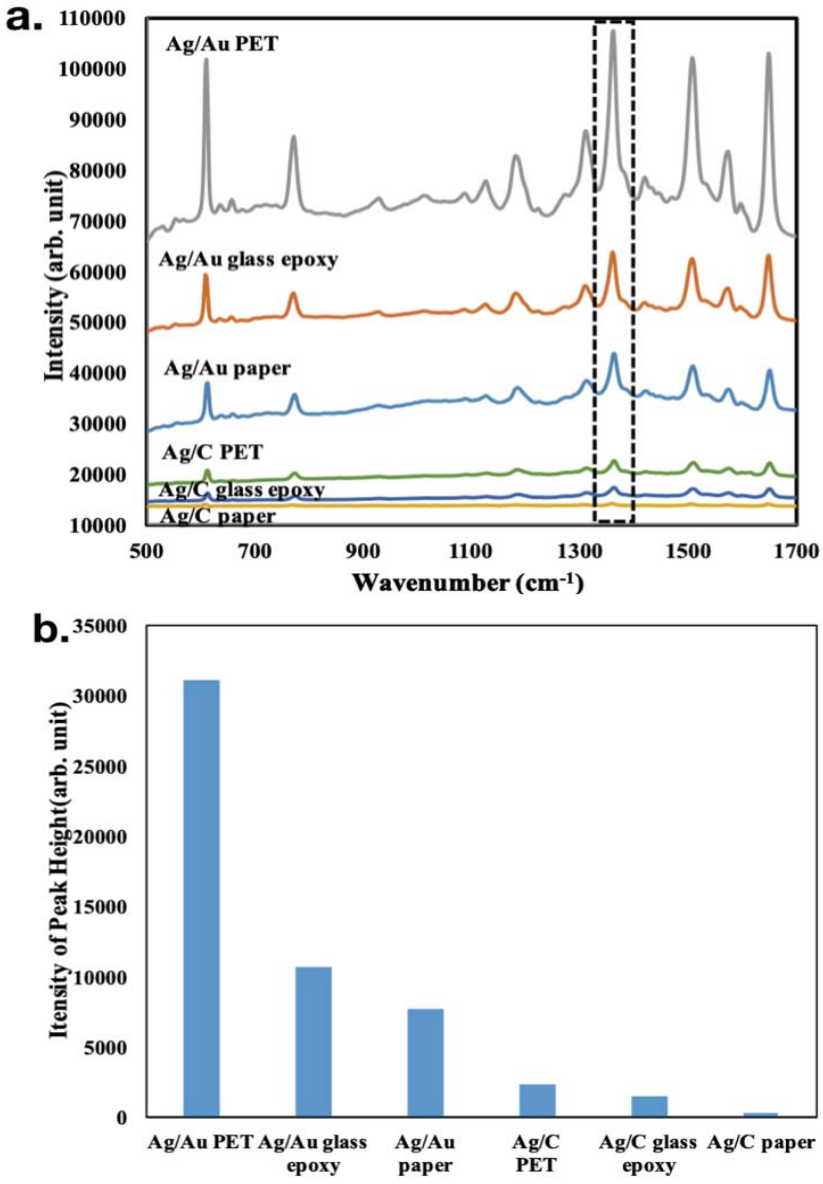

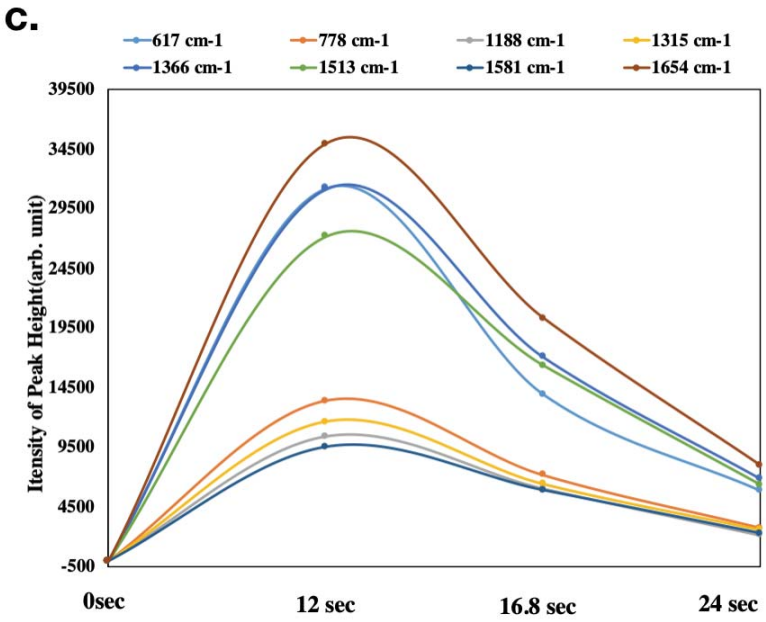

Fig 2.15. a) SERS signal of 100 μM rhodamine 6G measured on the six kinds of SERS-active SPEs which were Ag/Au SPE and Ag/C SPE on the PET substrate, Ag/Au SPE and Ag/C SPE on the glass epoxy substrate, Ag/Au SPE and Ag/C SPE on the paper substrate. b) Signal to noise of peak height at 1366 cm-1 of these six kinds of SERS-active SPEs. (c) Relationship between deposition time and signal to noise of SERS spectral of each peak. The silver deposition time was 12 s. The acquisition time: 60 s and laser power: 0.5 mW.

The enhancement factors of 12 s Ag-deposited SPE was roughly estimated through previous reports based on our experimental results [275]–[278]. The density of R6G is 1.26 g/cm^3 and the maximum surface area per R6G molecule on the surface is estimated to 2.22 nm^2 [275]. The laser excitation volume was 51.8 μm^2 in horizontal area and 1.4 μm in depth. The normal Raman scattering spectra of solid rhodamine 6G were

measured at the same condition as Fig. 2.14 a. The peak of normal Raman intensity at 1366 cm^{-1} was approximately 1/35 of SERS signal at 12 s Ag-deposited SPE. The number of molecules in the sampling volume for normal Raman and for the SERS was estimated to be 1.2×10^{14} and 1.5×10^{10}, respectively. The surface roughness of SPE was ignored in the estimation. The enhancement factor was roughly estimated as 2.8×10^{5}, which was comparable to the result of enhancement factor by using colloidal silver nanoparticles prepared by citrate reduction method in previous reports [278], [279]. Fig 2.16 showed the SERS spectral of SERS-active micro-chamber SPEs. This type of SERS-active SPE will be implemented for the EC-SERS detection of multiple targets. The diameter of each micro-chamber was around 200 µm. SERS signal from micro-chamber P1 to P6 can be observed which is shown in Fig 2.16b.

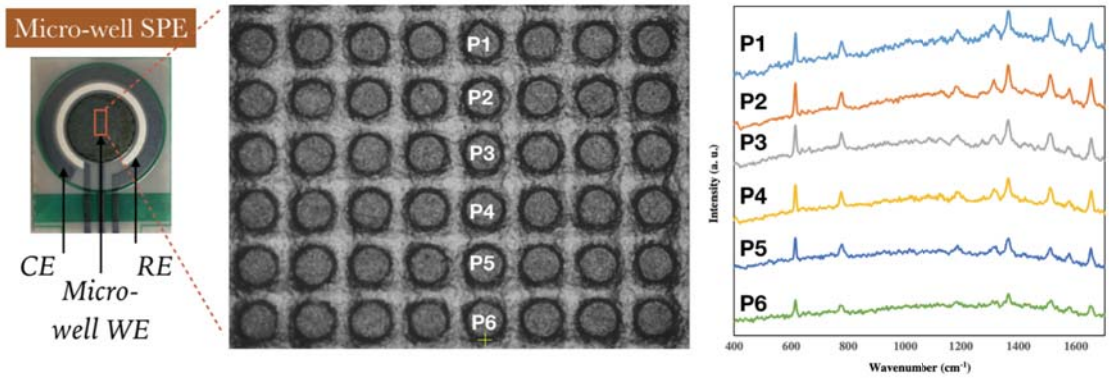

Fig 2.16. SERS signal of 100 µM rhodamine 6G measured on the SERS-active micro-chamber SPEs. The acquisition time: 60 s and laser power: 0.5 mW.

Compared with the citrate reduction method [266][280], the background noise of SERS-active SPEs was much better through the sputtering deposition method which was shown in Fig 2.17. The result was considered that the citrate molecule

absorbed on the surface donated a significant SERS background signal and limited the surface absorption of target analytes through the citrate reduction method [268]. While, through sputtering deposition, it promised low SERS background signal and a maximum of surface absorption for target analytes because there was no other material but pure silver directly deposited on the working electrode.

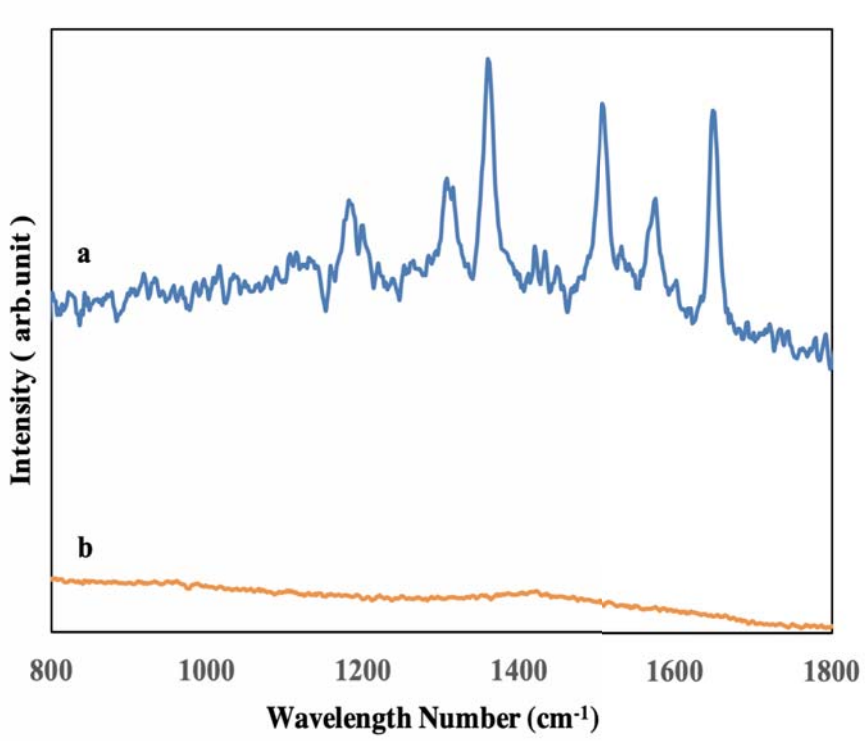

Fig 2.17. a) SERS signals of rhodamine 6G at the 12 s Ag-deposited carbon SPE. b) SERS signals of 12 s Ag-deposited carbon SPE (background signal).

2.5 Conclusion

The fabrications of SERS-active electrodes have been successfully conducted through sputtering deposition. The island structures of silver nanoparticle were observed on both carbon and gold working electrodes through 12 s sputtering

deposition. The deposited film structure was analyzed by ellipsometer which indicated that the actual deposited structure of Ag film was close to those of design. According to the SERS experiments of R6G, the SERS signals of 12 s silver-deposited film were the strongest among those at the other structure of silver-deposited films for both carbon and gold working electrodes. Compared with Ag/C structure, the SERS enhancement of Ag/Au structure was much stronger. The enhancement factors of Ag/C and Ag/Au structure were estimated as 2.8×10^5 and 2.2×10^7, respectively. Among the three kinds of substrates of SPE, SERS signals of R6G were the most enhanced on the PET substrate. Low background noise of SERS signals could be observed on the SERS-active SPE fabricated by sputtering deposition method. It is worth mentioning that thickness errors of continuous 5 batches of silver sputtering coating are ±0.1 nm which shows reliable reproducibility by sputtering deposition. It is reasonable to conclude that sputtering method is exceptionally applicable to the manufacture of SERS-active SPEs. Through this rapid, reproducible and mass producible fabrication method, it is acknowledged as a promising analysis platform.

Chapter 3. Application for Uric acid using EC-SERS

3.1 Introduction

3.1.1 Uric acid

Uric acid is a heterocyclic compound of carbon, nitrogen, oxygen, and hydrogen with the formula $C_5H_4N_4O_3$. Uric acid is a product of the metabolic breakdown of purine nucleotides, and it is a standard component of urine. High blood concentrations of uric acid can lead to gout and are associated with other medical conditions including diabetes and the formation of ammonium acid urate kidney stones. Uric acid is also a primary biomarker in urine for early diagnosis of preeclampsia [281].

3.1.2 Setup of the EC-SERS bio-analyzing system

The SERS and EC-SERS spectral were obtained via an objective 20X lens, and the laser spot size was measured through the microscope images of the Raman-11. The detail information was introduced in Chapter 2. The potentiostat system was a USB portable device named BDTminiSTAT100 which was available for several voltammetric techniques methods such as chronoamperometry (CA), cyclic voltammetry (CV), square wave voltammetry (SWV), differential pulse voltammetry (DPV) and linear sweep voltammetry (LSV). The potentiostat system and SPE were both provided by BioDevice Technology. From Chapter 2, the 12 s silver-deposited

film showed the best enhancement for Raman signals. Therefore, it was used for electrochemical SERS measurements.

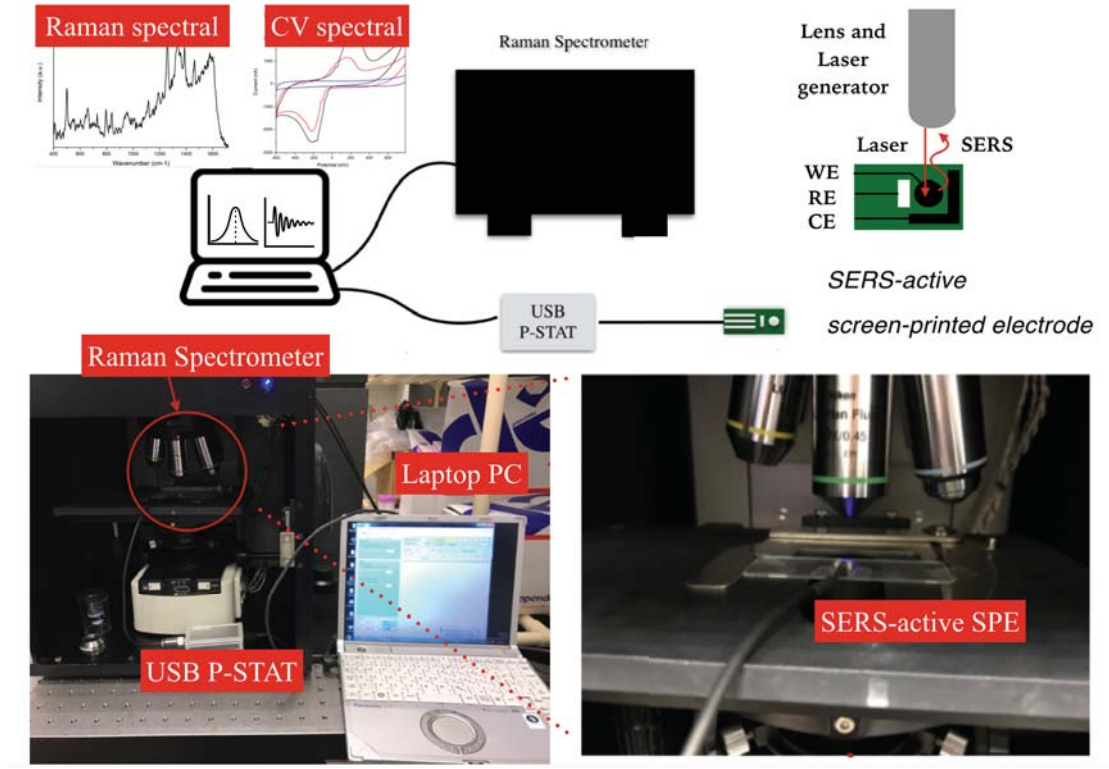

Fig. 3.1 Setup of the EC-SERS bio-analyzing system.

3.2 Experimental preparation

The SERS-active SPEs were prepared by the sputtering method which was reported in our previous chapter. In brief, the SPEs were mounted to a customized mask so that only the areas of the working electrode were exposed for sputtering deposition by an in-line sputtering machine. The silver nanoparticles were deposited onto the working electrode of the screen-printed electrode. The power of silver target was set to 250 kW for the sputtering process. The deposition time of the sputtering process was 12 s.

The Raman spectrometer used for these studies was Raman-11 (Nanophoton, Japan) which equipped with air-cool CCD of 1340 × 400 pixel and 532 nm laser and the potentiostat system was a USB portable device named BDTminiSTAT100 provided by BioDevice Technology which was introduced in Chapter 2. The laser wavelength, the power at sample and acquisition time was 532 nm, 1.4 mV and 60 s, respectively. The SERS and EC-SERS spectral were obtained via an objective 20X lens.

Uric acid was purchased from Wako Pure Chemical Industries, Ltd. For the E-SERS experiment, 100 μM uric acid was added into 0.05 M NaF solution which was as the supporting electrolyte. Besides, high-purity Milli-Q water with a resistivity of ≥18.2 MΩ·cm was used for the experiments.

3.3 EC-SERS analysis of uric acid

3.3.1 Normal Raman of uric acid

Normal Raman spectra of uric acid were shown in Fig 3.2. The peaks of 619 cm^{-1}, 1033 cm^{-1}, 1115 cm^{-1},1500 cm^{-1}, and 1644 cm^{-1} can be obviously observed which represents the assignment of skeletal ring deformation, mixed vibration, ring vibration, C-C stretching and C=O stretching, respectively.

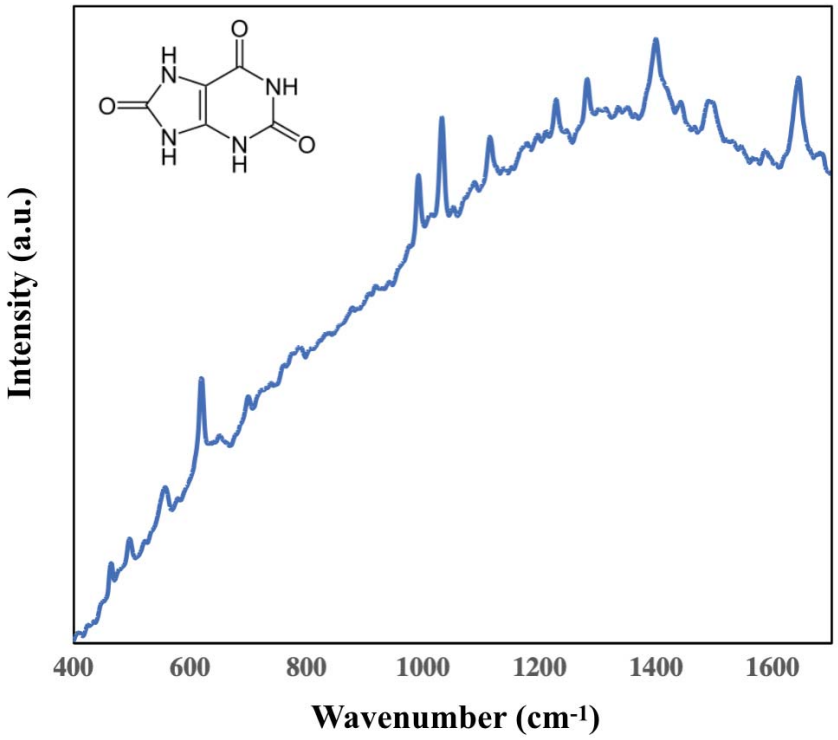

Fig 3.2 Raman spectral of uric acid powder

3.3.2 Density functional theory (DFT) simulation

Theoretical calculations were made by using the Gaussian 09 software. Quantum-chemical calculations were done in order to predict the infrared and Raman frequencies and intensities. Combined with table 3.1, the calculated spectra shown in Fig 3.3 is mostly consistent with the normal Raman spectra for uric acid (powder). The band assignments are also in agreement with other previous researches.

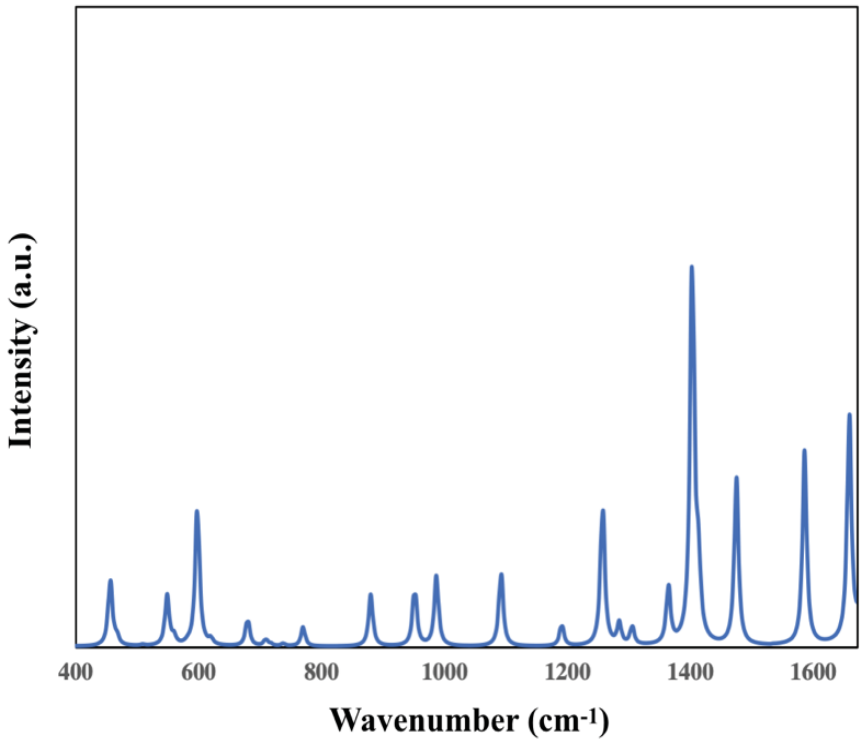

Fig 3.3 Quantum-chemical calculation of uric acid molecule by employing the B3LYP functional, choosing a 6-311 + G basis set.

Table 3.1. DFT simulation, Raman and SERS band assignment of uric acid

Simulation	Raman	SERS	Assignment
457	466	490	C–N–C ring vibrations
549	496	526	CN bending
596	560	-	Ring breathing mode
-	619	632	Skeletal ring deformation
-	-	807	Ring vibrations
879	-	881	N-H bending
953	-	-	-
986	993	1013	Ring vibrations
-	1033	-	Mixed vibrations: ring
1092	1115	1133	vibrations, C–O, C–C, C–N, and N–C–C
-	1229	1202	CN stretching, OH bending
1258	1282	-	CN stretching
-	-	1352	-
1405	1400	-	-
1475	1500	-	CC stretching
1585	-	1577	CN stretching
1658	1644	-	C=O stretching

3.3.3 EC-SERS analysis

The EC-SERS spectral of 100 μM uric acid in aqueous solution were recorded by collecting the spectrum at open circuit potential at first, and then stepping the applied voltage in the negative direction from 0 mV to -2000 mV in 200 mV increment.

3.4 Results and discussion

The assignment of SERS bands for uric acid is displayed in Table 3.1. It could be observed that the intensity signal was gradually enhanced with more negative applied potential until the applied potential reached -1400 mV. The peak intensities of strongly enhanced wavenumbers were calculated and shown in Fig 3.4 which were 632cm^{-1}, 807cm^{-1}, 881cm^{-1}, 1133cm^{-1} and 1202 cm^{-1} corresponding to the skeletal ring deformation, ring vibration, N–H bending, C–O, C–C, C–N, and N–C–C stretching and bending (Table 3.1). This phenomenon suggested that the uric acid molecule adopted vertical mode and kept a distance from the surface [196]. When the potential was applied up to -1600 mV, intensities of SERS bands were all weaken, which suggesting that the detachment of the uric acid molecules from the surface occurred. Finally, all bands could be hardly observed as the potential reaching -2000 mV. It suggested that the uric acid molecules were away from the substrate because of the negative charge density of uric acid molecule.

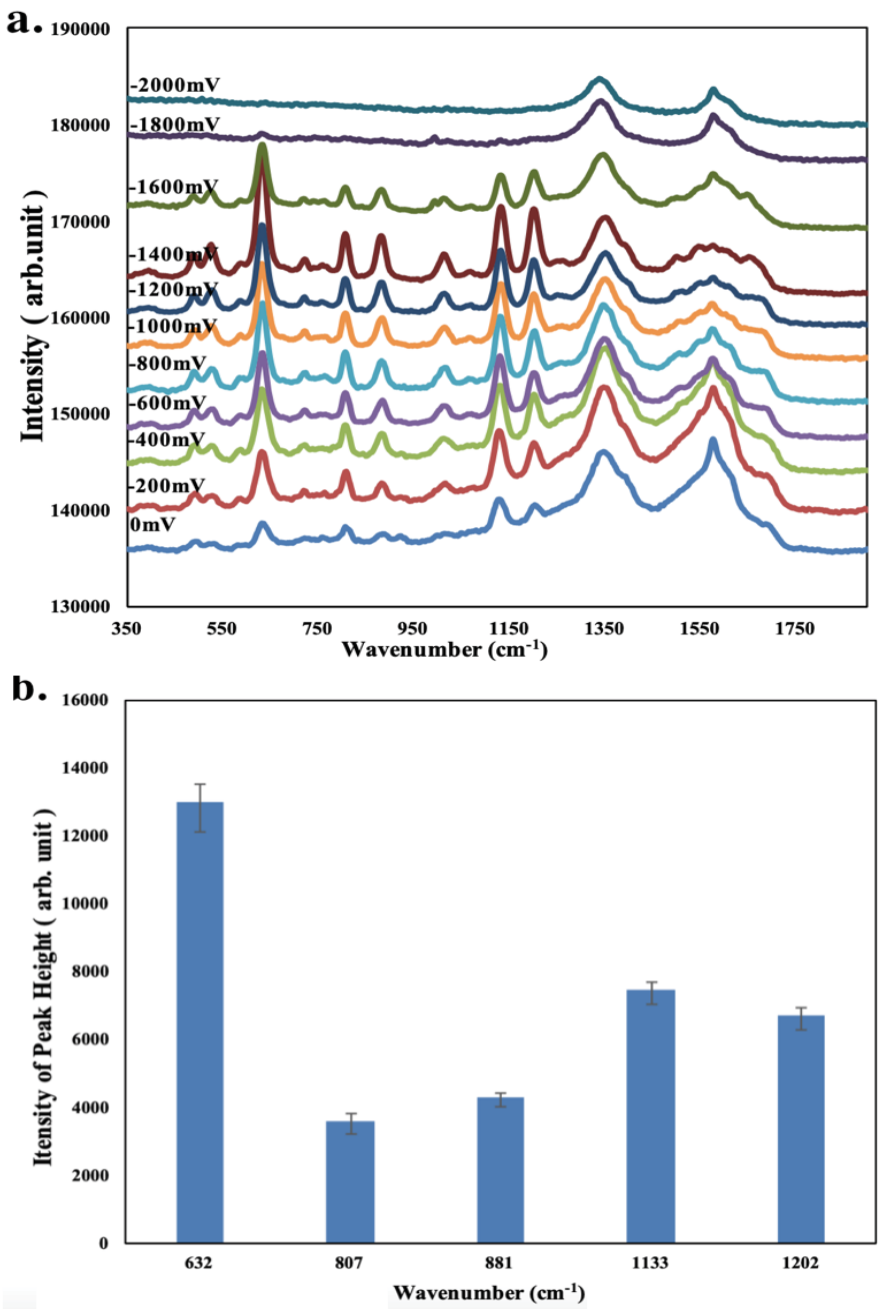
a.
Intensity (arb.unit)
190000
180000
170000
160000
150000
140000
130000
-2000mV
-1800mV
-1600mV
-1400mV
-1200mV
-1000mV
-800mV
-600mV
-400mV
-200mV
0mV
350
550
750
950
1150
1350
1550
1750
Wavenumber (cm-1)
b.
Itensity of Peak Height (arb. unit)
16000
14000
12000
10000
8000
6000
4000
2000
0
632
807
881
1133
1202
Wavenumber (cm-1)

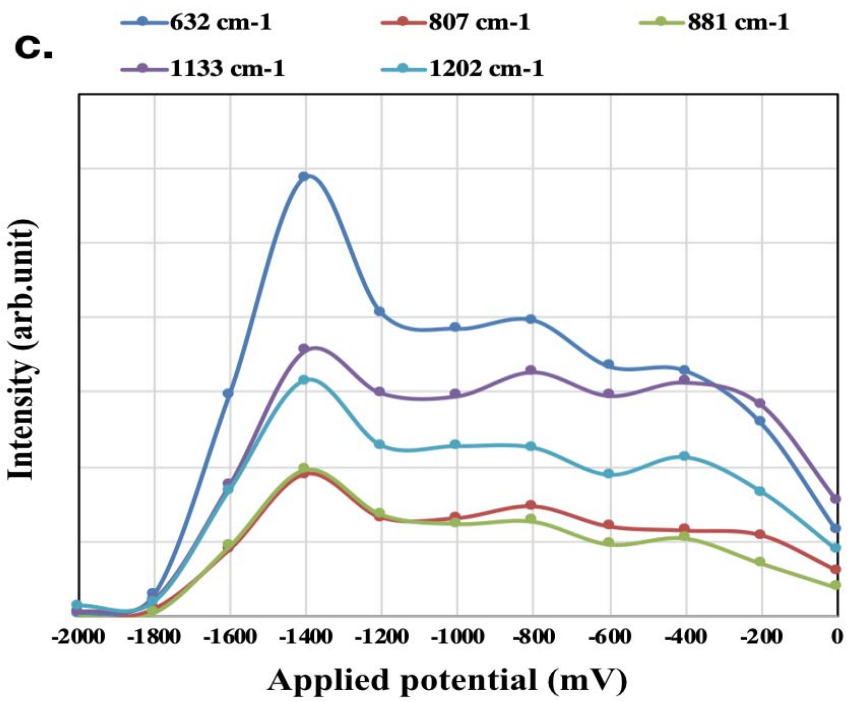

Fig. 3.4 (a) SERS spectral of 100 μM uric acid in aqueous solution with different potentials at the 12 s silver deposited carbon electrode on the PET substrate. The potentials were stepped in 200 mV increment from 0 mV to -2000 mV vs Ag/AgCl. Acquisition time: 60 s, laser power: 1.4 mW; (b) The peak intensities of SERS spectral of uric acid at the wavenumber of 632 cm^{-1}, 807 cm^{-1}, 881 cm^{-1}, 1133 cm^{-1} and 1202 cm^{-1} when applied potential was -1400 mV. (c) The relationship between the SERS intensity and applied potential. The acquisition time: 60 s and laser power: 0.5 mW.

Moreover, the potential-dependent behavior of uric acid absorbed on a SERS-active surface is in line with the charge transfer mechanism [282], [283]. Different applied potentials allowed alterations of the Fermi level of the metal. In this case, when the applied potential was less negative than -1400 mV, it was insufficient to produce the photon-driven CT state on the surface with excitation energy [273]. The bonding

effect caused the change of relative SERS intensity [284], [285]. When the potential was around -1400 mV, a significant enhancement in SERS intensity could be observed. It implied that the excitation energy fitted with the required CT energy due to the increase of the Fermi level. When the potential was more negative than -1400 mV, the SERS signal decreased because the excitation energy did not fall into an ideal resonance condition. Fig 3.4 c shows the relationship between signal intensity and applied potentials. The potential of -1400 mV shows the most enhanced SERS signal at the peak of the curve which is consistent with the mechanism of charge transfer. As shown in Fig 3.6, the limited of detection of uric acid reached 10 μM by EC-SERS measurement which was 10 times more sensitive than that of previous work [274]. Cyclic voltammetry (CV) data was shown in Fig 3.5. It was interesting that the redox peaks around -1400 mV in CV data were corresponding to the most enhanced EC-SERS signal. This result was agreed with the work done by Goodall et al. [274].

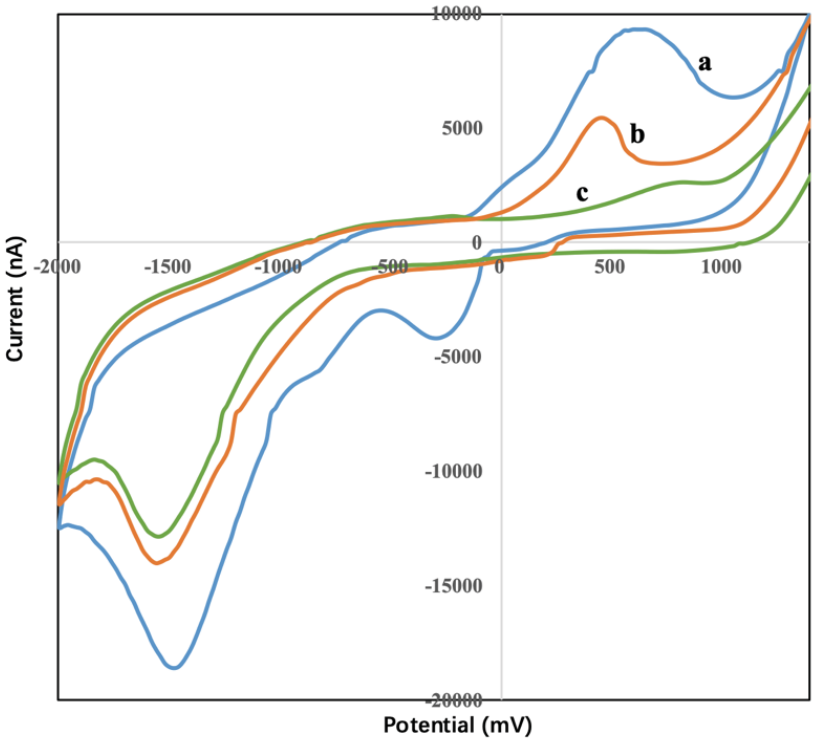

Fig 3.5 CV data of a) uric acid in 0.05M NaF solution on 12 sec deposited silver carbon SPE, b) uric acid in 0.05M NaF solution on carbon SPE and c) 0.05M NaF solution on carbon SPE. (-1400mV dissovled oxygen)

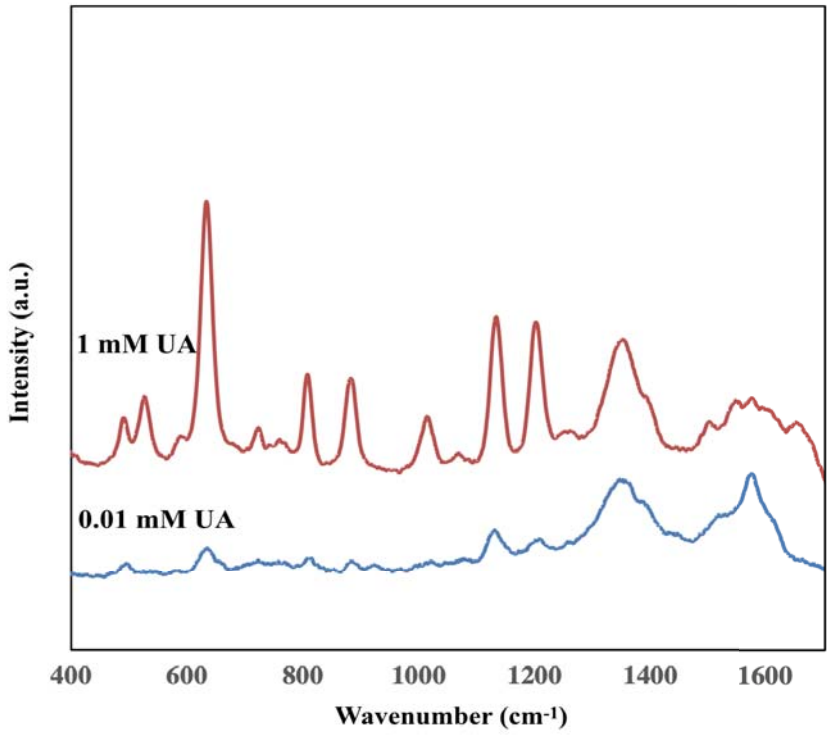

Fig. 3.6 SERS spectral of 1 mM and 10 μM uric acid in aqueous solution with potentials of -1400 mV vs Ag/AgCl. at the 12 s silver deposited carbon electrode on the PET substrate. Acquisition time: 60 s, laser power: 1.4 mW.

3.5 Conclusion

The spectroelectrochemical investigation of uric acid indicated that applying a proper negative potential on the electrode led to a significant effect on SERS signals enhancements. Besides, limited of detection is 10 times better than previous EC-SERS work which is considered as the benefit from the sputtering fabrication method.

Chapter 4. EC-SERS Application for Aminoglutethimide

4.1 Introduction

Aminoglutethimide (AGI) is an aromatase inhibitor which is used clinically for the treatment of hormone-dependent metastatic breast cancer [286]. For non-medical use, it is abused by bodybuilders and other steroid users to minimize the levels of circulating cortisol in the body and to prevent muscle loss. Also, the consumption of AGI by athletes in official competitions is banned by the World Anti-Doping Agency [287]. With the growing global concern for drug abuse problems, alternative methods for chemical identification that is efficient, easy-to-use, with simple instrumentation, but still having excellent accuracy and high sensitivity are much desired.

Several approaches, for quantitatively detecting AGI, have been reported to control its illegal use such as UV-VIS spectrophotometry, chromatography mass spectrometry (LC-MS), capillary electrophoresis (CE) and surface-enhanced Raman spectroscopy (SERS). UV-VIS spectrophotometry, LC-MS and CE require pre-treatment and have low detection sensitivities (10 μg/mL, 100 μg/mL and 20 μg/mL, respectively) [85], [88], [286]–[291]. SERS has gained much attention since 2010 because of the combination of detailed structural information of the analyte with trace level sensitivity down to a single molecule level with minimal sample preparation. However, certain chemicals have weak SERS signal and thus modulation is needed.

SERS coupled with electrochemistry can be used to modulate the detected signal of the analyte present on the metal surface at a chosen applied voltage. Compared with

normal SERS, the electrochemical SERS (EC-SERS) technology provides enhanced SERS signal and more 'fingerprint' information of the molecular bonds and molecule-surface bonds [208], [292]. Benefiting from the adjustable potentials on the electrode, the orientation of the molecules on the substrate can be altered which affects the intensity of the SERS signal. Both chemical and physical enhancements of SERS can be influenced to a certain extent by applying an electrode potential. Also, the electrochemical SERS sensor can be useful for detecting the signal of the analyte in a biologically relevant environment, for observing how a molecular conformation and orientation changes at different applied voltages, and also for measuring the electrochemical stability of specific analytes.

In this chapter, EC-SERS as a satisfying method for the rapid and quantitative detection of AGI is investigated. By several selected applied potentials, different adsorption mode of AGI molecule interacting with the SERS-active substrate can be observed, such as monodentate interaction through aniline or glutarimide moiety and bidentate interaction through both moieties. Compared with the SERS technique, these adsorption modes offer the advantages of enhanced signal intensity and more selectivity of the AGI molecule. The EC-SERS sensor may become a useful tool for rapid and routine analysis in anti-doping detection and patient biomarkers for on-site use.

4.2 Experimental Preparation

The potentiostat system and the preparation of SERS-active SPEs were the same as those in Chapter 3.

The Raman spectra and Raman images were obtained with a laser Raman confocal microscope (RAMAN-11, Nanophoton, Japan) equipped with a Nikon 100X, NA = 0.9 objective lens and an Olympus 20X, NA = 1.0, water-immersion objective lens, which were used for measuring the Raman spectral of AGI power and E-SERS spectral of AGI in solution, respectively. The sample was illuminated with a line-shaped laser (532 nm) was about 2.8 mW / line (400 pixels) focused through the objective lens. Raman scattering from the samples was collected by the same objective lens and guided to a spectrophotometer with a slit width of 15 μm. The Raman signal was diffracted by a 600 grooves/mm grating (spectra resolution, 1.6 cm^{-1}) and detected by an air-cooled CCD camera (-70 ˚C). Raman spectra were obtained from 1.25 μm x 167 μm (3 x 400 pixels) area.

The AGI, sodium fluoride, and ethanol were purchased from Wako Pure Chemical Industries, Ltd. A stock solution of AGI in ethanol at a concentration of 0.1 M was prepared, and further dilutions were made under ethanol or Milli-Q water. Absolute ethanol is of analytical grade (99.5% purity) and high-purity Milli-Q water has a resistivity of ≥18.2 MΩ·cm. For all EC-SERS measurements, 0.05 M NaF solution was used as the supporting electrolyte and the volume of the solution was 30 μL. The pH value of the buffer solution was 6.0.

Atomic force microscope (SPA400-AFM, Seiko Instruments Inc., Japan) was used for analyzing the surface of the SERS-active SPE which was equipped with a calibrated 20 μm xy-scan and 10 μm z-scan range PZT-scanner. All AFM images were taken in

dynamic force mode (DFM mode, i.e., tapping mode) at optimal force. A silicon cantilever (OMCL- AC160TS, OLYMPUS), which has a spring constant of 42 N/ m and a frequency resonance of 300 kHz, is also used for imaging in the air at room temperature.

Theoretical calculations were made by using the Gaussian 09 software. Geometry optimization is refined by employing the B3LYP functional, choosing a 6-311 + G basis set. The Hessian was evaluated at the first geometry (opt = CalcFC) for the first level in a series in order to aid geometry convergence.

4.3 Results and discussion

4.3.1 Normal Raman of AGI

Raman spectroscopy was used to characterize the solid AGI powder as shown in Fig 4.1a. Analysis of the spectra shows the bands of C-C-C oop bending, C-H ip bending / NH_2 rocking, C-NH stretching and C-H ip bending at 541, 1071, 1182 and 1200 cm^{-1}, respectively, suggesting that the aniline moiety exists in the powder form of AGI. Meanwhile, the spectra show the bands of C-C aromatic oop, CH_2 rocking, C-C-N bending / CH_2, and C-H ip bending / C-NH_2 at 649, 720, 834 and 1216 cm^{-1}, separately, implying that the powder form of AGI contains glutarimide moiety. Normal Raman spectroscopy exhibits poor sensitivity for the detection of analytes at low concentration.

Table 4.1 DFT simulation, Raman and SERS band assignment of AGI

Assignment	Simulation	Raman	SERS	E-SERS with -200mV	E-SERS with -400mV	E-SERS with -600mV	AGI Group
C-O bending			535w				
C-C-C oop bending		541w	545w	566w	556w		AN
Ring ip bending	598m	602w	602w	609w	613w	607m	
N−C=O bending	624w						GI
CNC aromatic bending		638m	640w				AN
C-C aromatic oop bending		649m					GI
CNC aromatic bending	658w		657m				AN
CH_2 rocking	737w	720w	728m				GI
	764w	755w	759w			753m	
		793m	795m				
C-C-N bending / CH_2 rocking	802s	834s	840m				GI
C-H aromatic oop bending	889w	881m	891w		891w		
C-N-C bending / CH_3 rocking	956m	952w	954m			948m	Ag-GI
	987w	985w	985w		994w	972m	
		1003w	1009w				GI
			1027w	1037w			
C-C stretching/	1060m	1045w	1053w				
C-H ip bending / NH_2 rocking	1088w	1071m	1071w		1089m		AN
NH_3^+ rocking		1113w	1115m				
		1129w		1131w			
C-H ip bending / CH_2 twisting		1145m	1151w		1147s		AN/GI
	1156m	1160w	1166w				
C-NH stretching	1187w	1182w	1188m	1182w	1182m		AN
C-H ip bending	1206w	1200w	1222w	1227w		1227m	AN
C-H ip bending / C-NH_2 aromatic stretching		1216m					GI
CH2 twisting			1259s	1245w			GI
CH_2 wagging	1293m	1294m	1288w	1303m	1302s	1313s	Ag-GI
C-NH_2 aromatic stretching	1322w		1331s				Ag-GI
CH_3 bending			1387w	1375m			GI
CH_2 bending		1404w		1400w	1410m		GI
CH_2 bending		1437m					GI
CH_2 bending	1459w	1448m	1461w	1463w	1442m	1477w	GI
C=N stretching / C=O stretching				1501w	1500m	1505w	Ag-GI
NH bending	1516w	1513w		1528w			GI
NH_3^+ rocking				1575s	1566m		AN
C-C stretching		1605s			1596w	1607m	AN
C-C stretching	1616s	1622s					AN
C-O asymmetric stretching	1665s	1682m					GI
C-O stretching		1704s					GI

In order to detect these analytes, surface-enhanced Raman spectroscopy (SERS) was employed. The morphology of the silver island-structured film on the SPE is recognized as the critical element of the SERS-based sensor. The nanostructured silver surface is widely used for SERS technique which associates with the enhancement of the electromagnetic field surrounding small objects optically excited near an intense and sharp plasmon resonance [293]–[300]. The Raman signal is enhanced through the localized surface plasmon resonance (LSPR) and chemical enhancement. The adsorption of AGI on the different metallic NPs employed can be carefully studied by analyzing the resulting SERS spectra. However, the measurement of a SERS signal from AGI requires the adsorbate to approach the metal surface in order to benefit from the electromagnetic near-field enhancement. This involves several processes: (a) diffusion to the surface, (b) adsorption, which usually also implies the removal of other chemical species adsorbed onto the surface, and (c) self-assembly on the interface. The adsorption is a crucial step since aqueous substrates impede the chemical interaction with the surface, making the existence of chemical groups showing some affinity toward the metal necessary.

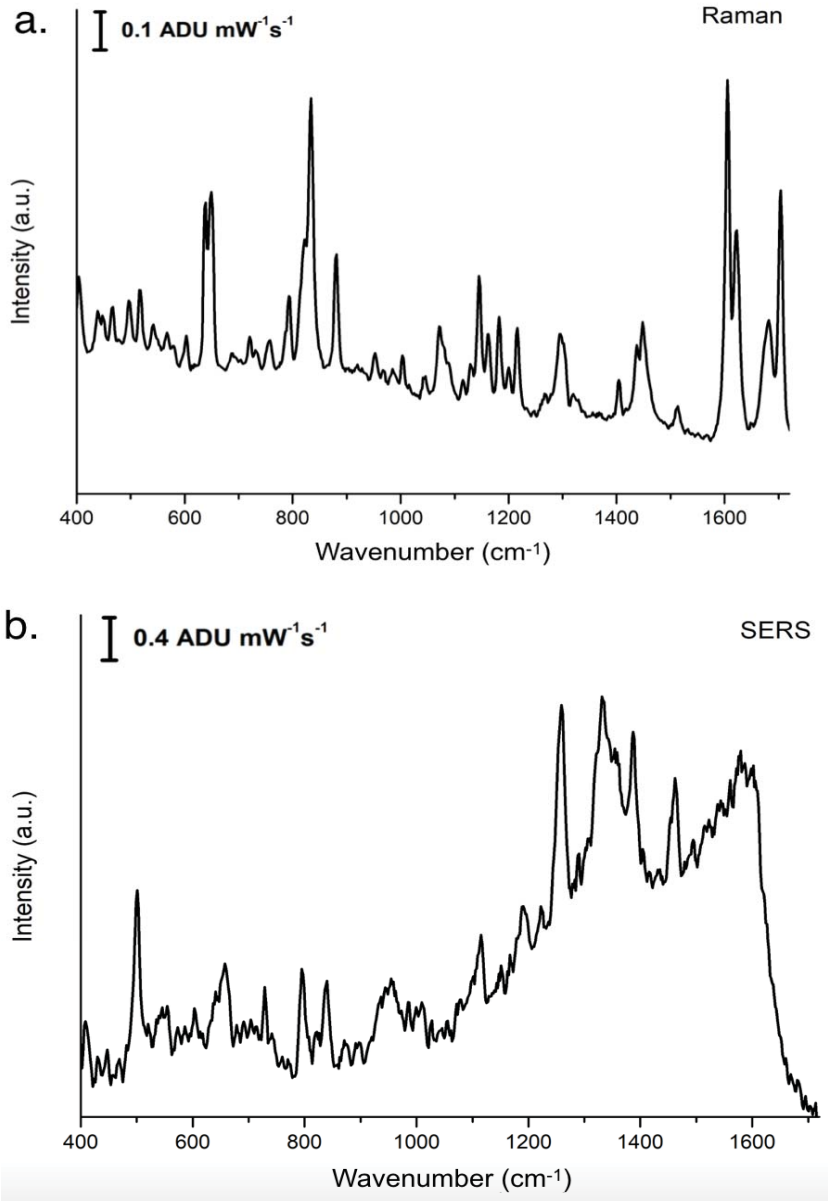

Fig 4.1 (a) Raman spectral of the AGI powder and (b) SERS signal of 0.1 mM AGI in ethanol solution without applied potential. The acquisition time is 60 s and laser powers are 0.5 mW and 2.8 mW, respectively.

AGI has two possible binding sites: aniline (AN) or glutarimide (GI), which determine the interaction mechanism with the metal surface shown in Fig 4.2. Fig 4.2a shows the interaction between AN moiety and silver nanoparticles. The NH_3^+ rocking

vibration from AN moiety is supposed to be enhanced under this type of adsorption mode. Also, the SERS signals of N-H-N bending and CH_2 wagging will increase at the adsorption mode from NH of GI moiety to the silver surface shown in Fig 4.2b. Fig 4.2c suggests the bidentate adsorption of AGI through both the AN and GI binding sites. The SERS signals are predicted to be strongly enhancement through this adsorption mode.

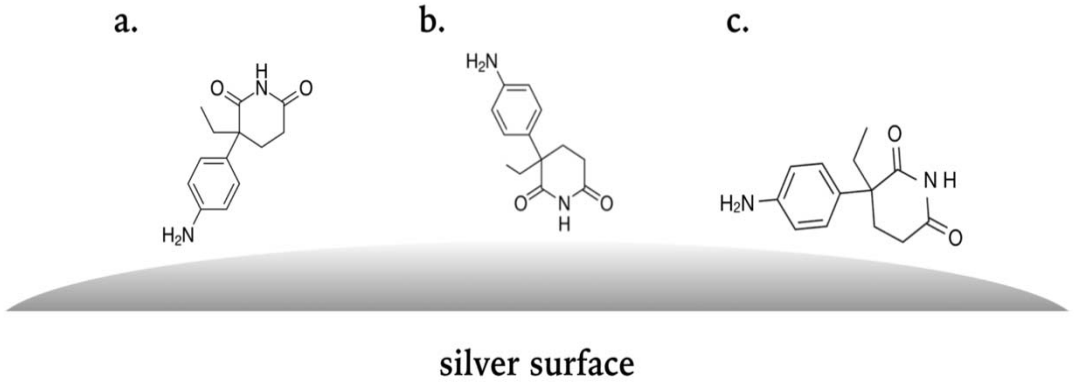

Fig 4.2 Different absorption methods which are a) aniline (AN) b) glutarimide (GI) and c) both aniline and glutarimide moieties interacting with the silver surface

In the present case, the SERS-active substrate is a modified screen-printed electrode (SPE), as described in our previous work. The comparison of SERS spectra in Fig 4.1b with the Raman spectrum of the power reveals an evident weakening or disappearance of the C=O stretching band 1704 cm^{-1} (see Table 1 for assignment), thus indicating that the interaction with the metal through the imide group is taking place. The enhancement and appearance of CH_2 wagging and C-NH_2 aromatic can be observed which correspond to the wavenumber 1288 and 1331 cm^{-1}, respectively,

manifesting a possible implication of GI moiety in the interaction with silver nanoparticles on the SERS-active SPE.

4.3.2 Cyclic voltammetry

To investigate the surface interaction, cyclic voltammetry (CV) was performed. The CV is a powerful tool for electrochemical study which reveals the electrochemical properties of an analyte in solution or of a molecule that is adsorbed onto the electrode. Fig 4.3 shows the CV graphs obtained from the buffer solution on the bare electrode (blue curve), buffer solution on the silver sputtered electrode (red curve) and AGI solution on the silver sputtered electrode (black curve). Compared with the two latter CV data, it is apparent that the current significantly increases for the AGI solution on the SER-active electrode. Moreover, the oxidation and reduction peaks can be observed which are at the potentials of 200 mV and -160mV marked as the star (∗) and solid circle (●), respectively. It suggests that these two peaks are associated with the protonation of the amino group placed in the aniline ring. It suggests that the interaction mechanism of AGI with the substrate seems to take place through the aniline protonated NH_3^+ as following equation:

$$NH_2 + H^+ \rightarrow NH_3^+ \quad (15)$$

While Ag and NH_3 (ammonia) are considered to donate for the oxidation peak around 200 mV as expressed in the following chemical equations:

$$Ag_2O + 4NH_3^+H_2O \rightarrow 2[Ag(NH_3)_2] + 2OH^- \quad (16)$$

$$[Ag(NH_3)_2]^+ + e^- \rightarrow Ag + 2NH_3 \quad (17)$$

Therefore, the adsorption of AGI undergoes a definite change on the substrate depending on the applied potential. This change is modulated by the protonation state of both the amino group of aniline and the imide, which further determines its interaction mechanism on the surface.

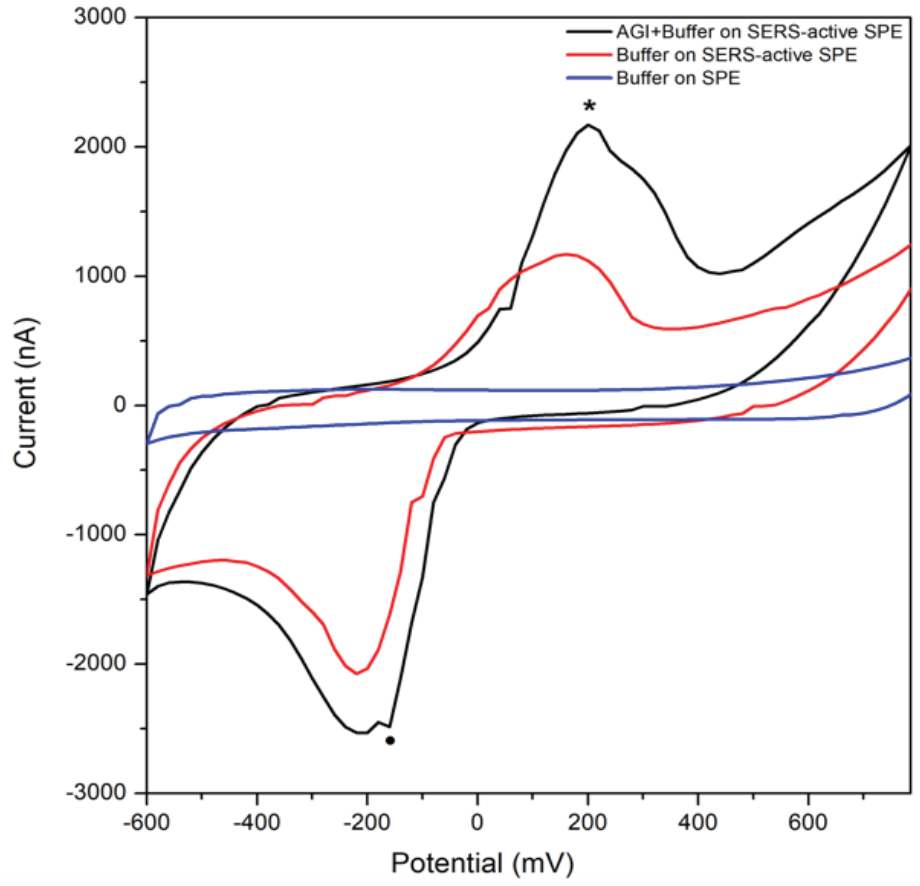

Fig 4.3 Cyclic voltammogram of a bare electrode in buffer solution (blue line), a bare SERS-active electrode in buffer solution (red line), and a SERS-active electrode containing the AGI in buffer solution (black line). Scan rate: 50 mV s^{-1}

4.3.3 EC-SERS analysis

As shown in Fig. 4.4, the EC-SERS spectral of 0.1 mM AGI in the buffer solution is recorded by collecting the spectrum at 0 mV, at first, and then stepping the applied

voltage in the negative direction from 0 mV to -1000 mV in -200 mV increment. The assignments of SERS bands for AGI are displayed in Table 4.1. At the applied potential of -200 mV, the intensity signal of EC-SERS spectrum appearing at 1575 cm^{-1} increased, compared with the normal SERS spectrum. These bands can be assigned to NH_3^+ rocking, which can be attributed to the anilinic part of AGI (see Table 1). This phenomenon suggests that the amino group placed in the anilinic ring is protonated and may interact with the surface by electrostatic interaction, forming an ionic pair with the anionic species already adsorbed on the metal surface [301]. This is also demonstrated by the CV data presented. When the applied potential increases to -400 mV, EC-SERS spectrum is dominated by the intense bands appearing at 1147, 1302 and 1566 cm^{-1}, which can be assigned to C-H / CH_2 bending (1147 cm^{-1}), CH_2 wagging (1302 cm^{-1}) and NH_3^+ rocking (1566 cm^{-1}). These bands can be attributed to both the aniline and glutarimide parts of AGI. The adsorption seems to take place through a simultaneous interaction with both AN and GI moieties. This result suggests that bidentate adsorption of AGI through both the AN and GI binding sites seems to occur at the applied potential of -400 mV. When applied potential reaches -600 mV, the SERS peak of NH_3^+ rocking (1566 cm^{-1}) attributed to the AN part disappears. By contrast, stronger GI bands are examined at the wavenumber of 948 and 1313 cm^{-1} corresponding to C-N-C / CH_3 bending and CH_2 wagging, respectively. It indicates that the interaction mode between adsorbates and substrate turns from the bidentate to the monodentate interaction again.

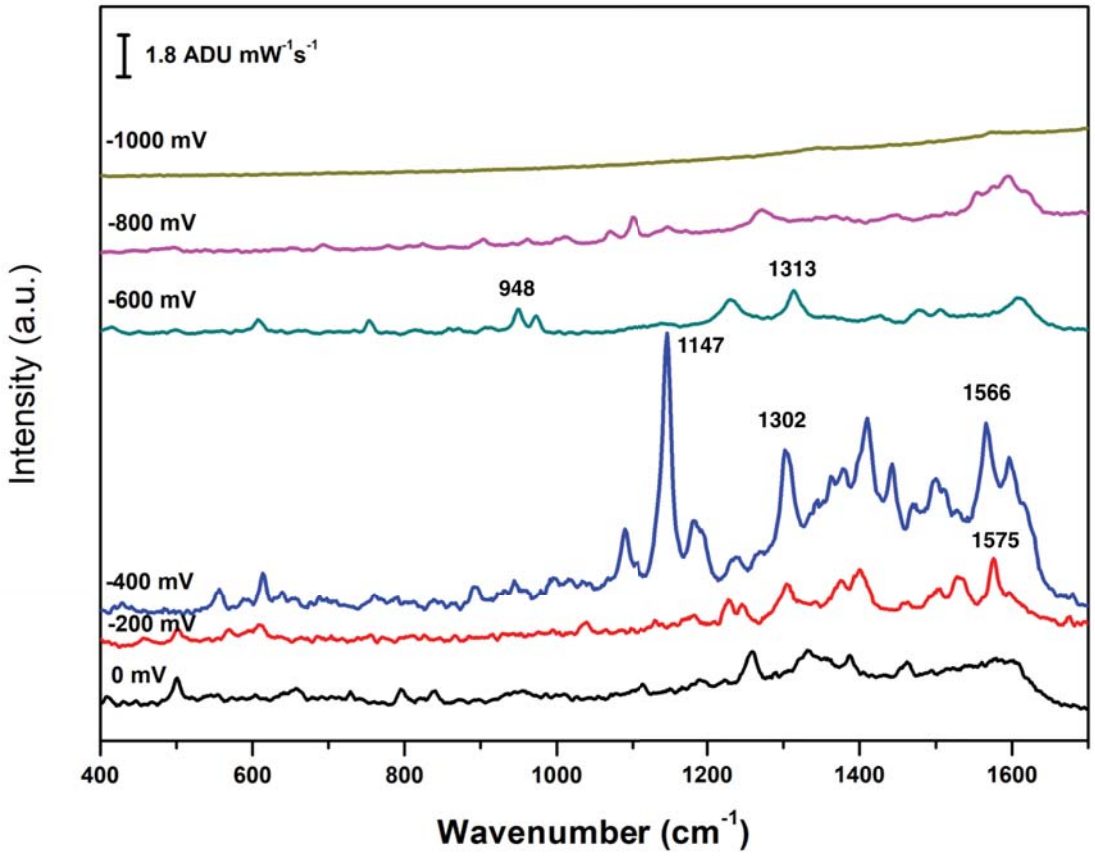

Fig. 4.4 SERS spectral of 0.1 mM AGI in buffer solution with different potentials at the SERS-active electrode. The assignments marked in the graph: C-N-C / CH_3 bending (948 cm^{-1}), C-H / CH_2 bending (1147 cm^{-1}), CH_2 wagging (1313 cm^{-1}) and NH_3^+ rocking (1566 cm^{-1}). The potentials are ramped at -200 mV increment from 0 mV to -1000 mV vs Ag/AgCl. Acquisition time: 60 s, laser power: 2.8 mW.

Moreover, the charge distribution of the amino group in aniline moiety is more negative than that of imino group in glutarimide moiety according to the simulation results shown in Fig 4.5. It explains why the signal from glutarimide moiety is observed to increase as the applied voltage is made more negative. Fig. 4.6 shows the proposed

orientations of the AGI molecule on the AgNPs electrode surface at different applied potentials, which are based on interpretation of EC-SERS spectral data.

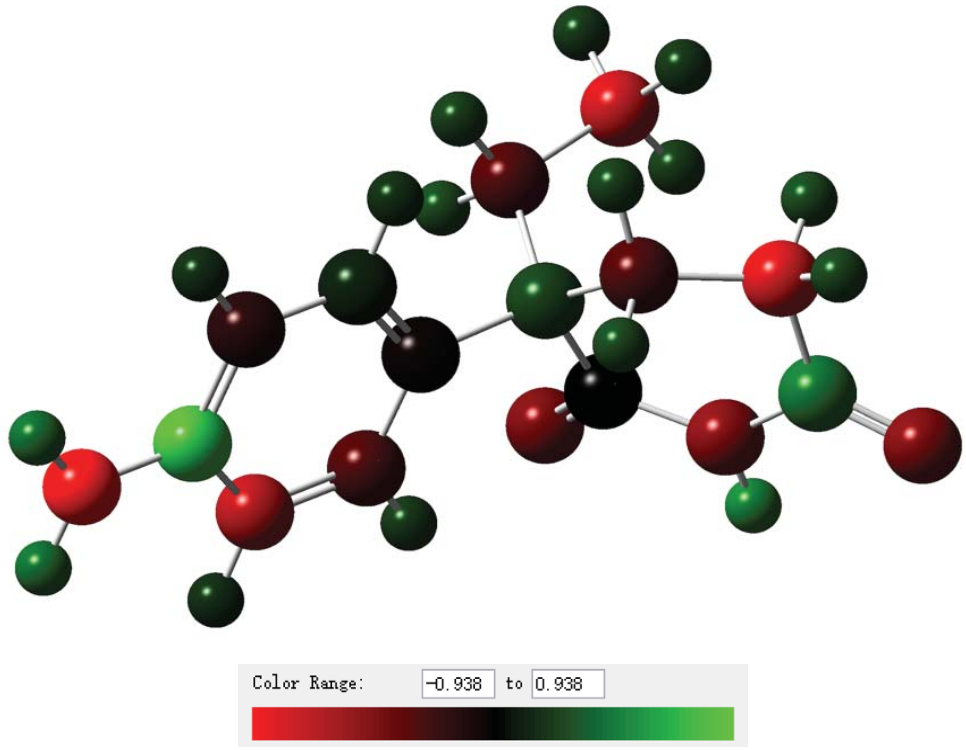

Fig. 4.5 The structure of the AGI molecule in stick-ball mode with the charge density shown in color calculated by B3LYP/6-311 + G.

Besides the potential-induced reorientation, the enhancement of signal intensity may suggest a possible potential-dependent behavior of the AGI molecule at the electrode surface. As the potential is made progressively more negative to -400 mV, some peaks of observed SERS signal increases have increased by over an order of magnitude. Further applied a more negative potential, the observed SERS signal turns into a decrease. This potential-dependent behavior of AGI absorbed on a SERS-active surface is in line with the charge transfer mechanism [201], [282], [302]–[304].

Different applied potentials allowed alterations of the Fermi level of the metal. In this case, when the applied potential was less negative than -400 mV, it was insufficient to produce the photon-driven CT state on the surface with excitation energy. The bonding effect caused the change of relative SERS intensity. When the potential was around -400 mV, a significant enhancement in SERS intensity could be observed. It implied that the excitation energy fitted with the required CT energy due to the increase of the Fermi level. When the potential was more negative than -400 mV, the SERS signal decreased because the excitation energy did not fall into an ideal resonance condition.

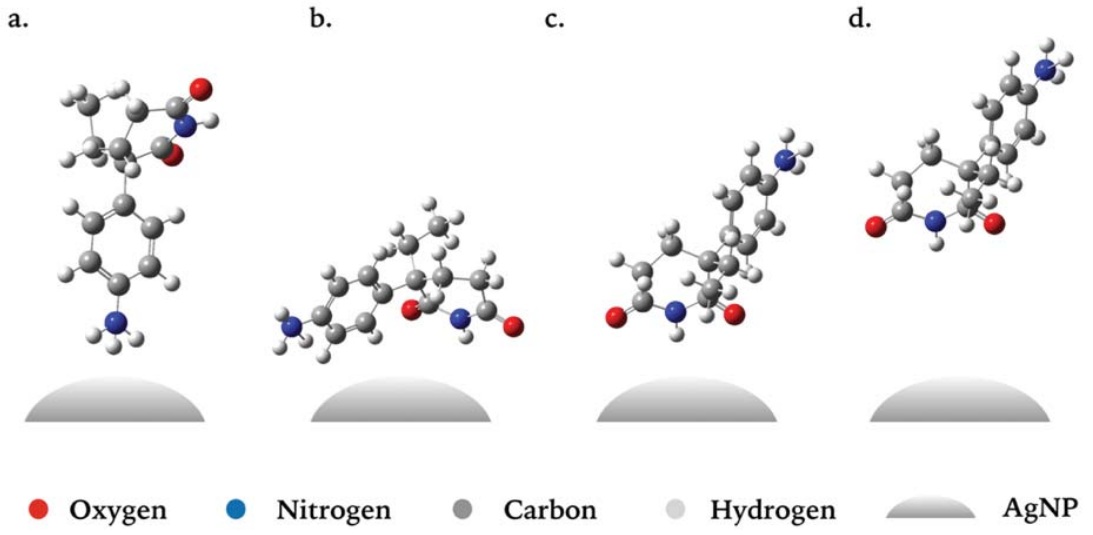

Fig. 4.6 Proposed orientation of the AGI molecule on the AgNPs electrode surface, based on interpretation of spectral data. The applied potentials: at (a) −200 mV, (b) −400 mV, (c) -600 mV and (d) from -800 to -1000 mV vs. Ag/AgCl.

4.3.4 Sensitivity and reproducibility of detection

A low background signal (Fig 4.7b) has been observed from the fabricated electrode and a high signal-to-noise ratio can be expected. Also, this study shows how

powerful EC-SERS can be for the detection of analytes, as compared with nonelectrochemical SERS, it provides the opportunity to drive the analyte to the surface through electric field and surface charge manipulation. Besides, bidentate interaction of AGI on the surface results in much improved SERS signal at applied negative voltages, as evidenced in Fig 4.6. The use of the EC-SERS can come into being the effect of increasing the SERS intensity of the target analyte by approximately 2 orders of magnitude.

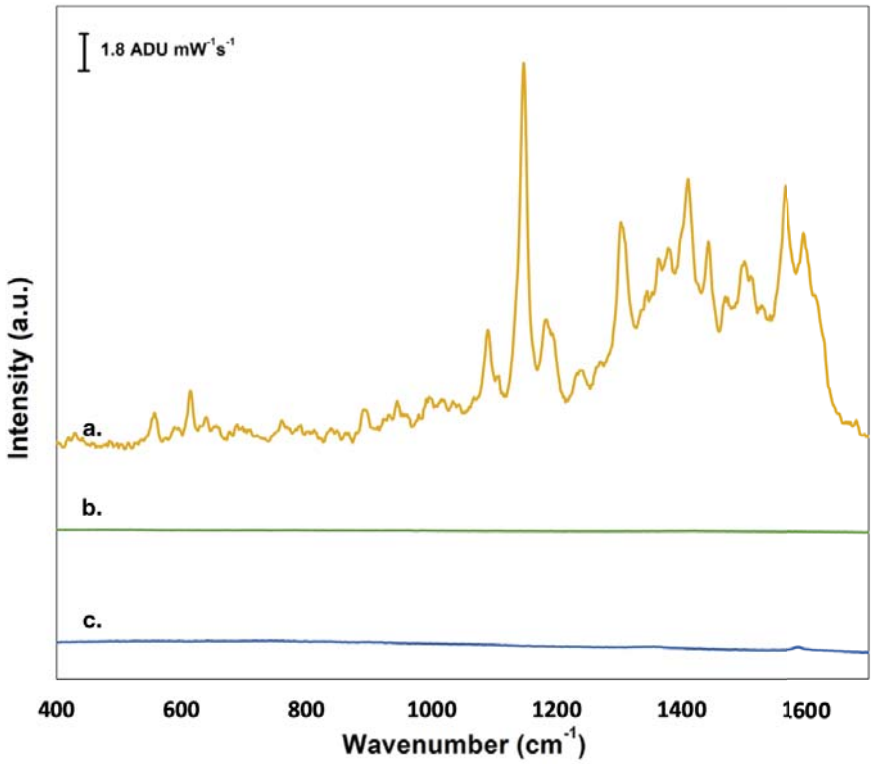

Fig 4.7 a) EC-SERS signals of AGI on the silver-deposited carbon screen-printed electrode (SPE) with -400 mV potential applied. b) background signal on the silver-deposited carbon SPE. c) AGI in buffer solution on the bare carbon SPE.

The SERS intensities registered for the quantitative study are acquired four times for each concentration which is shown in Fig 4.8a. Finally, Fig. 4.8b shows the limit of detection (LOD) calculated for a signal-to-noise ratio of Fig. 4.8a. The linearity occurs in the range from 1 x 10^{-5} M to 2 x 10^{-7} M and the square R of the linear curve is 0.98. Compared with previous SERS study, this report has a broader detection range and low-volume solution but has a relatively lower sensitivity. Two factors, which are the surface interacting area and different particle shapes, are the considered cause. In the previous study [291], the whole surface area of the nanoparticle is available to have interaction with AGI molecules. In this study, the island structure of nanoparticles on the chip limits the interacting area in this work to the exposed area only. Still, it is thought that the silver film could provide a more stable signal than a loosely bound silver particle. Regarding the particle shape, the triangular nanoprism-shaped silver nanoparticles performed the highest sensitivity to AGI molecule among other shapes of nanoparticles. The effect of the shape of the surface is not investigated in this current study. In the future, the triangular nanoprism or other different shapes of AgNPs will be considered to apply for our EC-SERS studies.

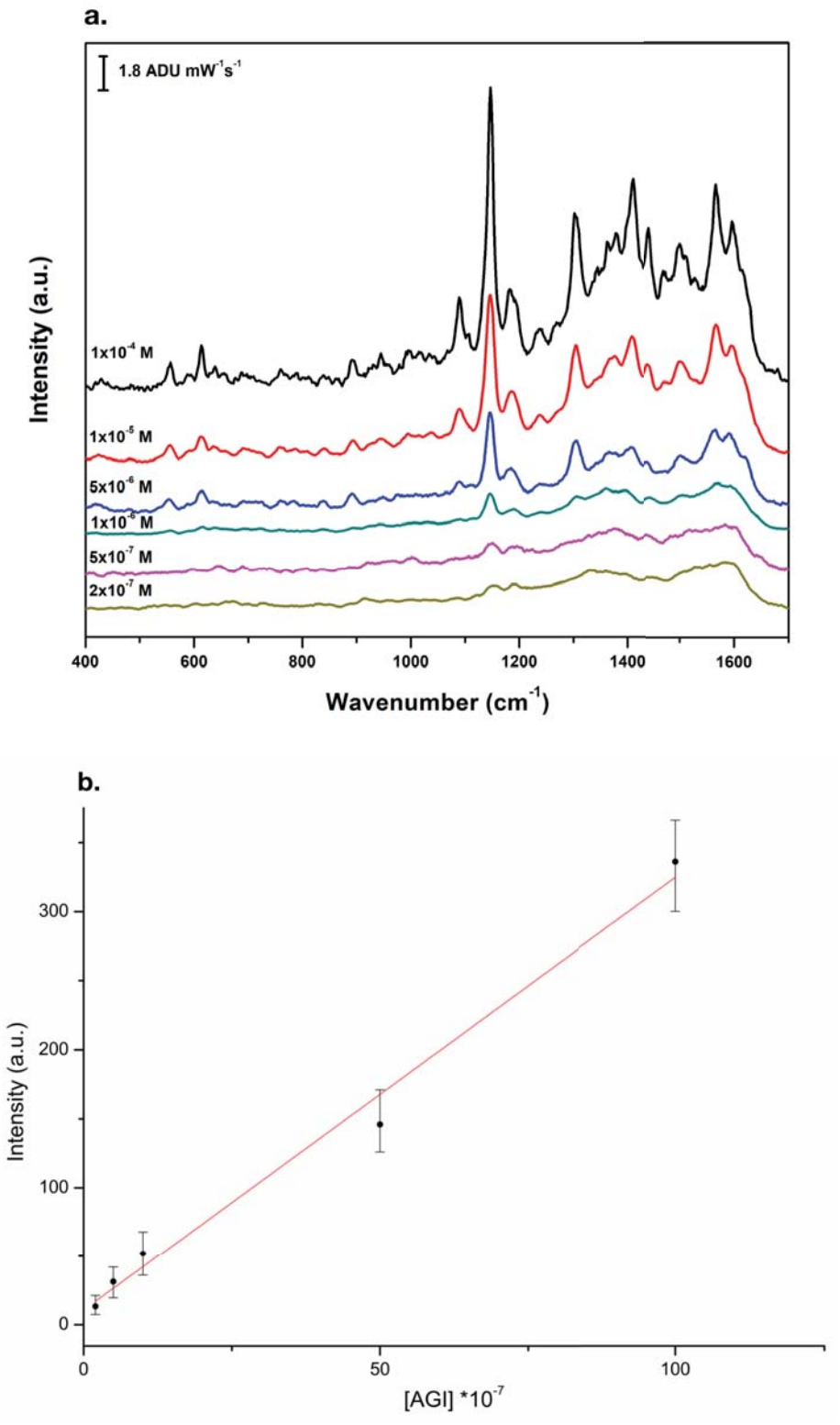

Fig. 4.8 (a) EC-SERS spectra at the applied potential of -400 mV vs Ag/AgCl with enhanced peak signal at 1147 cm^{-1}. I, II, III, IV, V and VI corresponding to the different

concentration of the AGI solution of $1x10^{-4}$, $1x10^{-5}$, $5x10^{-6}$, $1x10^{-6}$, $5x10^{-7}$ and $2x10^{-7}$ M, respectively (b) Calibration curve of different drug concentrations of AGI with good linear dependence (R^2 = 0.98) ranging from $1x10^{-5}$ to $2x10^{-7}$. Error bar represents standard deviation where n = 4.

4.4 Conclusion

The AGI at the low level of concentration was successfully detected on the SERS-active SPE. Cyclic voltammograms (CV) was used to investigate the surface interaction of the AGI molecule. The result shows that the adsorption of AGI on the substrate varies depending on the applied potential. This change is modulated by the protonation state of both the anilinic amino group and the imide, which further determines its interaction mechanism on the surface. The surface interaction mechanism of AGI molecule can be studied through the changes of EC-SERS spectral at different applied potentials. When the applied potential is at -400 mV, the bidentate adsorption of AGI through both the AN and GI binding sites occurs on the surface, which exhibits the most enhanced peak intensities among the other applied potentials. The C-H in-plane bending of the AGI (corresponding to the wavenumber of 1147 cm^{-1}) showed the strongest peak intensity among the other peaks at -400 mV applied potential. A linear dependence of different concentrations in the AGI range occurs from 2 x 10^{-7} to 1 x 10^{-5} M, which corresponds to the range from 40 ng/ml to 2 μg/ml. Compared with the normal SERS spectral (without applied potential), not only more selective peak signals appeared but also increasing signal intensities of the target analyte could be observed through the EC-

SERS spectra. EC-SERS is a promising analytical apparatus that can be employed in the monitoring and rapid detection of the AGI molecule. Future studies will focus on the substrate improvement and explorations of AGI detection in human metabolites such as urine.

Chapter 5. Study of the Mechanism of EC-SERS

5.1 Introduction

Through the EC-SERS experiments of uric acid and AGI, the intensity change and wavenumber shift of SERS spectra can be observed due to the change of molecule orientation and adsorption mode. The EC-SERS experiment of pyridine is conducted in this chapter in order to evaluate the performance of SERS-active SPE and master the SERS characterization as well. The first observation of SERS is from the pyridine adsorbed on electrochemically roughened silver electrode [166]. Till now, thousands of papers are published for studying the pyridine molecule regarding the vibration mode, adsorption mode, selection rules of SERS. This information assists in understanding the features of electrochemical SERS.

5.2 Experimental Preparation

The Raman confocal microscope, potentiostat system, theoretical calculations and the preparation of SERS-active SPEs were the same as those in Chapter 4.

The Pyridine (Py), sodium fluoride, and potassium chloride were purchased from Wako Pure Chemical Industries, Ltd. 0.01 M pyridine + 0.05 M potassium chloride were prepared, and further dilutions were made under Milli-Q water. High-purity Milli-Q water has a resistivity of ≥18.2 MΩ·cm. 0.05 M NaF solution was used as the supporting electrolyte for EC-SERS experiments, and the volume of solution for measurement was 30 μL.

Theoretical calculations were made by using the Gaussian 09 software. Pure liquid Py can be reproduced well using the DFT calculation for free Py at the B3LYP/6-311+G**(C, N, H) level [208], [305].

5.3 Results and discussion

The Py molecule has 11 atoms and C_{2v} symmetry point group which is shown in Fig 5.1. For the molecular coordinates, the x-axis is perpendicular to the molecular plane, the y-axis along the molecular plane and the z-axis is along the C_2. Thus, all these modes are Raman active under the C_{2v} point group [166], [306].

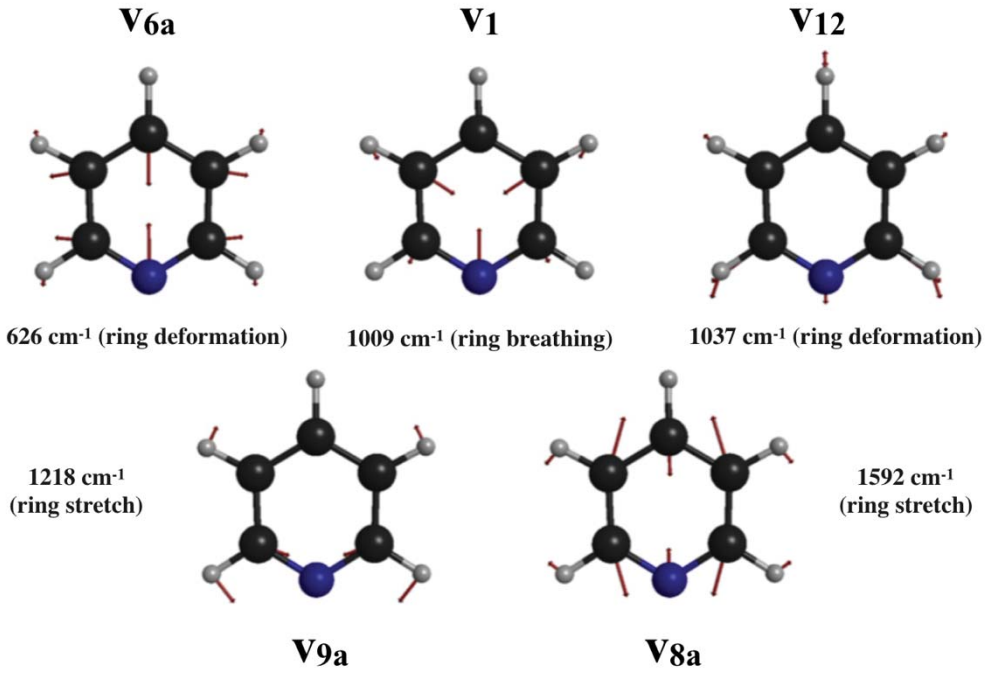

Fig. 5.1 selected normal modes of pyridine.

The potential dependent spectral character is the key issue to be investigated in detail. Fig 5.2 shows the SERS spectra of pyridine with different applied potentials.

The potentials are ramped at -200 mV increment from 0 mV to -1000 mV vs Ag/AgCl. By observing the SERS spectra, there are two changes when the applied potential negatively moves. One is the peak frequencies shift, and the other is the change of the signal intensity. For the former phenomenon, it can be observed that the wavenumber of 1009 and 1037 cm^{-1} shifts to 1007 and 1035 cm^{-1} when the potential applied from -200 mV to -400 mV. For the latter phenomenon, the wavenumber of 626, 1218 and 1592 cm^{-1} become stronger at the applied potential of -600 mV. Besides, the SERS intensity at the wavenumber of 1007 and 1035 cm^{-1} also changes with different applied potentials. Moreover, the SERS signal decreases rapidly when the negative movement of potential to -800 mV, and no SERS signal can be observed when the potential reaches to -1000 mV. The understandings for frequency shift and change of signal intensity are considered as follow.

5.3.1 Frequency shift

The reason for frequency shift is considered relating to the binding interaction between Py molecule and silver nanostructured surface. Therefore, it is essential to understand the adsorption mode of Py to the silver nanostructured surface. There are three different kinds of adsorption modes which are flat configuration with π-type bonding, an upright configuration with a σ bond through the lone-pair electron donation to the unoccupied orbital of metal atoms, and a tilted configuration with a cooperative contribution from the π and σ interaction [307].

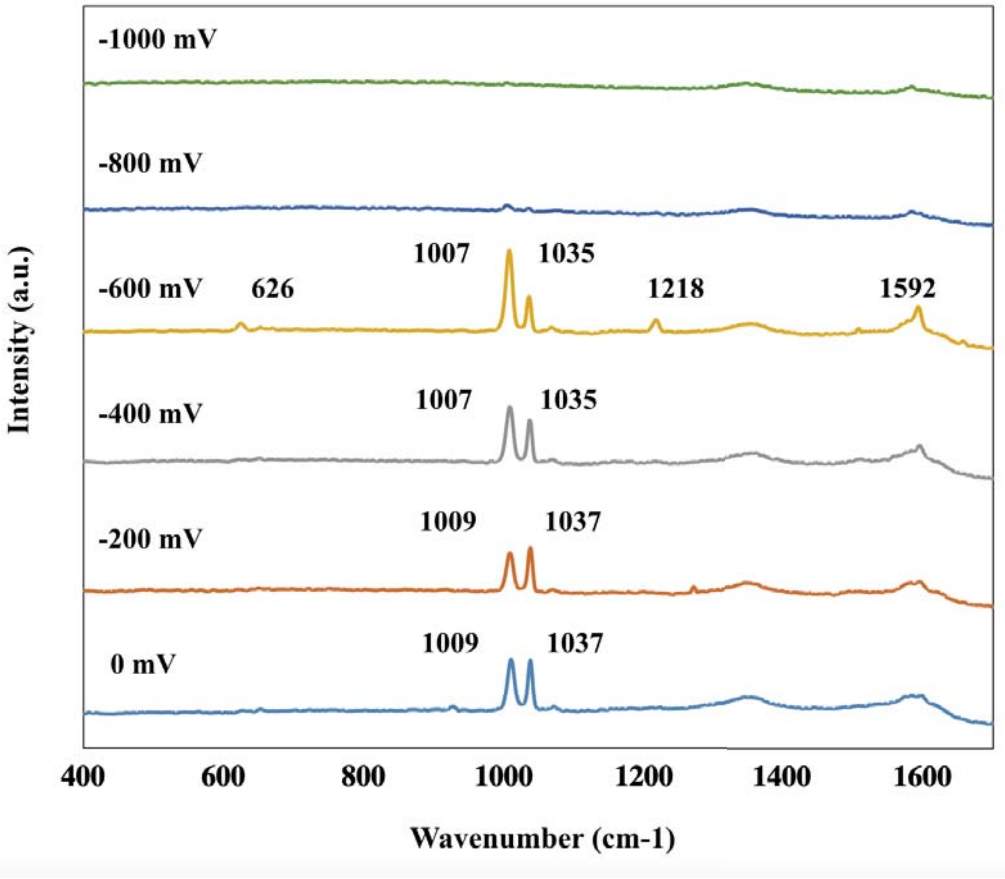

Fig. 5.2 SERS spectral of 0.01 mM pyridine + 0.05 M KCL in 0.05 M NaF solution with different potentials at the SERS-active electrode. The potentials are ramped at -200 mV increment from 0 mV to -1000 mV vs Ag/AgCl. Acquisition time: 60 s, laser power: 2.8 mW.

In this case, Py molecule binds to the silver surface through the long-pair electrons of nitrogen, which adopts an upright configuration. It interacts with the conductance band of the silver surface through σ-type bonding from the $2b_1$ orbital. When the potential moves negative direction, the antibonding character decreases which leads to the shift of frequencies of v_1 modes corresponding to the wavenumber of 1009 cm^{-1} [284]. Besides, due to the interaction between the σ-type orbitals and metal surfaces,

the frequency of the ring deformation mode of aromatic rings decreases significantly at the flat configuration. It causes the shift of frequencies of v_{12} modes corresponding to the wavenumber of 1037 cm^{-1}. In conclusion, the adsorption bond of Py molecule to the silver surface will weaken when the applied potential negatively moves, leading to the shift in the vibrational frequencies.

5.3.2 Change of SERS intensity

The CT mechanism is considered as the main factor for SERS intensity change [214], [267], [268], [280], [309]–[312]. When the applied potential reaches -600mV, The result shows the SERS signal of the v_{6a}, v_1, v_{9a} and v_{8a} modes corresponding to the wavenumber of 626, 1007, 1218 and 1592 cm^{-1} are strongly enhanced when resonance condition is satisfied [208]. While the SERS signal of the v_{12} band (1037 cm^{-1}) decreases because of the electron transition from the Fermi level of the silver surface during the CT process [313]. Besides, the Huang–Rhys factor is introduced in order to measure the displacement of the adsorbed molecule at the excited and ground states in the CT process. For the v_{6a}, v_1, v_{9a}, and v_{8a} modes, the Huang–Rhys factor are 0.152, 0.309, 0.339 and 0.288, respectively. While for v_{12} mode, the Huang–Rhys factor is only 0.035. Therefore, the former four modes are greatly magnified compared with the latter one [314].

5.3.3 EC-SERS of uric acid and AGI

Compared with EC-SERS experiments of pyridine, the SERS signals of uric acid changes differently when negative potential is applied. There are no apparent peak shifts for the EC-SERS experiments of uric acid. It is considered the adsorption bond of uric acid is not enhanced or weaken when changing different potentials, resulting in the no blueshift or redshift in the vibrational frequencies. For the SERS intensity, the intensity signal increases and then decreases with the negative movement of the electrode potential. Combined with Fig 1.9, this change of SERS intensity could be explained through the photon-driven CT from metal to molecule using the concept of energy level or energy states. In this case, the applied potential of -1400 mV is like to the V_2 in Fig 1.9, which leads to the excitation energy matching the required CT energy, causing a significant enhancement in the SERS intensity. When applied the potential is less or more than -1400 mV, the excitation energy does not fall in an ideal resonance condition. Therefore, the SERS signal will decrease.

About the EC-SERS experiment of AGI, it is more complicated that the absorption mode of AGI changes when applied different potentials. When applied potential reaches -200 mV, the SERS signal of wavenumber of 1575 cm^{-1} increased which assigned to the NH_3^+ rocking of anilinic part of AGI. It implies that of the monodentate interaction between aniline moiety and silver nanoparticles. When applied potential to -400 mV, SERS intensities are strongly enhanced appearing at the wavenumber of 1147, 1302 and 1566 cm^{-1}, which can be assigned to C-H / CH_2 bending, CH_2 wagging and

NH_3^+ rocking, respectively. These bands can be attributed to both the aniline and glutarimide parts of AGI. This phenomenon suggests that interaction mode between adsorbates and substrate turns from the monodentate to the bidentate interaction. When applied potential increases to -600 mV, SERS intensities are decreased at the wavenumber of 1147 and 1566 cm^{-1}, which are attributed to aniline moiety. In contrast, GI bands can be observed at the wavenumber of 948 and 1313 cm^{-1} corresponding to C-N-C / CH_3 bending and CH_2 wagging, respectively. It indicated that the interaction mode turns from the bidentate to the monodentate interaction between glutarimide moiety and silver nanoparticles.

5.4 Conclusion

The pyridine molecule is successfully detected on the silver-sputtered carbon SPE. From the EC-SERS experiments, the phenomenon of wavenumber shift and SERS intensity change can be observed. The reason can be explained through analyzing the adsorption bond of Py molecule to the silver surface and CT mechanism. It helps to understand the mechanisms of SERS and EC-SERS spectra from electrochemical adsorption and reaction.

Chapter 6. Conclusion and Future Remarks

The fabrications of SERS-active electrodes have been successfully conducted through sputtering deposition. On both carbon and gold working electrodes, the island structures of silver nanoparticle can be observed through 12 s sputtering deposition. It is worth mentioning that thickness errors of continuous 5 batches of silver sputtering coating are ±0.1 nm which shows fairly good reproducibility by sputtering deposition. It is reasonable to conclude that the sputtering method is extremely applicable for the manufacture of SERS-active SPEs. Through this rapid, reproducible and mass producible fabrication method, it is considered as a promising analysis platform.

According to the SERS experiments of R6G, the SERS signals of 12 s silver-deposited film were the strongest among those at the other structure of silver-deposited films for both carbon and gold working electrodes. Compared with Ag/C structure, the SERS enhancement of Ag/Au structure was much stronger. The enhancement factors of Ag/C and Ag/Au structure were estimated as 2.8×10^5 and 2.2×10^7, respectively.

The three kinds of substrates (glass epoxy, paper, and PET) have used for fabricating SERS-active SPE. The SERS signals were able to be observed at all kinds of the substrate even at the paper electrode which demonstrated the applicability of the sputtering method for producing SERS-active SPEs. Among the three kinds of substrates of SPE, SERS signals of R6G were the most enhanced on the PET substrate.

Low background noise of SERS signals and a high signal-to-noise ratio could be observed on the SERS-active SPE fabricated by the sputtering deposition method. In

addition, larger surface adsorption area for target molecules is present and further surface modification can be easily done if desired. As the results, the sensitivities of uric acid and pyridine are both higher than previous EC-SERS works.

The spectroelectrochemical investigation of uric acid indicated that applying a proper negative potential on the electrode led to a significant effect on SERS signals enhancements. It could be observed that the intensity signal was gradually enhanced with more negative applied potential until the applied potential reached -1400 mV. The peak intensities of strongly enhanced wavenumbers were calculated which were 632cm^{-1}, 807cm^{-1}, 881cm^{-1}, 1133cm^{-1} and 1202 cm^{-1}. This phenomenon suggested that the uric acid molecule adopted vertical mode and kept a distance from the surface. Besides, it implied that the excitation energy fitted with the required CT energy due to the increase of the Fermi level. It was interesting that the redox peaks around -1400 mV in CV data were corresponding to the most enhanced EC-SERS signal. The limited of detection of uric acid reached 10 μM by EC-SERS measurement which was 10 times more sensitive than that of previous work.

The AGI was successfully detected on the SERS-active SPE at a low level of concentration. The result shows that the adsorption of AGI on the SERS-active SPE varies depending on the applied potential through the Cyclic voltammograms (CV) analysis. The change of EC-SERS spectra at different applied potentials suggests the surface interaction mechanism of AGI molecule. When the applied potential is at -400mV, the bidentate adsorption of AGI occurs on the surface, which manifests the

most enhanced peak intensities among the other applied potentials. A linear dependence of different concentrations in the AGI range occurs from 2 x 10^{-7} to 1 x 10^{-5} M. Compared with the normal SERS spectral, both more selective peak signals appeared and increasing signal intensities of the target analyte could be observed through the EC-SERS spectra.

EC-SERS is a promising analytical tool that can be used in the monitoring and rapid detection of the molecule. By properly applied potentials on the electrode, the surface condition can be changed to a suitable state for biomolecule interaction. It benefits both the enhanced sensitivity of SERS signal and the selectivity for detection. It is convinced that EC-SERS technology will play an essential role in the growing demand in biological and biomedical applications in the future.

Cited Reference

Chapter 1

[1] M. Cremer, "Über die Ursache der elektromotorischen Eigenschaften der Gewebe, zugleich ein Beitrag zur Lehre von polyphasischen Elektrolytketten," *Z. Biol.*, 1906.

[2] E. G. Griffin and J. M. Nelson, "THE INFLUENCE OF CERTAIN SUBSTANCES ON THE ACTIVITY OF INVERTASE.," *J. Am. Chem. Soc.*, vol. 38, no. 3, pp. 722–730, Mar. 1916.

[3] J. M. Nelson and E. G. Griffin, "ADSORPTION OF INVERTASE.," *J. Am. Chem. Soc.*, vol. 38, no. 5, pp. 1109–1115, May 1916.

[4] W. S. Hughes, "THE POTENTIAL DIFFERENCE BETWEEN GLASS AND ELECTROLYTES IN CONTACT WITH THE GLASS," *J. Am. Chem. Soc.*, vol. 44, no. 12, pp. 2860–2867, Dec. 1922.

[5] A. M. Tonkin *et al.*, "Clinical relevance of statins: their role in secondary prevention.," *Atheroscler. Suppl.*, 2001.

[6] J. Wang, "Electrochemical glucose biosensors," in *Electrochemical Sensors, Biosensors and their Biomedical Applications*, 2008.

[7] J. Wang, "Glucose biosensors: 40 Years of advances and challenges," *Electroanalysis*. 2001.

[8] M. M. Rahman, A. J. S. Ahammad, J. H. Jin, S. J. Ahn, and J. J. Lee, "A comprehensive review of glucose biosensors based on nanostructured metal-oxides," *Sensors*, 2010.

[9] Y. Lin, F. Lu, Y. Tu, and Z. Ren, "Glucose Biosensors Based on Carbon Nanotube Nanoelectrode Ensembles," *Nano Lett.*, 2004.

[10] J. L. Hammond, N. Formisano, P. Estrela, S. Carrara, and J. Tkac, "Electrochemical biosensors and nanobiosensors," *Essays Biochem.*, 2016.

[11] X. Zhang, H. Ju, and J. Wang, *Electrochemical Sensors, Biosensors And Their Biomedical Applications*. 2008.

[12] S. Vigneshvar, C. C. Sudhakumari, B. Senthilkumaran, and H. Prakash, “Recent Advances in Biosensor Technology for Potential Applications – An Overview,” *Front. Bioeng. Biotechnol.*, 2016.

[13] G. G. Guilbault and J. G. Montalvo, “Urea-specific enzyme electrode,” *J. Am. Chem. Soc.*, vol. 91, no. 8, pp. 2164–2165, Apr. 1969.

[14] B. H. van der Schoot and P. Bergveld, “ISFET based enzyme sensors,” *Biosensors*, 1987.

[15] S. Vigneshvar *et al.*, “Glucose biosensors: 40 Years of advances and challenges,” *Electrochem. Sensors, Biosens. their Biomed. Appl.*, 2008.

[16] V. W. S. Hung and K. Kerman, “Carbon nanotubes: Advances, integration and applications to printable electrode-based biosensors,” in *Nanobiosensors and Nanobioanalyses*, 2015.

[17] S. Suzuki, F. Takahashi, I. Satoh, and N. Sonobe, “Ethanol and Lactic Acid Sensors Using Electrodes Coated with Dehydrogenase-Collagen Membranes,” *Bulletin of the Chemical ….* 1975.

[18] “Biochemical electrode uses tissue slices,” *Chem. Eng. News Arch.*, vol. 56, no. 41, p. 16, Oct. 1978.

[19] J. J. Baumberg *et al.*, “Angle-resolved surface-enhanced raman scattering on metallic nanostructured plasmonic crystals,” *Nano Lett.*, vol. 5, no. 11, pp. 2262–2267, 2005.

[20] A. E. G. Cass *et al.*, “Ferrocene-mediated enzyme electrode for amperometric determination of glucose,” *Anal. Chem.*, vol. 56, no. 4, pp. 667–671, Apr. 1984.

[21] C. Karunakaran, R. Rajkumar, and K. Bhargava, “Introduction to Biosensors,” *Biosensors and Bioelectronics*, 2015.

[22] Q. Xiang, “The development and application of electrochemical biosensor,” in *Communications in Computer and Information Science*, 2011.

[23] J. P. Chambers, B. P. Arulanandam, L. L. Matta, A. Weis, and J. J. Valdes, “Biosensor recognition elements,” *Current Issues in Molecular Biology*. 2008.

[24] M. A. Cooper, “Optical biosensors in drug discovery,” *Nat. Rev. Drug Discov.*, 2002.

[25] J. Kirsch, C. Siltanen, Q. Zhou, A. Revzin, and A. Simonian, “Biosensor technology: Recent advances in threat agent detection and medicine,” *Chemical Society Reviews*. 2013.

[26] A. J. Haes, L. Chang, W. L. Klein, and R. P. Van Duyne, “Detection of a biomarker for Alzheimer’s disease from synthetic and clinical samples using a nanoscale optical biosensor,” *J. Am. Chem. Soc.*, 2005.

[27] J. V. Rushworth, A. Ahmed, H. H. Griffiths, N. M. Pollock, N. M. Hooper, and P. A. Millner, “A label-free electrical impedimetric biosensor for the specific detection of Alzheimer’s amyloid-beta oligomers,” *Biosens. Bioelectron.*, 2014.

[28] M. Mimee *et al.*, “An ingestible bacterial-electronic system to monitor gastrointestinal health,” *Science (80-.).*, 2018.

[29] X. Li *et al.*, “Digital Health: Tracking Physiomes and Activity Using Wearable Biosensors Reveals Useful Health-Related Information,” *PLoS Biol.*, 2017.

[30] M. Soler, M. C. Estevez, M. de L. Moreno, A. Cebolla, and L. M. Lechuga, “Label-free SPR detection of gluten peptides in urine for non-invasive celiac disease follow-up,” *Biosens. Bioelectron.*, 2016.

[31] H. Shafiee *et al.*, “Nanostructured optical photonic crystal biosensor for HIV viral load measurement,” *Sci. Rep.*, 2014.

[32] J. U. Sprenger *et al.*, “In vivo model with targeted cAMP biosensor reveals changes in receptor-microdomain communication in cardiac disease,” *Nat. Commun.*, 2015.

[33] S. Farid *et al.*, “Detection of Interferon gamma using graphene and aptamer based FET-like electrochemical biosensor,” *Biosens. Bioelectron.*, 2015.

[34] G. Maduraiveeran, M. Sasidharan, and V. Ganesan, “Electrochemical sensor and biosensor platforms based on advanced nanomaterials for biological and biomedical applications,” *Biosensors and Bioelectronics*. 2018.

[35] A. Stett *et al.*, “Biological application of microelectrode arrays in drug discovery and basic research,” *Analytical and Bioanalytical Chemistry*. 2003.

[36] R. L. Rich and D. G. Myszka, “Why you should be using more SPR biosensor technology,” *Drug Discov. Today Technol.*, 2004.

[37] Y. Fang, *Label-free biosensor methods in drug discovery*. 2015.

[38] D. R. Baselt, G. U. Lee, M. Natesan, S. W. Metzger, P. E. Sheehan, and R. J. Colton, “A biosensor based on magnetoresistance technology,” *Biosens. Bioelectron.*, 1998.

[39] A. Olaru, C. Bala, N. Jaffrezic-Renault, and H. Y. Aboul-Enein, “Surface Plasmon Resonance (SPR) Biosensors in Pharmaceutical Analysis,” *Critical Reviews in Analytical Chemistry*. 2015.

[40] M. A. Cooper, “Current biosensor technologies in drug discovery,” *Drug Discov. World*, 2006.

[41] V. Ramanathan and N. Vachharajani, “Protein Binding in Drug Discovery and Development,” in *Evaluation of Drug Candidates for Preclinical Development: Pharmacokinetics, Metabolism, Pharmaceutics, and Toxicology*, 2010.

[42] S. Rodriguez-Mozaz, M. J. Lopez De Alda, and D. Barceló, “Biosensors as useful tools for environmental analysis and monitoring,” *Analytical and Bioanalytical Chemistry*. 2006.

[43] R. Tecon and J. R. Van Der Meer, “Bacterial biosensors for measuring availability of environmental pollutants,” *Sensors*. 2008.

[44] A. J. Baeumner, “Biosensors for environmental pollutants and food contaminants,” *Analytical and Bioanalytical Chemistry*. 2003.

[45] F. Long, A. Zhu, and H. Shi, “Recent advances in optical biosensors for environmental monitoring and early warning,” *Sensors (Switzerland)*. 2013.

[46] S. Rodriguez-Mozaz, M.-P. Marco, M. J. L. de Alda, and D. Barceló, “Biosensors for environmental applications: Future development trends,” *Pure Appl. Chem.*, 2004.

[47] J. Bjerketorp, S. Håkansson, S. Belkin, and J. K. Jansson, “Advances in preservation methods: Keeping biosensor microorganisms alive and active,” *Current Opinion in Biotechnology*. 2006.

[48] X. Wang, X. Lu, and J. Chen, “Development of biosensor technologies for analysis of environmental contaminants,” *Trends in Environmental Analytical Chemistry*. 2014.

[49] C. Y. Shao, C. J. Howe, A. J. R. Porter, and L. A. Glover, “Novel cyanobacterial biosensor for detection of herbicides,” *Appl. Environ. Microbiol.*, 2002.

[50] A. M. Horsburgh *et al.*, “On-line microbial biosensing and fingerprinting of water pollutants,” *Biosens. Bioelectron.*, 2002.

[51] Y. Amano and Q. Cheng, “Detection of influenza virus: Traditional approaches and development of biosensors,” *Analytical and Bioanalytical Chemistry*. 2005.

[52] K. Yanamandra *et al.*, “Anti-tau antibodies that block tau aggregate seeding invitro markedly decrease pathology and improve cognition in vivo,” *Neuron*, 2013.

[53] A. J. Haes, W. P. Hall, L. Chang, W. L. Klein, and R. P. Van Duyne, “A localized surface plasmon resonance biosensor: First steps toward an assay for Alzheimer’s disease,” *Nano Lett.*, 2004.

[54] P. J. Conroy, S. Hearty, P. Leonard, and R. J. O’Kennedy, “Antibody production, design and use for biosensor-based applications,” *Seminars in Cell and Developmental Biology*. 2009.

[55] A. Y. Zhu, F. Yi, J. C. Reed, H. Zhu, and E. Cubukcu, “Optoelectromechanical multimodal biosensor with graphene active region,” *Nano Lett.*, 2014.

[56] A. L. Chua, C. Y. Yean, M. Ravichandran, B. H. Lim, and P. Lalitha, “A rapid DNA biosensor for the molecular diagnosis of infectious disease,” *Biosens. Bioelectron.*, 2011.

[57] M. L. Sin, K. E. Mach, P. K. Wong, and J. C. Liao, “Advances and challenges in biosensor-based diagnosis of infectious diseases,” *Expert Review of Molecular Diagnostics*. 2014.

[58] A. J. Webb *et al.*, “A protease-based biosensor for the detection of schistosome cercariae,” *Sci. Rep.*, 2016.

[59] R. Singh *et al.*, “DNA biosensor for detection of Neisseria gonorrhoeae causing sexually transmitted disease,” *J. Biotechnol.*, 2010.

[60] Y. Fang, A. M. Ferrie, N. H. Fontaine, J. Mauro, and J. Balakrishnan, “Resonant waveguide grating biosensor for living cell sensing,” *Biophys. J.*, 2006.

[61] R. T. Hill, “Plasmonic biosensors,” *Wiley Interdisciplinary Reviews: Nanomedicine and Nanobiotechnology*. 2015.

[62] J. H. Lee, K. S. Hwang, J. Park, K. H. Yoon, D. S. Yoon, and T. S. Kim, “Immunoassay of prostate-specific antigen (PSA) using resonant frequency shift of piezoelectric nanomechanical microcantilever,” in *Biosensors and Bioelectronics*, 2005.

[63] B. Sepúlveda, P. C. Angelomé, L. M. Lechuga, and L. M. Liz-Marzán, “LSPR-based nanobiosensors,” *Nano Today*. 2009.

[64] J. L. Hammond, N. Bhalla, S. D. Rafiee, and P. Estrela, “Localized surface plasmon resonance as a biosensing platform for developing countries,” *Biosensors*. 2014.

[65] X. Fan, I. M. White, S. I. Shopova, H. Zhu, J. D. Suter, and Y. Sun, “Sensitive optical biosensors for unlabeled targets: A review,” *Analytica Chimica Acta*. 2008.

[66] S. M. Yoo and S. Y. Lee, “Optical Biosensors for the Detection of Pathogenic Microorganisms,” *Trends in Biotechnology*. 2016.

[67] X. Guo, “Surface plasmon resonance based biosensor technique: A review,” *Journal of Biophotonics*. 2012.

[68] M. Seydack, “Nanoparticle labels in immunosensing using optical detection methods,” *Biosensors and Bioelectronics*. 2005.

[69] F. Lammers and T. Scheper, “Thermal biosensors in biotechnology,” *Adv Biochem Eng Biotechnol*, 1999.

[70] P. Mehrotra, “Biosensors and their applications - A review,” *Journal of Oral Biology and Craniofacial Research*. 2016.

[71] C. S. Lee, S. Kyu Kim, and M. Kim, “Ion-sensitive field-effect transistor for biological sensing,” *Sensors*. 2009.

[72] M. Yuqing, G. Jianguo, and C. Jianrong, “Ion sensitive field effect transducer-based biosensors,” *Biotechnology Advances*. 2003.

[73] P. Bergveld, “The development and application of FET-based biosensors,” *Biosensors*, 1986.

[74] M. Badihi-Mossberg, V. Buchner, and J. Rishpon, “Electrochemical biosensors for pollutants in the environment,” *Electroanalysis*. 2007.

[75] D. Grieshaber, R. MacKenzie, J. Vörös, and E. Reimhult, “Electrochemical biosensors - Sensor principles and architectures,” *Sensors*. 2008.

[76] D. R. Thévenot, K. Toth, R. A. Durst, and G. S. Wilson, “Electrochemical biosensors: Recommended definitions and classification,” *Biosens. Bioelectron.*, 2001.

[77] M. Amasia and M. Madou, “Large-volume centrifugal microfluidic device for blood plasma separation,” *Bioanalysis*, 2010.

[78] T. Ichiki, Y. Sugiyama, R. Taura, T. Koidesawa, and Y. Horiike, “Plasma applications for biochip technology,” in *Thin Solid Films*, 2003.

[79] V. Appierto, M. Callari, E. Cavadini, D. Morelli, M. G. Daidone, and P. Tiberio, “A lipemia-independent NanoDrop®-based score to identify hemolysis in plasma and serum samples,” *Bioanalysis*, 2014.

[80] T. Cabras *et al.*, “Top-down analytical platforms for the characterization of the human salivary proteome,” *Bioanalysis*. 2014.

[81] A. J. Ji, Z. Jiang, Y. Livson, J. A. Davis, J. X. Chu, and N. Weng, “Challenges in urine bioanalytical assays: Overcoming nonspecific binding,” *Bioanalysis*, 2010.

[82] J. Barbosa *et al.*, “Hair as an alternative matrix in bioanalysis,” *Bioanalysis*. 2013.

[83] F. Xie, T. Liu, W. J. Qian, V. A. Petyuk, and R. D. Smith, “Liquid chromatography-mass spectrometry-based quantitative proteomics,” *Journal of Biological Chemistry*. 2011.

[84] W. M. A. Niessen, *Liquid Chromatography-Mass Spectrometry, Third Edition*. 2006.

[85] M. J. Kang, Y. H. Hwang, W. Lee, and D. H. Kim, “Validation and application of a screening method for beta 2-agonists, anti-estrogenic substances and mesocarb in human urine using liquid chromatography/tandem mass spectrometry,” *Rapid Commun. Mass Spectrom.*, 2007.

[86] S. Moco *et al.*, “A Liquid Chromatography-Mass Spectrometry-Based Metabolome Database for Tomato,” *PLANT Physiol.*, 2006.

[87] A. K. Malik, C. Blasco, and Y. Picó, “Liquid chromatography-mass spectrometry in food safety,” *Journal of Chromatography A*. 2010.

[88] U. Mareck, G. Sigmund, G. Opfermann, H. Geyer, and W. Schänzer, “Identification of the aromatase inhibitor aminoglutethimide in urine by gas chromatography/mass spectrometry,” *Rapid Commun. Mass Spectrom.*, 2002.

[89] J. Lisec, N. Schauer, J. Kopka, L. Willmitzer, and A. R. Fernie, “Gas chromatography mass spectrometry-based metabolite profiling in plants,” *Nat. Protoc.*, 2006.

[90] O. D. Sparkman, Z. Penton, and F. G. Kitson, *Gas Chromatography and Mass Spectrometry: A Practical Guide*. 2011.

[91] K. K. Pasikanti, P. C. Ho, and E. C. Y. Chan, “Gas chromatography/mass spectrometry in metabolic profiling of biological fluids,” *Journal of Chromatography B: Analytical Technologies in the Biomedical and Life Sciences*. 2008.

[92] C. H. Evans, “Introduction to mass spectrometry,” *Trends Biochem. Sci.*, 1986.

[93] a. . Jackson, “An introduction to mass spectrometry,” *Endeavour*, 1982.

[94] T. Soga, Y. Ohashi, Y. Ueno, H. Naraoka, M. Tomita, and T. Nishioka, "Quantitative Metabolome Analysis Using Capillary Electrophoresis Mass Spectrometry," *J. Proteome Res.*, 2003.

[95] W. M. A. Niessen, U. R. Tjaden, and J. van der Greef, "Capillary electrophoresis-mass spectrometry," *J. Chromatogr. A*, 1993.

[96] P. Schmitt-Kopplin and M. Frommberger, "Capillary electrophoresis-mass spectrometry: 15 years of developments and applications," *Electrophoresis*, 2003.

[97] M. V. Novotny, K. A. Cobb, and J. Liu, "Recent advances in capillary electrophoresis of proteins, peptides and amino acids," *Electrophoresis*, 1990.

[98] R. D. Smith, J. A. Loo, C. G. Edmonds, C. J. Barinaga, and H. R. Udseth, "Sensitivity considerations for large molecule detection by capillary electrophoresis-electrospray ionization mass spectrometry," *J. Chromatogr. A*, 1990.

[99] M. Sugimoto, D. T. Wong, A. Hirayama, T. Soga, and M. Tomita, "Capillary electrophoresis mass spectrometry-based saliva metabolomics identified oral, breast and pancreatic cancer-specific profiles," *Metabolomics*, 2010.

[100] C. Simó, C. Barbas, and A. Cifuentes, "Capillary electrophoresis-mass spectrometry in food analysis," *Electrophoresis*. 2005.

[101] D. C. Harrison, "Chromatography," *Nature*, 1955.

[102] P. Bailon, G. K. Ehrlich, W. Fung, W. Berthold, M. Wilchek, and I. Chaiken, "Chromatography Edited by An Overview of Affinity Chromatography," *Mol. Biochem. Parasitol.*, 2000.

[103] L. Castelletti, B. Verzola, C. Gelfi, A. Stoyanov, and P. G. Righetti, "chromatography," *J. Chromatogr. A*, 2000.

[104] A. Williams, "Overview Of Conventional Chromatography," in *Handbook of Food Analytical Chemistry*, 2005.

[105] F. Hernández and M. Ibáñez, *Liquid Chromatography*. 2013.

[106] R. D. Conlon, "Liquid Chromatography Detectors," *Anal. Chem.*, 1969.

[107] V. R. Meyer, “High-performance liquid chromatography (HPLC),” in *Practical Methods in Cardiovascular Research*, 2005.

[108] G. Chromatography and L. Chromatography, “Gas Chromatography (GC) and Liquid Chromatography (LC),” *Education*, 2003.

[109] C. A. Cramers and H. M. McNair, “Gas chromatography,” *J. Chromatogr. Libr.*, 1983.

[110] L. Pauling, A. B. Robinson, R. Teranishi, and P. Cary, “Quantitative Analysis of Urine Vapor and Breath by Gas-Liquid Partition Chromatography,” *Proc. Natl. Acad. Sci.*, 1971.

[111] W. Jennings, E. Mittlefehldt, and P. Stremple, *Analytical Gas Chromatography*. 1997.

[112] B. d’Acampora Zellner, P. Dugo, G. Dugo, and L. Mondello, “Gas chromatography-olfactometry in food flavour analysis,” *Journal of Chromatography A*. 2008.

[113] S. C. Terry, J. H. Herman, and J. B. Angell, “A Gas Chromatographic Air Analyzer Fabricated on a Silicon Wafer,” *IEEE Trans. Electron Devices*, 1979.

[114] S. H. Y. Wong, “Supercritical fluid chromatography,” in *Handbook of Analytical Therapeutic Drug Monitoring and Toxicology*, 2017.

[115] L. T. Taylor, “Supercritical fluid chromatography in perspective,” *Chim. Oggi*, 2008.

[116] S. M. Pourmortazavi and S. S. Hajimirsadeghi, “Supercritical fluid extraction in plant essential and volatile oil analysis,” *Journal of Chromatography A*. 2007.

[117] R. D. Strickland, “Electrophoresis,” *Anal. Chem.*, 1968.

[118] A. S. Dukhin and P. J. Goetz, “Fundamentals of interface and colloid science,” *Stud. Interface Sci.*, 2010.

[119] M. H. Blees, “Foundations of Colloid Science,” *Colloids Surfaces A Physicochem. Eng. Asp.*, 2002.

[120] D. Rosen, “Electrokinetic phenomena,” *Phys. Educ.*, 1971.

[121] R. E. Challis, M. J. W. Povey, M. L. Mather, and A. K. Holmes, “Ultrasound techniques for characterizing colloidal dispersions,” *Reports Prog. Phys.*, 2005.

[122] E. C. Hulme and M. A. Trevethick, “Ligand binding assays at equilibrium: Validation and interpretation,” *British Journal of Pharmacology*. 2010.

[123] J. M. Sailstad, R. R. Bowsher, O. F. Laterza, and W. Nowatzke, “Ligand Binding Assays in Drug Development,” in *The Immunoassay Handbook*, 2013.

[124] L. A. A. De Jong, D. R. A. Uges, J. P. Franke, and R. Bischoff, “Receptor-ligand binding assays: Technologies and applications,” *Journal of Chromatography B: Analytical Technologies in the Biomedical and Life Sciences*. 2005.

[125] J. Escorihuela, M. Á. González-Martínez, J. L. López-Paz, R. Puchades, Á. Maquieira, and D. Gimenez-Romero, “Dual-polarization interferometry: A novel technique to light up the nanomolecular world,” *Chemical Reviews*. 2015.

[126] V. C. Özalp, “Dual-polarization interferometry for quantification of small molecules using aptamers,” *Anal. Bioanal. Chem.*, 2012.

[127] A. Boudjemline, D. T. Clarke, N. J. Freeman, J. M. Nicholson, and G. R. Jones, “Early stages of protein crystallization as revealed by emerging optical waveguide technology,” *J. Appl. Crystallogr.*, 2008.

[128] A. Mashaghi, M. Swann, J. Popplewell, M. Textor, and E. Reimhult, “Optical anisotropy of supported lipid structures probed by waveguide spectroscopy and its application to study of supported lipid bilayer formation kinetics,” *Anal. Chem.*, 2008.

[129] G. Y. Wiederschain, “The ELISA guidebook,” *Biochem.*, 2009.

[130] Thermo Scientific, “ELISA technical guide and protocols,” *Thermo Sci.*, 2010.

[131] P. J. Tighe, R. R. Ryder, I. Todd, and L. C. Fairclough, “ELISA in the multiplex era: Potentials and pitfalls,” *Proteomics - Clinical Applications*. 2015.

[132] R. M. Lequin, “Enzyme immunoassay (EIA)/enzyme-linked immunosorbent assay (ELISA),” *Clin. Chem.*, 2005.

[133] G. N. Konstantinou, “Enzyme-linked immunosorbent assay (ELISA),” in *Methods in Molecular Biology*, 2017.

[134] L. Asensio, I. González, T. García, and R. Martín, “Determination of food authenticity by enzyme-linked immunosorbent assay (ELISA),” *Food Control*. 2008.

[135] P. I. Nikitin, P. M. Vetoshko, and T. I. Ksenevich, “Magnetic Immunoassays,” *Sens. Lett.*, 2007.

[136] A. L. Lin and H. Y. Monica Way, “Functional Magnetic Resonance Imaging,” in *Pathobiology of Human Disease: A Dynamic Encyclopedia of Disease Mechanisms*, 2014.

[137] “Radioimmunoassay,” *Acta Med. Scand.*, 1977.

[138] R. D. Grange, J. P. Thompson, D. G. Lambert, and R. P. Mahajan, “Radioimmunoassay, enzyme and non-enzyme-based immunoassays,” *British Journal of Anaesthesia*. 2014.

[139] M. M. Richter, “Electrochemiluminescence,” in *Optical Biosensors*, 2008.

[140] Z. Liu, W. Qi, and G. Xu, “Recent advances in electrochemiluminescence,” *Chem. Soc. Rev.*, 2015.

[141] L. Hu and G. Xu, “Applications and trends in electrochemiluminescence,” *Chemical Society Reviews*. 2010.

[142] H. Li, S. Liu, Z. Dai, J. Bao, and X. Yang, “Applications of nanomaterials in electrochemical enzyme biosensors,” *Sensors*. 2009.

[143] C. B. Faust, “Ultraviolet/visible spectroscopy,” in *Modern Chemical Techniques*, 1992.

[144] Royal Society of Chemistry, “Ultraviolet -Visible Spectroscopy (UV),” *Rsc*, 2009.

[145] V. Scognamiglio, F. Arduini, G. Palleschi, and G. Rea, “Biosensing technology for sustainable food safety,” *TrAC - Trends in Analytical Chemistry*. 2014.

[146] M. Ghasemi-Varnamkhasti *et al.*, “Monitoring the aging of beers using a bioelectronic tongue,” *Food Control*, 2012.

[147] P. Arora, A. Sindhu, N. Dilbaghi, and A. Chaudhury, “Biosensors as innovative tools for the detection of food borne pathogens,” *Biosensors and Bioelectronics*. 2011.

[148] V. Scognamiglio *et al.*, “Biosensors for effective environmental and agrifood protection and commercialization: From research to market,” *Microchimica Acta*. 2010.

[149] G. Rea *et al.*, “Structure-based design of novel Chlamydomonas reinhardtii D1-D2 photosynthetic proteins for herbicide monitoring,” *Protein Sci.*, 2009.

[150] K. R. Rogers and J. N. Lin, “Biosensors for environmental monitoring,” *Biosens. Bioelectron.*, 1992.

[151] V. V. Uslu and G. Grossmann, “The biosensor toolbox for plant developmental biology,” *Current Opinion in Plant Biology*. 2016.

[152] D. Ye, X. Zuo, and C. Fan, “DNA Nanotechnology-Enabled Interfacial Engineering for Biosensor Development,” *Annu. Rev. Anal. Chem.*, 2018.

[153] V. A. Turek, “Raman Scattering,” 2013.

[154] D. Hahn, *Raman Scattering Theory*. 2013.

[155] A. Smekal, “Zur Quantentheorie der Dispersion,” *Naturwissenschaften*, 1923.

[156] C. V. Raman, “A new radiation,” *Proc. Indian Acad. Sci. - Sect. A*, 1953.

[157] R. Singh, “C. V. Raman and the Discovery of the Raman Effect,” *Phys. Perspect.*, 2002.

[158] K. Kneipp, “Surface-enhanced raman scattering,” *Phys. Today*, 2007.

[159] E. J. Blackie, E. C. Le Ru, and P. G. Etchegoin, “Single-molecule surface-enhanced raman spectroscopy of nonresonant molecules,” *J. Am. Chem. Soc.*, 2009.

[160] E. C. Le Ru, E. Blackie, M. Meyer, and P. G. Etchegoint, “Surface enhanced raman scattering enhancement factors: A comprehensive study,” *J. Phys. Chem. C*, 2007.

[161] W. Zhang, X. Cui, B. S. Yeo, T. Schmid, C. Hafner, and R. Zenobi, “Nanoscale roughness on metal surfaces can increase tip-enhanced raman scattering by an order of magnitude,” *Nano Lett.*, 2007.

[162] P. G. Etchegoin, P. D. Lacharmoise, and E. C. Le Ru, “Influence of photostability on single-molecule surface enhanced Raman scattering enhancement factors,” *Anal. Chem.*, 2009.

[163] U. K. Sur, “Surface-enhanced Raman spectroscopy,” *Resonance*, 2010.

[164] G. McNay, D. Eustace, W. E. Smith, K. Faulds, and D. Graham, “Surface-enhanced Raman scattering (SERS) and surface-enhanced resonance raman scattering (SERRS): A review of applications,” *Applied Spectroscopy*. 2011.

[165] R. Aroca, *Surface-Enhanced Vibrational Spectroscopy*. 2007.

[166] M. Fleischmann, P. J. Hendra, and A. J. McQuillan, “Raman spectra of pyridine adsorbed at a silver electrode,” *Chem. Phys. Lett.*, 1974.

[167] D. L. Jeanmaire and R. P. Van Duyne, “Surface raman spectroelectrochemistry. Part I. Heterocyclic, aromatic, and aliphatic amines adsorbed on the anodized silver electrode,” *J. Electroanal. Chem.*, 1977.

[168] M. G. Albrecht and J. A. Creighton, “Anomalously Intense Raman Spectra of Pyridine at a Silver Electrode,” *J. Am. Chem. Soc.*, 1977.

[169] M. A. Young, J. A. Dieringer, and R. P. Van Duyne, “Plasmonic Materials for Surface-Enhanced and Tip-Enhanced Raman Spectroscopy,” in *Tip Enhancement*, 2007.

[170] E. Hao and G. C. Schatz, “Electromagnetic fields around silver nanoparticles and dimers,” *J. Chem. Phys.*, 2004.

[171] Z. Yang, J. Aizpurua, and H. Xu, “Electromagnetic field enhancement in TERS configurations,” *J. Raman Spectrosc.*, 2009.

[172] S. Y. Ding *et al.*, “Nanostructure-based plasmon-enhanced Raman spectroscopy for surface analysis of materials,” *Nature Reviews Materials*. 2016.

[173] E. H. Witlicki *et al.*, “Molecular logic gates using surface-enhanced raman-scattered light,” *J. Am. Chem. Soc.*, 2011.

[174] H. Lin, J. Mock, D. Smith, T. Gao, and M. J. Sailor, “Surface-enhanced Raman scattering from silver-plated porous silicon,” *J. Phys. Chem. B*, 2004.

[175] I. Talian, K. B. Mogensen, A. Oriňák, D. Kaniansky, and J. Hübner, “Surface-enhanced Raman spectroscopy on novel black silicon-based nanostructured surfaces,” *J. Raman Spectrosc.*, 2009.

[176] K. N. Kanipe, P. P. F. Chidester, G. D. Stucky, and M. Moskovits, “Large Format Surface-Enhanced Raman Spectroscopy Substrate Optimized for Enhancement and Uniformity,” *ACS Nano*, 2016.

[177] P. Xu, N. H. Mack, S. H. Jeon, S. K. Doom, X. Han, and H. L. Wang, “Facile fabrication of homogeneous 3D silver nanostructures on gold-supported polyaniline membranes as promising SERS substrates,” *Langmuir*, 2010.

[178] A. Taguchi, N. Hayazawa, K. Furusawa, H. Ishitobi, and S. Kawata, “Deep-UV tip-enhanced Raman scattering,” *J. Raman Spectrosc.*, 2009.

[179] E. P. Hoppmann, W. W. Yu, and I. M. White, “Inkjet-printed fluidic paper devices for chemical and biological analytics using surface enhanced Raman spectroscopy,” *IEEE J. Sel. Top. Quantum Electron.*, 2014.

[180] C. H. Lee, L. Tian, and S. Singamaneni, “Paper-based SERS swab for rapid trace detection on real-world surfaces,” *ACS Appl. Mater. Interfaces*, 2010.

[181] Y. H. Ngo, D. Li, G. P. Simon, and G. Garnier, “Gold nanoparticle-paper as a three-dimensional surface enhanced raman scattering substrate,” *Langmuir*, 2012.

[182] J. J. Laserna, A. D. Campiglia, and J. D. Winefordner, “Mixture Analysis and Quantitative Determination of Nitrogen-Containing Organic Molecules by Surface-Enhanced Raman Spectrometry,” *Anal. Chem.*, 1989.

[183] Y. Chang *et al.*, “Tunable bioadhesive copolymer hydrogels of thermoresponsive poly(N -isopropyl acrylamide) containing zwitterionic polysulfobetaine,” *Biomacromolecules*, 2010.

[184] L. L. Qu, D. W. Li, J. Q. Xue, W. L. Zhai, J. S. Fossey, and Y. T. Long, “Batch fabrication of disposable screen printed SERS arrays,” *Lab Chip*, 2012.

[185] B. J. Kennedy, S. Spaeth, M. Dickey, and K. T. Carron, “Determination of the Distance Dependence and Experimental Effects for Modified SERS Substrates Based on Self-Assembled Monolayers Formed Using Alkanethiols,” *J. Phys. Chem. B*, 1999.

[186] S. S. Masango *et al.*, “High-Resolution Distance Dependence Study of Surface-Enhanced Raman Scattering Enabled by Atomic Layer Deposition,” *Nano Lett.*, 2016.

[187] P. M. Fierro-Mercado and S. P. Hernández-Rivera, “Highly Sensitive Filter Paper Substrate for SERS Trace Explosives Detection,” *Int. J. Spectrosc.*, 2012.

[188] H. Lu, H. Zhang, X. Yu, S. Zeng, K. T. Yong, and H. P. Ho, “Seed-mediated Plasmon-driven Regrowth of Silver Nanodecahedrons (NDs),” *Plasmonics*, 2012.

[189] L. L. Bao, S. M. Mahurin, C. Du Liang, and S. Dai, “Study of silver films over silica beads as a surface-enhanced Raman scattering (SERS) substrate for detection of benzoic acid,” *J. Raman Spectrosc.*, 2003.

[190] S. Ayas *et al.*, “Label-free nanometer-resolution imaging of biological architectures through surface enhanced raman scattering,” *Sci. Rep.*, 2013.

[191] A. Bonifacio, S. Cervo, and V. Sergo, “Label-free surface-enhanced Raman spectroscopy of biofluids: Fundamental aspects and diagnostic applications,” *Analytical and Bioanalytical Chemistry*. 2015.

[192] J. R. Lombardi, R. L. Birke, T. Lu, and J. Xu, “Charge-transfer theory of surface enhanced Raman spectroscopy: Herzberg-Teller contributions,” *J. Chem. Phys.*, 1986.

[193] J. R. Lombardi and R. L. Birke, “A unified approach to surface-enhanced raman spectroscopy,” *J. Phys. Chem. C*, 2008.

[194] C. Langhammer, Z. Yuan, I. Zorić, and B. Kasemo, “Plasmonic properties of supported Pt and Pd nanostructures,” *Nano Lett.*, 2006.

[195] A. Wieckowski, *Interfacial electrochemistry: Theory: Experiment, and applications*. 2017.

[196] L. Zhang, Y. Wen, Y. Pan, and H. Yang, "2-Amino-5-(4-pyridinyl)-1,3,4-thiadiazole film at the silver surface: Observation by Raman spectroscopy and electrochemical methods," *Appl. Surf. Sci.*, vol. 257, no. 15, pp. 6347–6352, 2011.

[197] M. Musiani, J. Y. Liu, and Z. Q. Tian, "Applications of Electrochemical Surface-Enhanced Raman Spectroscopy (EC-SERS)," in *Developments in Electrochemistry: Science Inspired by Martin Fleischmann*, 2014.

[198] S. A. Maier and H. A. Atwater, "Plasmonics: Localization and guiding of electromagnetic energy in metal/dielectric structures," *J. Appl. Phys.*, vol. 98, no. 1, p. 11101, Jul. 2005.

[199] Z. Q. Tian, B. Ren, and D. Y. Wu, "Surface-enhanced Raman scattering: From noble to transition metals and from rough surfaces to ordered nanostructures," *Journal of Physical Chemistry B*. 2002.

[200] Z. Yang *et al.*, "Surface enhanced Raman scattering of pyridine adsorbed on Au@Pd core/shell nanoparticles," *J. Chem. Phys.*, vol. 130, no. 23, p. 234705, Jun. 2009.

[201] D. Y. Wu, M. Hayashi, S. H. Lin, and Z. Q. Tian, "Theoretical differential Raman scattering cross-sections of totally-symmetric vibrational modes of free pyridine and pyridine-metal cluster complexes," *Spectrochim. Acta - Part A Mol. Biomol. Spectrosc.*, 2004.

[202] A. H. Ali and C. A. Foss, "Electrochemically induced shifts in the plasmon resonance bands of nanoscopic gold particles adsorbed on transparent electrodes," *J. Electrochem. Soc.*, vol. 146, no. 2, pp. 628–636, 1999.

[203] V. O. Santos, M. B. Alves, M. S. Carvalho, P. A. Z. Suarez, and J. C. Rubim, "Surface-Enhanced Raman Scattering at the Silver Electrode/Ionic Liquid (BMIPF6) Interface," *J. Phys. Chem. B*, vol. 110, no. 41, pp. 20379–20385, Oct. 2006.

[204] B. I. Lundqvist, T. Fondén, J. Idiodi, P. Johnsson, A. Mällo, and S. Papadia, "Theoretical descriptions of atomic and molecular chemisorption on metals," *Prog. Surf. Sci.*, vol. 25, no. 1, pp. 191–210, 1987.

[205] J. Gersten and A. Nitzan, "Electromagnetic theory of enhanced Raman scattering by molecules adsorbed on rough surfaces," *J. Chem. Phys.*, vol. 73, no. 7, pp. 3023–3037, Oct. 1980.

[206] A. Bruckbauer and A. Otto, *Raman Spectroscopy of Pyridine Adsorbed on Single Crystal Copper Electrodes*, vol. 29. 1998.

[207] J. Lombardi and R. Birke, *Time-dependent picture of the charge-transfer contributions to surface enhanced Raman spectroscopy*, vol. 126. 2007.

[208] D. Y. Wu, J. F. Li, B. Ren, and Z. Q. Tian, "Electrochemical surface-enhanced Raman spectroscopy of nanostructures," *Chem. Soc. Rev.*, 2008.

[209] K. Kim, H. B. Lee, J. K. Yoon, D. Shin, and K. S. Shin, "Ag Nanoparticle-Mediated Raman Scattering of 4-Aminobenzenethiol on a Pt Substrate," *J. Phys. Chem. C*, vol. 114, no. 32, pp. 13589–13595, Aug. 2010.

[210] B. Ren, Y. Cui, D.-Y. Wu, and Z.-Q. Tian, "Electrochemical SERS and its Application in Analytical, Biophysical and Life Science," *Surface Enhanced Raman Spectroscopy*. 28-Dec-2010.

[211] D. D. Usta, K. Salimi, A. Pinar, İ. Coban, T. Tekinay, and A. Tuncel, "A Boronate Affinity-Assisted SERS Tag Equipped with a Sandwich System for Detection of Glycated Hemoglobin in the Hemolysate of Human Erythrocytes," *ACS Appl. Mater. Interfaces*, vol. 8, no. 19, pp. 11934–11944, May 2016.

[212] Á. I. López-Lorente and C. Kranz, "Recent advances in biomolecular vibrational spectroelectrochemistry," *Curr. Opin. Electrochem.*, vol. 5, no. 1, pp. 106–113, 2017.

[213] L. Zhao, J. Blackburn, and C. L. Brosseau, "Quantitative Detection of Uric Acid by Electrochemical-Surface Enhanced Raman Spectroscopy Using a Multilayered Au/Ag Substrate," *Anal. Chem.*, vol. 87, no. 1, pp. 441–447, Jan. 2015.

[214] R. A. Karaballi, A. Nel, S. Krishnan, J. Blackburn, and C. L. Brosseau, "Development of an electrochemical surface-enhanced Raman spectroscopy (EC-SERS) aptasensor for direct detection of DNA hybridization," *Phys. Chem. Chem. Phys.*, vol. 17, pp. 21356–21363, 2015.

[215] A. M. Robinson, S. G. Harroun, J. Bergman, and C. L. Brosseau, "Portable electrochemical surface-enhanced raman spectroscopy system for routine spectroelectrochemical analysis," *Anal. Chem.*, 2012.

[216] Z. Zhu *et al.*, "Electrochemically Modulated Surface-Enhanced Raman Spectra of Aminoglutethimide (AGI) on a Ag-Sputtered Electrode," *Bull. Chem. Soc. Jpn.*, vol. 91, no. 11, pp. 1579–1585, Sep. 2018.

[217] L. Xu, Z. Lei, J. Li, C. Zong, C. J. Yang, and B. Ren, "Label-Free Surface-Enhanced Raman Spectroscopy Detection of DNA with Single-Base Sensitivity," 2015.

[218] H. K. Lee *et al.*, "Designing surface-enhanced Raman scattering (SERS) platforms beyond hotspot engineering: emerging opportunities in analyte manipulations and hybrid materials," *Chem. Soc. Rev.*, vol. 48, no. 3, pp. 731–756, 2019.

[219] R. A. Karaballi, S. Merchant, S. R. Power, and C. L. Brosseau, "Electrochemical surface-enhanced Raman spectroscopy (EC-SERS) study of the interaction between protein aggregates and biomimetic membranes," *Phys. Chem. Chem. Phys.*, 2018.

[220] H. L. Zheng, S. S. Yang, J. Zhao, and Z. C. Zhang, "Synthesis of rGO–Ag nanoparticles for high-performance SERS and the adsorption geometry of 2-mercaptobenzimidazole on Ag surface," *Appl. Phys. A*, vol. 114, no. 3, pp. 801–808, 2014.

[221] H. Ryoo, Y. M. Lee, and K. Kim, "Surface-Enhanced Raman Scattering of Benzenethiol Adsorbed on Silver-Exchanged Copper Powders," *file:///Users/ascecheng/Downloads/10.5012_BKCS.2008.29.2.445 (1).ris*, vol. 29, Feb. 2008.

[222] Y. Wang *et al.*, "Mercaptopyridine Surface-Functionalized CdTe Quantum Dots with Enhanced Raman Scattering Properties," *J. Phys. Chem. C*, vol. 112, no. 4, pp. 996–1000, Jan. 2008.

[223] Y.-C. Liu and C.-C. Wang, "Effect of Argon Plasma Treatment on Surface-Enhanced Raman Spectroscopy of Polypyrrole Deposited on Electrochemically Roughened Gold Substrates," *J. Phys. Chem. B*, vol. 109, no. 12, pp. 5779–5782, Mar. 2005.

[224] Z. Zhu, H. Yoshikawa, M. Saito, B. Fan, and E. Tamiya, "Fabrication of Surface-enhanced Raman Spectroscopy (SERS) – Active Electrodes by Silver Sputtering Deposition for Electrochemical SERS Analysis," *Electroanalysis*, vol. 30, no. 7, pp. 1432–1437, Jul. 2018.

[225] H. M. Dykstra, S. B. Hall, and M. R. Waterland, "A spectroelectrochemical investigation of nanoparticle and molecular resonances in surface enhanced Raman scattering from crystal violet and malachite green," *J. Raman Spectrosc.*, vol. 48, no. 3, pp. 405–412, Mar. 2017.

[226] C. Zong, C.-J. Chen, M. Zhang, D.-Y. Wu, and B. Ren, "Transient Electrochemical Surface-Enhanced Raman Spectroscopy: A Millisecond Time-Resolved Study of an Electrochemical Redox Process," *J. Am. Chem. Soc.*, vol. 137, no. 36, pp. 11768–11774, Sep. 2015.

[227] L.-Q. Xie *et al.*, "Adsorption of Dye Molecules on Single Crystalline Semiconductor Surfaces: An Electrochemical Shell-Isolated Nanoparticle Enhanced Raman Spectroscopy Study," *J. Phys. Chem. C*, vol. 120, no. 39, pp. 22500–22507, Oct. 2016.

Chapter 2

[228] A. Gopinath, S. V. Boriskina, W. R. Premasiri, L. Ziegler, B. M. Reinhard, and L. D. Negro, "Plasmonic nanogalaxies: Multiscale aperiodic arrays for surface-enhanced Raman sensing," *Nano Lett.*, 2009.

[229] S. M. Wells, S. D. Retterer, J. M. Oran, and M. J. Sepaniak, “Controllable nanofabrication of aggregate-like nanoparticle substrates and evaluation for surface-enhanced Raman spectroscopy,” *ACS Nano*, 2009.

[230] J. L. Abell, J. D. Driskell, R. A. Dluhy, R. A. Tripp, and Y. P. Zhao, “Fabrication and characterization of a multiwell array SERS chip with biological applications,” *Biosens. Bioelectron.*, 2009.

[231] G. Hong, C. Li, and Limin Qi, “Facile fabrication of two-dimensionally ordered macroporous silver thin films and their application in molecular sensing,” in *Advanced Functional Materials*, 2010.

[232] J. Hu and C. Y. Zhang, “Sensitive detection of nucleic acids with rolling circle amplification and surface-enhanced raman scattering spectroscopy,” *Anal. Chem.*, 2010.

[233] Y.-Y. Lin, J.-D. Liao, Y.-H. Ju, C.-W. Chang, and A.-L. Shiau, “Focused ion beam-fabricated Au micro/nanostructures used as a surface enhanced Raman scattering-active substrate for trace detection of molecules and influenza virus,” *Nanotechnology*, vol. 22, no. 18, p. 185308, 2011.

[234] C. W. Chang, J. Der Liao, Y. Y. Lin, and C. C. Weng, “Detecting very small quantity of molecular probes in solution using nano-mechanically made Au-cavities array with SERS-active effect,” *Sensors Actuators, B Chem.*, 2011.

[235] S. Habouti, M. Mátéfi-Tempfli, C.-H. Solterbeck, M. Es-Souni, S. Mátéfi-Tempfli, and M. Es-Souni, “On-substrate, self-standing Au-nanorod arrays showing morphology controlled properties,” *Nano Today*, vol. 6, no. 1, pp. 12–19, 2011.

[236] Y. Liu, S. Xu, X. Xuyang, B. Zhao, and W. Xu, “Long-range surface plasmon field-enhanced raman scattering spectroscopy based on evanescent field excitation,” *J. Phys. Chem. Lett.*, 2011.

[237] H. Y. Wu, C. J. Choi, and B. T. Cunningham, “Plasmonic nanogap-enhanced raman scattering using a resonant nanodome array,” *Small*, 2012.

[238] S. J. Barcelo, A. Kim, W. Wu, and Z. Li, “Fabrication of deterministic nanostructure assemblies with sub-nanometer spacing using a nanoimprinting transfer technique,” *ACS Nano*, 2012.

[239] M. L. Seol *et al.*, “A nanoforest structure for practical surface-enhanced Raman scattering substrates,” *Nanotechnology*, 2012.

[240] G. Das *et al.*, “Plasmon based biosensor for distinguishing different peptides mutation states,” *Sci. Rep.*, vol. 3, p. 1792, May 2013.

[241] H. Im, K. C. Bantz, S. H. Lee, T. W. Johnson, C. L. Haynes, and S. H. Oh, “Self-assembled plasmonic nanoring cavity arrays for SERS and LSPR biosensing,” *Adv. Mater.*, 2013.

[242] H. W. Cheng, S. Y. Huan, H. L. Wu, G. L. Shen, and R. Q. Yu, “Surface-enhanced Raman spectroscopic detection of a bacteria biomarker using gold nanoparticle immobilized substrates,” *Anal. Chem.*, 2009.

[243] Y. Liu, J. Fan, Y. P. Zhao, S. Shanmukh, and R. A. Dluhy, “Angle dependent surface enhanced Raman scattering obtained from a Ag nanorod array substrate,” *Appl. Phys. Lett.*, 2006.

[244] J. Fu, Z. Cao, and L. Yobas, “Localized oblique-angle deposition: Ag nanorods on microstructured surfaces and their SERS characteristics,” *Nanotechnology*, 2011.

[245] W. Tian, G. Rui, and Z. Fu, “A blind adaptive matching pursuit algorithm for compressed sensing based on divide and conquer,” in *Lecture Notes in Electrical Engineering*, 2012.

[246] M. Li *et al.*, “Three-dimensional hierarchical plasmonic nano-architecture enhanced surface-enhanced Raman scattering immunosensor for cancer biomarker detection in blood plasma,” *ACS Nano*, 2013.

[247] A. Gutes, C. Carraro, and R. Maboudian, “Silver nanodesert rose as a substrate for surface-enhanced raman spectroscopy,” *ACS Appl. Mater. Interfaces*, 2009.

[248] J. Fu, W. Ye, and C. Wang, “Facile synthesis of Ag dendrites on Al foil via galvanic replacement reaction with [Ag(NH3)2]Cl for ultrasensitive SERS detecting of biomolecules,” *Mater. Chem. Phys.*, 2013.

[249] J. Erlebacher, M. J. Aziz, A. Karma, N. Dimitrov, and K. Sieradzki, “Evolution of nanoporosity in dealloying,” *Nature*, 2001.

[250] T. Qiu, W. Zhang, and P. K. Chu, “Aligned silver nanorod arrays for surface-enhanced Raman spectroscopy,” *Phys. B Condens. Matter*, 2009.

[251] Y. S. Huh and D. Erickson, “Aptamer based surface enhanced Raman scattering detection of vasopressin using multilayer nanotube arrays,” *Biosens. Bioelectron.*, 2010.

[252] K. E. Shafer-Peltier, C. L. Haynes, M. R. Glucksberg, and R. P. Van Duyne, “Toward a glucose biosensor based on surface-enhanced Raman scattering,” *J. Am. Chem. Soc.*, 2003.

[253] D. R. P. Van, j C. Hulteen, and D. A. Treichel, “Atomic force microscopy and surface-enhanced Raman spectroscopy. I. Silver island films and silver film over polymer nanosphere surfaces supported on glass,” *J. Chem. Phys.*, vol. 99, no. Copyright (C) 2013 American Chemical Society (ACS). All Rights Reserved., pp. 2101–2115, 1993.

[254] X. Zhang, M. A. Young, O. Lyandres, and R. P. Van Duyne, “Rapid detection of an anthrax biomarker by surface-enhanced Raman spectroscopy,” *J. Am. Chem. Soc.*, 2005.

[255] J. M. McMahon, S. Li, L. K. Ausman, and G. C. Schatz, “Modeling the effect of small gaps in surface-enhanced Raman spectroscopy,” *J. Phys. Chem. C*, 2012.

[256] M. A. Khan, T. P. Hogan, and B. Shanker, “Gold-coated zinc oxide nanowire-based substrate for surface-enhanced Raman spectroscopy,” *J. Raman Spectrosc.*, 2009.

[257] M. Tudorache and C. Bala, “Biosensors based on screen-printing technology, and their applications in environmental and food analysis,” *Analytical and Bioanalytical Chemistry*. 2007.

[258] P. Fanjul-Bolado, D. Hernández-Santos, P. J. Lamas-Ardisana, A. Martín-Pernía, and A. Costa-García, "Electrochemical characterization of screen-printed and conventional carbon paste electrodes," *Electrochim. Acta*, 2008.

[259] F. Arduini *et al.*, "Electrochemical biosensors based on nanomodified screen-printed electrodes: Recent applications in clinical analysis," *TrAC - Trends in Analytical Chemistry*. 2016.

[260] O. D. Renedo, M. A. Alonso-Lomillo, and M. J. A. Martínez, "Recent developments in the field of screen-printed electrodes and their related applications," *Talanta*. 2007.

[261] F. Tan, J. P. Metters, and C. E. Banks, "Electroanalytical applications of screen printed microelectrode arrays," *Sensors Actuators, B Chem.*, 2013.

[262] Ł. Tymecki, E. Zwierkowska, and R. Koncki, "Screen-printed reference electrodes for potentiometric measurements," *Anal. Chim. Acta*, 2004.

[263] J. P. Hart and S. A. Wring, "Recent developments in the design and application of screen-printed electrochemical sensors for biomedical, environmental and industrial analyses," *TrAC - Trends in Analytical Chemistry*. 1997.

[264] A. Hayat and J. L. Marty, "Disposable screen printed electrochemical sensors: Tools for environmental monitoring," *Sensors (Switzerland)*. 2014.

[265] M. E. Abdelsalam, P. N. Bartlett, J. J. Baumberg, S. Cintra, T. A. Kelf, and A. E. Russell, "Electrochemical SERS at a structured gold surface," vol. 7, pp. 740–744, 2005.

[266] A. M. Robinson, S. G. Harroun, J. Bergman, and C. L. Brosseau, "Portable electrochemical surface-enhanced raman spectroscopy system for routine spectroelectrochemical analysis," *Anal. Chem.*, vol. 84, no. 3, pp. 1760–1764, 2012.

[267] S. G. Harroun *et al.*, "Electrochemical surface-enhanced Raman spectroscopy (E-SERS) of novel biodegradable ionic liquids," *Phys. Chem. Chem. Phys.*, vol. 15, no. 44, p. 19205, 2013.

[268] B. H. C. Greene, D. S. Alhatab, C. C. Pye, and C. L. Brosseau, “Electrochemical-Surface Enhanced Raman Spectroscopic (EC-SERS) Study of 6-Thiouric Acid: A Metabolite of the Chemotherapy Drug Azathioprine,” *J. Phys. Chem. C*, 2017.

Chapter 3

[269] P. C. Lee and D. Meisel, “Adsorption and surface-enhanced Raman of dyes on silver and gold sols,” *J. Phys. Chem.*, 1982.

[270] D.-S. Wang and C.-W. Lin, “Density-dependent optical response of gold nanoparticle monolayers on silicon substrates,” *Opt. Lett.*, 2007.

[271] B. Gross, G. M. Sessler, and J. E. West, “Charge dynamics for electron-irradiated polymer-foil electrets,” *J. Appl. Phys.*, 1974.

[272] E. G. Bortchagovsky, A. Dejneka, L. Jastrabik, V. Z. Lozovski, and T. O. Mishakova, “Deficiency of standard effective-medium approximation for ellipsometry of layers of nanoparticles,” *J. Nanomater.*, 2015.

[273] D. Stroud, “The effective medium approximations: Some recent developments,” *Superlattices Microstruct.*, 1998.

[274] B. L. Goodall, A. M. Robinson, and C. L. Brosseau, “Electrochemical-surface enhanced Raman spectroscopy (E-SERS) of uric acid: A potential rapid diagnostic method for early preeclampsia detection,” *Phys. Chem. Chem. Phys.*, 2013.

[275] R. Gupta and W. A. Weimer, “High enhancement factor gold films for surface enhanced Raman spectroscopy,” *Chem. Phys. Lett.*, 2003.

[276] K. Zhang, S. Yu, B. Jv, and W. Zheng, “Interaction of Rhodamine 6G molecules with graphene: A combined computational-experimental study,” *Phys. Chem. Chem. Phys.*, 2016.

[277] W. B. Cai *et al.*, “Investigation of surface-enhanced Raman scattering from platinum electrodes using a confocal Raman microscope: Dependence of surface roughening pretreatment,” *Surf. Sci.*, 1998.

[278] H. Yoshikawa, A. Hironou, Z. Shen, and E. Tamiya, “Versatile Micropatterning of Plasmonic Nanostructures by Visible Light Induced Electroless Silver Plating on Gold Nanoseeds,” *ACS Appl. Mater. Interfaces*, 2016.

[279] W. L. J. Hasi *et al.*, “Chloride ion-assisted self-assembly of silver nanoparticles on filter paper as SERS substrate,” *Appl. Phys. A Mater. Sci. Process.*, 2014.

[280] M. Vezvaie, C. L. Brosseau, and J. Lipkowski, “Electrochemical SERS study of a biomimetic membrane supported at a nanocavity patterned Ag electrode,” *Electrochim. Acta*, 2013.

[281] S. A. Bainbridge and J. M. Roberts, “Uric Acid as a Pathogenic Factor in Preeclampsia,” *Placenta*, 2008.

[282] T. E. Furtak and S. H. Macomber, “Voltage-induced shifting of charge-transfer excitations and their role in surface-enhanced Raman scattering,” *Chem. Phys. Lett.*, 1983.

[283] M. Osawa, N. Matsuda, K. Yoshii, and I. Uchida, “Charge transfer resonance Raman process in surface-enhanced Raman scattering from p-aminothiophenol adsorbed on silver: Herzberg-Teller contribution,” *J. Phys. Chem.*, 1994.

[284] D. Y. Wu, B. Ren, Y. X. Jiang, X. Xu, and Z. Q. Tian, “Density functional study and normal-mode analysis of the bindings and vibrational frequency shifts of the pyridine-M (M = Cu, Ag, Au, Cu+, Ag+, Au+, and Pt) complexes,” *J. Phys. Chem. A*, 2002.

[285] L. L. Zhao, L. Jensen, and G. C. Schatz, “Surface-enhanced raman scattering of pyrazine at the junction between two Ag 20 nanoclusters,” *Nano Lett.*, 2006.

Chapter 4

[286] A. A. Elbashir, F. E. O. Suliman, B. Saad, and H. Y. Aboul-Enein, “Determination of aminoglutethimide enantiomers in pharmaceutical formulations by capillary electrophoresis using methylated-β-cyclodextrin as a chiral selector and computational calculation for their respective inclusion complexes,” *Talanta*, vol. 77, no. 4, pp. 1388–1393, 2009.

[287] I. Izquierdo-Lorenzo, S. Sanchez-Cortes, and J. V. Garcia-Ramos, “Trace detection of aminoglutethimide drug by surface-enhanced Raman spectroscopy: A vibrational and adsorption study on gold nanoparticles,” *Anal. Methods*, 2011.

[288] M. M. Abdel-Khalek, M. S. Mahrous, H. G. Daabees, and Y. A. Beltagy, “Spectrophotometric determination of aminoglutethimide by diazotization and subsequent coupling,” *Anal. Lett.*, 1993.

[289] G. K. Poon, G. G. F. Bisset, and M. Prakash, “Electrospray ionization mass spectrometry for analysis of low-molecular-weight anticancer drugs and their analogues,” *J. Am. Soc. Mass Spectrom.*, 1993.

[290] N. Cesur, T. I. Apak, H. Y. Aboul-Enein, and S. Özkrml, “LC determination of aminoglutethimide enantiomers as dansyl and fluorescamine derivatives in tablet formulations,” *J. Pharm. Biomed. Anal.*, 2002.

[291] I. Izquierdo-Lorenzo, I. Alda, S. Sanchez-Cortes, and J. V. Garcia-Ramos, “Adsorption and detection of sport doping drugs on metallic plasmonic nanoparticles of different morphology,” *Langmuir*, 2012.

[292] K. Yamanaka *et al.*, “Rapid detection for primary screening of influenza A virus: Microfluidic RT-PCR chip and electrochemical DNA sensor,” *Analyst*, 2011.

[293] S. K. Bhunia, L. Zeiri, J. Manna, S. Nandi, and R. Jelinek, “Carbon-Dot/Silver-Nanoparticle Flexible SERS-Active Films,” *ACS Appl. Mater. Interfaces*, 2016.

[294] M. L. Cheng, B. C. Tsai, and J. Yang, “Silver nanoparticle-treated filter paper as a highly sensitive surface-enhanced Raman scattering (SERS) substrate for detection of tyrosine in aqueous solution,” *Anal. Chim. Acta*, 2011.

[295] X. Yan, T. Suzuki, Y. Kitahama, H. Sato, T. Itoh, and Y. Ozaki, “A study on the interaction of single-walled carbon nanotubes (SWCNTs) and polystyrene (PS) at the interface in SWCNT-PS nanocomposites using tip-enhanced Raman spectroscopy,” *Phys. Chem. Chem. Phys.*, 2013.

[296] B. Liedberg, C. Nylander, and I. Lunström, “Surface plasmon resonance for gas detection and biosensing,” *Sensors and Actuators*, 1983.

[297] K. S. Phillips and Q. J. Cheng, “Surface plasmon resonance,” in *Molecular Biomethods Handbook: Second Edition*, 2008.

[298] J. J. Mock, M. Barbic, D. R. Smith, D. A. Schultz, and S. Schultz, “Shape effects in plasmon resonance of individual colloidal silver nanoparticles,” *J. Chem. Phys.*, 2002.

[299] A. K. Sarychev, G. Shvets, and V. M. Shalaev, “Magnetic plasmon resonance,” *Phys. Rev. E - Stat. Nonlinear, Soft Matter Phys.*, 2006.

[300] A. D. McFarland and R. P. Van Duyne, “Single silver nanoparticles as real-time optical sensors with zeptomole sensitivity,” *Nano Lett.*, 2003.

[301] M. Castellá-Ventura and E. Kassab, “Comparative semiempirical and ab initio study of the harmonic vibrational frequencies of aniline—I. The ground state,” *Spectrochim. Acta Part A Mol. Spectrosc.*, vol. 50, no. 1, pp. 69–86, 1994.

[302] T. E. Furtak, “Current understanding of the mechanism of surface enhanced Raman scattering,” *J. Electroanal. Chem. Interfacial Electrochem.*, vol. 150, no. 1, pp. 375–388, 1983.

[303] J. Billman and A. Otto, “Charge transfer between adsorbed cyanide and silver probed by sers,” *Surf. Sci.*, 1984.

[304] L. Zhao, L. Jensen, and G. C. Schatz, “Pyridine-Ag20 cluster: A model system for studying surface-enhanced Raman scattering,” *J. Am. Chem. Soc.*, 2006.

Chapter 5

[305] A. G. Brolo, D. E. Irish, and J. Lipkowski, “Surface-Enhanced Raman Spectra of Pyridine and Pyrazine Adsorbed on a Au(210) Single-Crystal Electrode,” *J. Phys. Chem. B*, 1997.

[306] S. Shimizu *et al.*, “Pyridine and Pyridine Derivatives,” in *Ullmann’s Encyclopedia of Industrial Chemistry*, 2000.

[307] D. Wu, B. Ren, and Z.-Q. Tian, *A Theoretical Study on SERS Intensity of Pyridine Adsorbed on Transition Metal Electrodes*, vol. 46. 2010.

[308] X. Lin, B. Ren, Z. Yang, G. kun Liu, and Z.-Q. Tian, *Surface-enhanced Raman spectroscopy with ultraviolet excitation*, vol. 36. 2005.

[309] M. Abdelsalam *et al.*, "Quantitative electrochemical SERS of flavin at a structured silver surface," *Langmuir*, 2008.

[310] R. A. Karaballi, S. Merchant, S. Power, and C. L. Brosseau, "Electrochemical surface-enhanced Raman spectroscopy (EC-SERS) study of the interaction between protein aggregates and biomimetic," no. 902, 2018.

[311] A. Fanigliulo and B. Bozzini, "An electrochemical and SERS study of benzyldimethylphenylammonium chloride at a polycrystalline gold electrode," vol. 47, pp. 4511–4521, 2002.

[312] S. Chen *et al.*, "Electrochimica Acta Electrochemical fabrication of pyramid-shape silver microstructure as effective and reusable SERS substrate," *Electrochim. Acta*, vol. 274, pp. 242–249, 2018.

[313] D. Y. Wu, M. Hayashi, C. H. Chang, K. K. Liang, and S. H. Lin, "Bonding interaction, low-lying states and excited charge-transfer states of pyridine-metal clusters: Pyridine-Mn(M = Cu, Ag, Au; n = 2-4)," *J. Chem. Phys.*, 2003.

[314] R. L. Birke, V. Znamenskiy, and J. R. Lombardi, "A charge-transfer surface enhanced Raman scattering model from time-dependent density functional theory calculations on a Ag10 -pyridine complex," *J. Chem. Phys.*, 2010.

Appendix a.

Sample ID
Ag 5nm

Details	
Software and regression log	
Software about	Semilab - Spectroscopic Ellipsometry Analyzer - SEA
Software version	1.5.2
Officially licensed to	Semilab Japan
Operator	Operator
Date and time of regression	07-07-2016 12:11
Comments	

Layer structure	
Overview	
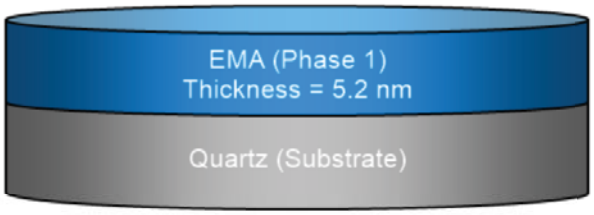	
Optical model	
Phase 1	EMA
EMA	Ag + Dispersionlaws

Measurement information				
Measurement file path	C:\SAM SUITE\Result\Measured Data\V0005\Ag\Ag 5nm.smdx			
Angle of Incidence	60.3°			
Regression details				
Regression 1 (EllipsoReflectance)				
Wavelength range	290.08 - 976.21 nm			
Angle of Incidence	60.3°			
Fit to	Ψ, Δ			
Angular Aperture	0°			
Fit algorithm	LMA			
Results				
Parameters	Value	Fitted	2 σ confidence limit	Unit
Model				
AOI Shift	0			°
Angular Aperture	0			°
Phase 1 (EMA)				
Thickness	5.243	X	0.00023	nm
Depolarization coefficient	0.33333			
Concentration 1	0.2499	X	16454450.83395	
Concentration 2	0.7501	X	49388988.95453	
B (µm^2)	-0.82237	X	0.05141	µm^2
C (µm^4)	0.05303	X	0.00404	µm^4
D	2.97095	X	0.28167	
E (µm^2)	0.16867	X	0.07771	µm^2
F (µm^4)	-0.0485	X	0.0058	µm^4
N_inf	3.73198	X	0.13979	

Derived parameters	Value
Phase 1 (EMA)	
n @ 550 nm	1.2213
k @ 550 nm	3.1063
n @ 632.8 nm	1.5476
k @ 632.8 nm	3.3564
Substrate (Quartz)	
n @ 550 nm	1.4629
k @ 550 nm	0
n @ 632.8 nm	1.4598
k @ 632.8 nm	0
Fit quality	
R^2	0.95097
RMSE	0.90298

Correlation coefficients	
Ph1 - EMA - Thickness --- Ph1 - Concentration 1	-0.0172
Ph1 - EMA - Thickness --- Ph1 - Concentration 2	-0.0172
Ph1 - EMA - Thickness --- Ph1 - Cauchy - B (µm^2)	0.8872
Ph1 - EMA - Thickness --- Ph1 - Cauchy - C (µm^4)	-0.8778
Ph1 - EMA - Thickness --- Ph1 - Cauchy - D	-0.6804
Ph1 - EMA - Thickness --- Ph1 - Cauchy - E (µm^2)	0.2825
Ph1 - EMA - Thickness --- Ph1 - Cauchy - F (µm^4)	-0.06
Ph1 - Concentration 1 --- Ph1 - Concentration 2	1
Ph1 - Concentration 1 --- Ph1 - Cauchy - B (µm^2)	0.0016
Ph1 - Concentration 1 --- Ph1 - Cauchy - C (µm^4)	-0.0004
Ph1 - Concentration 1 --- Ph1 - Cauchy - D	0.0307
Ph1 - Concentration 1 --- Ph1 - Cauchy - E (µm^2)	-0.0184
Ph1 - Concentration 1 --- Ph1 - Cauchy - F (µm^4)	0.0112
Ph1 - Concentration 2 --- Ph1 - Cauchy - B (µm^2)	0.0016
Ph1 - Concentration 2 --- Ph1 - Cauchy - C (µm^4)	-0.0004
Ph1 - Concentration 2 --- Ph1 - Cauchy - D	0.0307
Ph1 - Concentration 2 --- Ph1 - Cauchy - E (µm^2)	-0.0184
Ph1 - Concentration 2 --- Ph1 - Cauchy - F (µm^4)	0.0112
Ph1 - Cauchy - B (µm^2) --- Ph1 - Cauchy - C (µm^4)	-0.9747
Ph1 - Cauchy - B (µm^2) --- Ph1 - Cauchy - D	-0.5552
Ph1 - Cauchy - B (µm^2) --- Ph1 - Cauchy - E (µm^2)	0.1994
Ph1 - Cauchy - B (µm^2) --- Ph1 - Cauchy - F (µm^4)	-0.0037
Ph1 - Cauchy - C (µm^4) --- Ph1 - Cauchy - D	0.6973
Ph1 - Cauchy - C (µm^4) --- Ph1 - Cauchy - E (µm^2)	-0.3918
Ph1 - Cauchy - C (µm^4) --- Ph1 - Cauchy - F (µm^4)	0.2062
Ph1 - Cauchy - D --- Ph1 - Cauchy - E (µm^2)	-0.8898
Ph1 - Cauchy - D --- Ph1 - Cauchy - F (µm^4)	0.7626
Ph1 - Cauchy - E (µm^2) --- Ph1 - Cauchy - F (µm^4)	-0.9732

Appendix b.

Sample ID
Ag 10nm

Details	
Software and regression log	
Software about	Semilab - Spectroscopic Ellipsometry Analyzer - SEA
Software version	1.5.2
Officially licensed to	Semilab Japan
Operator	Operator
Date and time of regression	07-07-2016 12:18
Comments	

Layer structure	
Overview	
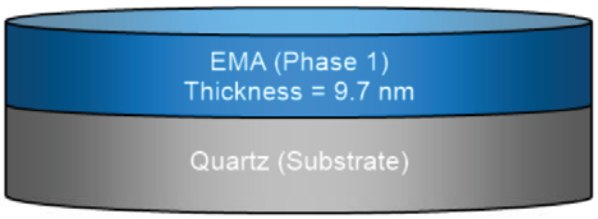	
Optical model	
Phase 1	EMA
EMA	Ag + Void

Measurement information				
Measurement file path	C:\SAM SUITE\Result\Measured Data\V0005\Ag\Ag 10nm.smdx			
Angle of Incidence	60.3°			
Regression details				
Regression 1 (EllipsoReflectance)				
Wavelength range	290.08 - 976.21 nm			
Angle of Incidence	60.3°			
Fit to	Ψ, Δ			
Angular Aperture	0°			
Fit algorithm	LMA			
Results				
Parameters	Value	Fitted	2 σ confidence limit	Unit
Model				
AOI Shift	0			°
Angular Aperture	0			°
Phase 1 (EMA)				
Thickness	9.727	X	0.00004	nm
Depolarization coefficient	0.33333			
Concentration 1	1.01487	X	188369.48695	
Concentration 2	-0.01487	X	2759.54419	

Derived parameters	Value
Phase 1 (EMA)	
n @ 550 nm	0.126
k @ 550 nm	3.3822
n @ 632.8 nm	0.1365
k @ 632.8 nm	4.0355
Substrate (Quartz)	
n @ 550 nm	1.4629
k @ 550 nm	0
n @ 632.8 nm	1.4598
k @ 632.8 nm	0
Fit quality	
R^2	0.99601
RMSE	0.40988

List of Publications

[1] Zicheng Zhu, Hiroyuki Yoshikawa, Masato Saito, Bin Fan and Eiichi Tamiya, "Fabrication of Surface-Enhanced Raman Spectroscopy (SERS) - Active Electrodes by Silver Sputtering Deposition for Electrochemical SERS Analysis", Electroanalysis, 30 (2018), 1-7. (Accepted, DOI: https://doi.org/10.1002/elan.201800003)

[2] Zicheng Zhu, Wilfred Villariza Espulgar, Hiroyuki Yoshikawa, Masato Saito, Bin Fan, Xiaoming Dou and Eiichi Tamiya, "Electrochemically Modulated Surface-Enhanced Raman Spectra of Aminoglutethimide (AGI) on the Ag-sputtered Electrode", Bulletin of the Chemical Society of Japan, Vol. 91 (2018), Issue 11, 1579-1585. (Accepted, DOI: https://doi.org/10.1246/bcsj.20180172)

[3] Zicheng Zhu, Wilfred Villariza Espulgar, Hiroyuki Yoshikawa, Masato Saito, Bin Fan, Xiaoming Dou and Eiichi Tamiya, "Detection of the Organophosphorus Pesticides using Electrochemical Surface-Enhanced Raman Spectra System" (In preparation)

[4] Zicheng Zhu, Wilfred Villariza Espulgar, Hiroyuki Yoshikawa, Masato Saito and Eiichi Tamiya, "Multiplex Electrochemical Surface-Enhanced Raman Spectra (EC-SERS) Analysis based on Microwell Array Electrodes" (In preparation)

[5] Zicheng Zhu, Wilfred Villariza Espulgar, Hiroyuki Yoshikawa, Masato Saito and Eiichi Tamiya, "Review article: Bio-application of Electrochemical Surface-Enhanced Raman Spectra System" (In preparation)

List of presentations at scientific meetings

International conferences

[1] Zicheng Zhu, Hiroyuki Yoshikawa and Eiichi Tamiya, "Fabrication of Surface-Enhanced Raman Spectroscopy (SERS)-Active Electrode by Silver Sputtering Deposition and Application to the Electrochemical SERS Analysis", International Conference on Molecular Electronics and Bioelectronics, Kanazawa, Japan, June, 2017. (Poster presentation)

[2] Zicheng Zhu, Wilfred Villariza Espulgar, Hiroyuki Yoshikawa, Masato Saito and Eiichi Tamiya, "Quantitative Detection of Aminoglutethimide by Electrochemical Surface Enhanced Raman Spectroscopy", International Meeting on Chemical Sensors, Vienna, Austria, July, 2018. (Poster presentation)

[3] Zicheng Zhu, Wilfred Villariza Espulgar, Hiroyuki Yoshikawa, Masato Saito and Eiichi Tamiya, "Development and application of Electrochemical Surface-enhanced Raman Spectroscopy Biosensor", International Symposium on Applied Physics and Biomedical applications, Shanghai, China, November, 2018. (Oral Presentation)

Domestic conferences

[1] Zicheng Zhu, Ryo Nakagawa, Aya Hashimoto, Hiroyuki Yoshikawa and Eiichi Tamiya, "Fabrication of silver SERS-active electrode by sputtering deposition and

application to electrochemical SERS analysis", The 10th Joint Symposia of bio-related chemistry, Kanazawa, Japan, September, 2017. (Poster presentation)

[2] Zicheng Zhu, Hiroyuki Yoshikawa and Eiichi Tamiya, "Fabrication of silver SERS-active electrode by sputtering deposition and application to electrochemical SERS analysis", The JSAP-OSA Joint Symposia Kansai Chapter, Osaka, Japan, February, 2017. (Poster presentation)

[3] Zicheng Zhu, Ryo Nakagawa, Aya Hashimoto, Hiroyuki Yoshikawa and Eiichi Tamiya, "Fabrication of silver nanostructure on carbon screen printed electrode and application to electrochemical SERS analysis", The 64th JSAP-OSA Joint Symposia, Tokyo, Japan, March, 2017. (Poster presentation)

[4] Zicheng Zhu, Ryo Nakagawa, Aya Hashimoto, Hiroyuki Yoshikawa and Eiichi Tamiya, "Fabrication of silver nanostructure on carbon screen printed electrode and application to electrochemical SERS analysis", The 62th Meeting of Electrochemical Society of Japan, Nagasaki, Japan, September, 2017. (Oral presentation)

[5] Zicheng Zhu, Hiroyuki Yoshikawa, Masato Saito and Eiichi Tamiya, "Electrochemical SERS Analysis on SERS-Active Screen-Printed Electrodes", The 65th JSAP-OSA Joint Symposia, Tokyo, Japan, March, 2018. (Poster presentation)

[6] Zicheng Zhu, Wilfred Villariza Espulgar, Hiroyuki Yoshikawa, Masato Saito and Eiichi Tamiya, "Electrochemically Modulated Surface-Enhanced Raman Spectra of

Aminoglutethimide (AGI) on the Ag-sputtered Electrode", The 12th Joint Symposia of bio-related chemistry, Osaka, Japan, September, 2018. (Poster presentation)

[7] Zicheng Zhu, Wilfred Villariza Espulgar, Hiroyuki Yoshikawa, Masato Saito and Eiichi Tamiya, "EC-SERS Analysis of Aminoglutethimide on the Ag-sputtered Screen Printed Electrode", The 64th Meeting of Electrochemical Society of Japan, Kanazawa, Japan, September, 2018. (Oral presentation)

Acknowledgements

Firstly, I would like to thank my distinguished and cordial supervisor, Professor Eiichi Tamiya, who has guided me with academic advice, instructive suggestions, insightful ideas and enlightened me when I am confused. His patient encouragements are indispensable for my accomplishment of the doctoral dissertation.

Also, I would like to express my sincere gratitude to all the distinguished students and teachers who have taught me at the university, especially, to Assistant Professor Yoshikawa, Assistant Professor Saito, and Assistant Professor Wilfred, who influence me and help me with the experiments, each presentation of the conference and each published paper.

Besides, I am much obliged to Professor Takamura, Professor Kobayashi and Professor Verma who give me insightful comments. Their instructions distinctly improve me in my doctoral dissertation and my future studies.

Lastly, I also want to thank my family members, esp. my wife. It is their understanding and patience that make this dissertation possible.